WARWICK
THE UNIVERSITY OF WARWICK

A Thesis Submitted for the Degree of PhD at the University of Warwick

Permanent WRAP URL:
http://wrap.warwick.ac.uk/165351

Copyright and reuse:
This thesis is made available online and is protected by original copyright.
Please scroll down to view the document itself.
Please refer to the repository record for this item for information to help you to cite it.
Our policy information is available from the repository home page.

For more information, please contact the WRAP Team at: wrap@warwick.ac.uk

warwick.ac.uk/lib-publications

Spin decoherence in nanodiamond and digital signal processing for quantum sensing & magnetometry

by

Guy Anthony Stimpson

Thesis

Submitted to the University of Warwick

for the degree of

Doctor of Philosophy

Department of Physics

February 2020

Contents

List of Tables **v**

List of Figures **vi**

Acknowledgments **xx**

Declarations **xxii**

Abstract **xxiv**

Abbreviations **xxv**

Chapter 1 Introduction **1**

1.1 Expecting the Unexpected 2

1.1.1 An Unexpected Journey 2

1.1.2 An Unexpected Destination 3

1.1.3 An Unexpected Alliance 4

1.2 Motivation 5

1.3 Thesis structure 7

Chapter 2 Lock-in Amplifiers **12**

2.1 Introduction 13

2.2 Principles of operation 13

2.2.1 Theory 13

2.2.2 Practical considerations 18

2.3 Hardware 19

2.3.1 The STEMlab 125-14 19

2.3.2 Zurich Instruments HF2LI 20

2.4 Field programmable gate arrays 21

2.4.1 Principles 21

2.4.2 LIA Implementation 22
2.4.3 Hardware & software 23
2.4.4 Characterisation methodology 25
2.4.5 Magnetocardiography 27

Chapter 3 LIA Results **34**
3.1 Results 35
3.2 Discussion 46
3.2.1 Cross-talk 46

Chapter 4 Nanodiamonds **51**
4.1 Introduction 52
4.2 Diamond as a material 52
4.2.1 Crystallographic structure 52
4.2.2 Intrinsic material properties 53
4.2.3 Bonding 53
4.2.4 The tight binding model 54
4.2.5 Electronic properties 56
4.2.6 Thermal conductivity 59
4.3 Diamond synthesis 59
4.3.1 High Pressure High Temperature 61
4.3.2 Chemical Vapour Deposition 63
4.3.3 The role of hydrogen in CVD synthesis 66
4.4 The nitrogen vacancy centre 66
4.5 Fabrication of nanodiamonds 68
4.5.1 Detonation Nanodiamonds 69
4.5.2 Ball milling 69
4.5.3 Nanopillars 74
4.5.4 Treatment of nanodiamonds 76
4.6 Surface Chemistry 77
4.6.1 Termination 77
4.7 Elemental Purity 79
4.7.1 Carbon isotopes 79
4.7.2 Nitrogen 80
4.8 Effect of Size 80

Chapter 5 Electron Paramagnetic Resonance **100**
5.1 Spin dynamics . . . 101
5.1.1 The spin Hamiltonian . . . 101
5.1.2 Electronic Zeeman splitting . . . 102
5.1.3 Zero-field splitting . . . 104
5.1.4 Hyperfine interactions . . . 104
5.1.5 Quadrupole interactions . . . 105
5.1.6 Nuclear Zeeman splitting . . . 105
5.2 Practical EPR . . . 106
5.2.1 The EPR spectrometer . . . 106
5.2.2 Optically detected magnetic resonance . . . 109
5.3 Pulsed ODMR . . . 113
5.3.1 The Bloch interpretation . . . 113
5.3.2 Rabi oscillations . . . 114
5.3.3 Decoherence . . . 115
5.3.4 Spin echo . . . 117
5.3.5 Dynamic decoupling . . . 119
5.4 Optically detected magnetic resonance (ODMR) of fluorescent nanodiamonds . . . 119
5.4.1 Spin-spin decoherence . . . 120
5.5 Samples used for research . . . 121

Chapter 6 Magnetometry **126**
6.1 Ensemble NV magnetometry . . . 127
6.1.1 Basic setup . . . 127
6.1.2 Design considerations . . . 128
6.2 Magnetocardiography . . . 130
6.3 Experimental considerations . . . 131
6.3.1 Field homogeneity . . . 131
6.3.2 Fluorescence collection efficiency . . . 132
6.4 Potential improvements . . . 134
6.4.1 Infrared absorption . . . 134
6.4.2 Gradiometry . . . 137
6.4.3 MCG imaging . . . 137

Chapter 7 Confocal microscopy **143**
7.1 Room Temperature Confocal Fluorescence Microscopy . . . 144
7.1.1 Operating principles . . . 144

7.2 Silicon maps 149
7.2.1 Nanodiamond deposition 150
7.2.2 Confocal mapping 151
7.2.3 SEM 152
7.3 Continuous Wave ODMR 154
7.3.1 Nanodiamonds 155
7.4 Microscopy results 157
7.4.1 Auto-correlation statistics 159
7.5 Pulsed ODMR results 161
7.5.1 Rabi 161
7.5.2 Spin echo 162
7.6 Future research 165

Chapter 8 Optical trapping **169**
8.1 Theory & motivation 170
8.1.1 Macroscopicity 170
8.1.2 The physics of optical trapping 172
8.1.3 Experimental considerations 174
8.1.4 Trapping apparatus 175
8.1.5 Trap frequency 176
8.2 Homogeneous magnetic fields 178
8.3 Future research 181

Chapter 9 Conclusion **185**
9.1 Summary of findings 186
9.2 Concluding remarks 187

List of Tables

2.1 STEMlab 125-14 hardware specifications 20

3.1 RePLIA input noise level and corresponding sensitivity as measured after three different collection periods. 35

3.2 Time constants τ for the RePLIA at various demodulation frequencies. The central column contains the minimum usable time constant and the right hand column details the actual time constants used which were determined by ensuring a near-Lorentzian passband at the relevant demodulation frequency. Note that this table is not exhaustive and longer/shorter time constants and lower/higher demodulation frequencies may be used. 44

4.1 Qualitative comparison of nanodiamonds produced by three fabrication methods. 76

5.1 Electron irradiation parameters for ball milled nanodiamonds. *The expected vacancy production rate was estimated from work conducted by Andrew Edmonds with Warwick University in 2008, as detailed in his thesis.[22] However, the facility used (Synergy Health, Swindon, UK) is not well characterised and so precise irradiation damage rates are prone to a large error. 121

7.1 PODMR data and dimensions obtained via SEM for the four nanodiamonds. R_{max} is the maximum possible distance between the measured NV^- and the surface of the nanodiamond. 164

List of Figures

2.1 The simulated effect of phase difference $\delta\phi$ between the input and reference signals. Vertical bars indicate alternating points where $\delta\phi = \frac{\pi}{2}$ (out of phase) and $\delta\phi = 0$ (in phase). 14

2.2 The effect of a non-zero width passband. Multiple signal components are shown in (a) where red data indicate signals with a slightly higher frequency than the reference (grey line) whilst blue data indicate lower frequency signals. b) shows a summation of the signals in (a) with the corresponding constructive and destructive interference leading to the signal shown. c) shows the magnitude of the signal in (b). d) shows the effect of a moving average filter of four different averaging periods. 17

2.3 Simplified layout of a CLB comprising a look-up table (LUT), flip-flop (FF) and an output and a block of static random-access memory (SRAM).[39] 22

2.4 Simplified schematic of circuitry layout on Red Pitaya lock-in amplifier FPGA. Signals (solid green arrows) are received at channel processing, where they are multiplied by a reference signal generated in the direct digital synthesis (DDS) block, which takes time data (dashed brown arrows) from the timer and distributes it as a reference. After the multiplication, data are passed through a single pole infinite impulse response (IIR) filter, currently limited to a single pass. Filtered data (solid blue arrows) are then passed to the memory allocation block and subsequently to the digital to analogue converters (DACs), converted to analogue data (solid red arrows) and passed out to the user or saved to the random access memory (RAM) where they can be accessed via ethernet (dashed red arrow). The reference signal is extracted from the DACs in analogue form (dashed blue arrow). Operating parameters and modes are set by the user (dashed green arrows), via the command line interface (CLI) which communicates with the mode control block on the FPGA. 24

3.1 Noise spectrum from a) RePLIA at 500 kHz demodulation with a 1 ms time constant (with 1 s data zero padded) and b) HF2LI at 1 MHz demodulation and 700 µs time constant, at 1 second (blue trace), 10 seconds (red trace) and 100 seconds (orange trace) collection time (output data is R for both devices). c) noise level decays with increased collection time, close to the predicted $1/\sqrt{time}$ relationship (top trace) calculated based on noise measured after 1 second of collection. The lower trace indicates theoretical values back calculated from the 100 seconds data point. 36

3.2 FFTs of terminated input data, extracted via file transfer, at various RePLIA demodulation frequencies with 100 s collection time. Two distinct noise regimes seem to exist, with demodulation frequencies above 100 kHz producing significantly lower noise. Time constants were varied dependent on demodulation frequency (see table 3.2). Note that low frequency and high intensity data have been cropped for visual clarity. 37

3.3 Output of frequency sweep for MHz demodulation frequencies for the a) RePLIA and b) HF2LI. c) Maximum output voltage of the RePLIA plotted against demodulation frequency, showing the half power point. Note that the RePLIA has a sampling rate of 125 MHz. 39

3.4 Demodulated RePLIA output against input voltage, operating at 500 kHz demodulation for a ±1 V input range. Solid red line is a linear fit of the 0 to 0.7 V linear region. 40
3.5 a) FFT of 10 kHz demodulation data taken from the RePLIA's DAC outputs, demonstrating significantly greater noise 140 μV/$\sqrt{\text{Hz}}$ than data taken from Ethernet output. b) Output signal to noise from the DAC outputs improves dramatically with demodulation frequency throughout lower frequency ranges due to increased signal. 41
3.6 Fast Fourier transforms of RePLIA input noise at varying DAC multiplier settings (a) with extremes only plotted for clarity (b). c) The signal to noise ratio at the RePLIA's digital-to-analogue outputs increases with larger DAC multiplier. However, even small signals can lead to saturation of these outputs. Data obtained at 500 kHz demodulation frequency and a 10 ms time constant. 42
3.7 The effect of the time constant setting on the resulting passband. An 80 kHz sweep over 10 seconds through the demodulation frequency of 500 kHz at varying time constants results in distortion of the passband. Longer time constants result in fringes in the unwanted frequency regions and shorter time constants result in excessive acceptance of unwanted frequencies. For 500 kHz, a time constant of 1 ms was chosen as a suitable compromise. The small section of the sweep output shown above shows only the part of the passband affected by the time constant. 43
3.8 Low Frequency (1-10 kHz) FFTs of RePLIA input noise from a) 1 second, b) 10 seconds and c) 100 seconds of DAC data. Frequency-specific spikes are common at low demodulation frequency. 45
3.9 FFTs of noise at varying time constant at a demodulation frequency of 500 kHz. 46
3.10 a) RePLIA and b) HF2LI 10 MHz passbands with Lorentzian fits with 2.6 kHz and 2 kHz linewidths respectively. Note that the x-axes cover different ranges for these data. 47
3.11 FFT of signal demodulated at 30 kHz, with a fit of $f(x) = a + b \cdot {}^{1}/_{f}$ where $a = 5.6 \cdot 10^{-5}, b = 0.001$, consistent with flicker noise of the board. 48

3.12 Cross-talk between the two fast input channels was detected using the STEMLab hardware and software. A sine wave input signal was applied at channel A with a significant signal detected at channel B. Note that cross-talk is minimal at lower frequency and was indistinguishable from background noise at input frequencies below 1 kHz. . 48

4.1 The diamond crystal lattice along the three principle axes; a) [100], b) [110] and c) [111]. 52
4.2 Each carbon atom in the diamond lattice is covalently bonded to four identical carbon atoms. 54
4.3 a) Two isolated carbon atoms at an infinite distance have four electrons available for bonding (circles with arrows showing spin) i.e. two electrons in each p-orbital and 2 in each s-orbital. The 2 core electrons are not concerned with bonding and are not shown. b) When two such atoms are brought close together, the p- and s-orbitals overlap and the electrons from the p-orbitals join with those from the s-orbitals to form the sp^3 hybrid state with a band gap E_{gap} up to the antibonding states. 55
4.4 A drawing of the band structure of a semiconductor (adapted from[18]). As the energy levels from multiple atoms accumulate they 'smear out', forming bands. The atomic separation d determines the energy gap (band gap) between the conduction and valence bands. For atomic separations between d_1 and d_2, metallic behaviour (i.e. high electrical conductivity) will be extant. 56
4.5 A simulation of the band structure of diamond adapted from Smith et al.[23] The vertical axis denotes the energy of an occupied or unoccupied state, whilst the horizontal axis shows the 'crystal momentum' or k-vector in the lattice's Brillouin zone. Occupied energy levels reside within the valence band and require an energy greater than or equal to the band gap to make the transition to the lowest unoccupied conduction band energy level. The horizontal offset between the top of the valence band and the bottom of the conduction band shows that diamond is an indirect band gap semiconductor. 58

4.6 Though both diamond and graphite are stable at room temperature and pressure, carbon can be converted from one allotrope to the other by supplying sufficient energy to overcome the energy barrier, or activation energy, between them. This barrier can be reduced by the use of a metal catalyst in HPHT synthesis. 60
4.7 Phase diagram for carbon. Each synthesis method requires specific growth conditions, with two distinct regions for HPHT (using molten metal catalysts to reduce the formation temperature) and HPHT* (without catalysis). Chemical vapour deposition (CVD - see 4.3.2) takes place at comparatively low pressures and temperatures, well within the stable graphite region. It should be noted that the specific temperatures and pressures employed for CVD diamond synthesis have a significant effect on the size, quality and physical & chemical properties of the resulting material. 61
4.8 A schematic diagram of an HPHT press. The seed crystal (1) acts as foundation upon which carbon atoms precipitating from the graphite/-catalyst mixture (2) can undergo homo-epitaxial growth. Pressure (indicated by the arrows) is applied via anvils (3). 62
4.9 Simplified layout of a CVD reactor. Gases entering the vacuum chamber are separated into their constituent atoms by microwave radiation and assist the carbon in being deposited upon the substrate. Cooling may be applied beneath the substrate to control formation parameters. 64
4.10 Varying atomic composition ratios of carbon, hydrogen and oxygen determine the feasibility of diamond growth. Each corner of the triangle denotes 100% composition by a particular element, with a fractional ratio between two elements leading down each edge, and a three element mixture anywhere within the triangle. Adapted from Bachmann, 1991.[55] 65

4.11 One possible mechanism of hydrogen mediated diamond growth in the CVD process. a) In most cases, dangling bonds on the growth surface are simply occupied by atomic hydrogen drawn from the gas mixture. b) However, (ii)sometimes a CH_3 molecule may occupy this site. (iii)A neighbouring H atom may also recombine with a loose H atom to form molecular hydrogen, leaving a dangling bond adjacent to the CH_3. (iv) This dangling bond may also become occupied by a second CH_3 and (v) each of these CH_3s may lose an H atom, becoming CH_2. (vi) The two carbon atoms now each have a spare bond which they now join together, becoming fully part of the diamond surface with two attached hydrogen atoms each, which may now continue the process from step (i). Note that atom sizes, bond lengths and bond angles are not to scale in this diagram. Adapted from[68] and.[67] . . . 67
4.12 Two carbon atoms (C) in the diamond lattice are removed and replaced with a nitrogen atom (N) and a lattice vacancy (V) to form the nitrogen vacancy defect. 68
4.13 Ball milling uses mechanical crushing to reduce diamond precursor to a nanodiamond powder. The drum rotates causing the milling balls to grind the precursor material gradually, with the size distribution of the resulting powder determined by the material of the milling balls, the size of balls and drum and the duration of the milling process. . 71
4.14 In a planetary mill, one or more milling chambers orbit a common centre of rotation on a 'sun' disc. This offset from the centre leads to higher kinetic energy in the milling mixture (balls and precursor material) and greater velocity differences between particles. In a) the milling mixture is falling down the side of the chamber due to gravity, as will a simple mill. However, in b) the rotation of the sun disc means that particles fall from a greater height and are moved with greater force, leading to more effective milling. 72
4.15 Scanning electron microscopy (SEM) image of ball milled nanodiamonds. Dimensions range from a few nanometres to a few microns in diameter. 74
4.16 SEM images (left) of two suspected diamond particles. EDX analysis (right) showed that whilst carbon (most likely diamond) was present at both sites, silicon contamination was also present, in some cases more so than the carbon, suggesting widespread contamination. . . 75

4.17 The ratio of nanodiamond surface area to bulk volume decreases rapidly. 81

5.1 Illustration of the splitting of energies in a lone, unpaired electron under the influence of a magnetic field, where B_0 is the applied magnetic field in EPR. 103

5.2 Functional layout of an EPR spectrometer. Microwave emission from the source enters the circulator at 'a' and exits *only* at 'b', after which it enters the cavity and interacts with the sample. The resultant emission from the cavity returns to the circulator at 'b' and exits *only* at 'c'. The difference between the reference and the signal exiting the circulator forms the output signal, constructed by a detector diode. . 106

5.3 Behaviour of an EPR cavity under various conditions. An unloaded cavity will reflect microwave radiation when not critically coupled (a, c), i.e. the iris is either too large or too small. An unloaded and critically coupled cavity (b), an unloaded and non-critically coupled cavity (d) or a cavity containing a non-absorptive sample (f) will not reflect microwaves. A loaded (and critically coupled) cavity will only reflect microwaves, and therefore generate a signal, when a sample which absorbs at the resonant frequency is present (e). 107

5.4 As the B_0 field is swept, absorption occurs where the magnitude of the field matches the microwave excitation frequency (see eqn. 5.3). A second, oscillating field is applied parallel to B_0 to which a lock-in amplifier is tuned. This modulation scans a small region of the total scanning range at any one time, giving an output signal at the upper extent of the modulation amplitude (a_1) and and an output signal at the lower extent (a_2), leading to the respective outputs s_1 and s_2. The LIA output represents the difference in these values for each 'segment' (modulation amplitude) of the sweep range, leading to the derivative line shape seen in figure 5.5. 108

5.5 Derivative line shape produced by employing a lock-in amplifier to demodulate an EPR signal. 109

5.6 The energy level scheme of the negatively charged nitrogen vacancy centre. Spin conserving optical excitation of the $^3A_2$ triplet ground state[10] to the excited ^3E state leads to relaxation via a red photon (λ_{re}) or spin polarisation to the $m_s = 0$ ground state via inter-system crossing (ISC) and non-radiative relaxation (or the emission of an infrared photon (λ_{ir})) between the singlet states. Resonant microwave excitation can then excite from the $m_s = 0$ ground state to the degenerate $m_s = \pm 1$ ground state. This degeneracy may be lifted by the application of a magnetic field by Zeeman splitting (see section 5.1.2). 'Weak' and 'strong' refer to the relative probability of centres making the transition from either the $m_s = 0$ or $m_s = \pm 1$ excited state through the shelving states. With the spin selective transition from the ^3E level to the $^1A_1$ level, approximately 99% of transitions will be via the 'strong' route, coming from the $m_s = \pm 1$ state and the remaining 1% from the $m_s = 0$ state. 110

5.7 A sketch of the NV$^-$ ODMR spectrum. Each trough in fluorescence represents a formerly degenerate state in the presence of a magnetic field, calculable from equation 5.3. Note that this drawing does not take account of a lock-in amplifier, and so the features are purely absorptive and have no derivative line shape. 111

5.8 Two dimensional model of the collection efficiency of a lens collecting light from an isotropic source in a) a single medium of refractive index n_1 and b) two materials of refractive indices n_1 and n_2. 112

5.9 Bloch sphere for a non-specific two level system. Vectors at either pole are basis states, with other points on the sphere's surface corresponding to superpositions of the two basis states. Mixed states can be represented by vectors which terminate below the sphere's surface. 113

5.10 A two dimensional Bloch sphere representation of a Rabi oscillation sequence (left) with the resulting fluorescence as a function of pulse area (right). Each state or superposition has a characteristic fluorescence which is plotted against the length of the microwave pulse used to initialise that state or superposition. Below are the microwave and laser pulse sequences used for spin initialisation and read out. . . . 114

5.11 The spin echo pulse scheme: the effect of the laser (b) and microwave (c) pulse sequences on the magnetisation vector of the NV$^-$(a). An initial laser pulse prepares the spin by placing it into the $|0\rangle$ state (i). The NV is then placed in a quantum superposition (ii) with a $\frac{\pi_x}{2}$ microwave pulse. Decoherence is accumulated (iii) before a π_x rotates the vector through 180° around the x-axis. The same degree of decoherence is now accumulated again (iv), 180° rotated from the original accumulation, cancelling out the earlier decoherence. The spin echo then occurs (v) and a $\frac{\pi_x}{2}$ readout pulse is then applied to rotate the magnetisation vector (vi) so that it can be detected by measuring the fluorescence from a green laser excitation pulse. This pulse reinitialises the centre (vii) so that the sequence can be repeated. 118

6.1 A simplistic view of an NV magnetometer. Excitation light (green arrows) is directed towards a diamond containing NV centres, which fluoresce omni-directionally (red rings). Some of this fluorescence (red arrows) arrives at the detector. A microwave antenna (not shown) delivers microwave radiation at approximately 2.88 GHz to enable ODMR. The omni-directional nature of the NV fluorescence emission demonstrates the need for optical elements to improve the collection efficiency of this arrangement. 128

6.2 Derivative (a) and purely absorptive (b) ODMR spectra of NV$^-$ ensemble under zero bias field and under an arbitrary bias field aligned along the [1 1 1] axis. The application of the bias field lifts the degeneracy of the $m_s = \pm 1$ state, and the resonances are further split by hyperfine interactions. 129

6.3 Layout of the NV magnetometer built for this research. Optical excitation is delivered and fluorescence collected via a microscope objective. Modulated 2.88 GHz excitation for driving between the $m_s = 0$ and $m_s = \pm 1$ ground state is applied via an antenna to the diamond sample. Fluorescence detection utilises a photodiode whose output is passed to an LIA and subsequently to an oscilloscope. A bias field is provided by a permanent magnet. 130

6.4 The effect of distance between the sensing area (blue squares) and the origin of a field, in this case a permanent magnet. The separation between field lines in the x direction indicates the steepness of the magnetic field gradient. 131

6.5 The surface area of the cap bounded by the circle of radius a at a distance h from the sphere's surface towards its centre, when compared to the sphere as a whole, will give the collection efficiency of the lens. 133
6.6 Resonant excitaion from the $^3A_2$ $m_s = 0$ to the $m_s = 1$ state is driven by resonant microwave excitation, and is further excited to the corresponding ^3E state as with conventional fluorescence detection. Rather than detect fluorescence from photon emission back to the ground state though, absorption by excitation from the ^1A to the ^1E can be used for ODMR. 134
6.7 a) In conventional fluorescence detection, large amounts of signal are lost due to radiation away from the optical path. Similarly, a significant proportion of the signal is directed to the edge of the diamond by total internal reflection (TIR). b) In this hypothetical scheme, only material within the optical path is able to absorb and so no signal is lost, leading to collection efficiency nearing unity. 136
6.8 Layout of proposed design with free space optics (left) and a fibre coupled design (right). 1042 nm probe light is reflected by a silvered surface back through the objective, after which it is deflected from the incident path by a prism to a detector. 137

7.1 The pinhole in a confocal microscope accepts light from the confocal volume near the focal plane and allows it to pass through to the detector (red lines). Light originating outside the confocal volume does not come to focus on the pinhole and so is spread out, with only a small proportion entering the pinhole and the majority being rejected. Note that though the focal plane exists at a defined distance from the objective (the working distance), the confocal volume is an extended region, with the size of this volume being determined by the size of the pinhole, the excitation volume and the characteristics of the objective and any other optical components in the optical path. 144
7.2 In confocal fluorescence microscopy, fluorescence in the sample is stimulated by an excitation beam which is directed into the objective and thus to the sample by a dichroic mirror which also allows fluorescence to be transmitted. Optical filtering reduces back scattered excitation light unintentionally reflected by the dichroic. The sample may be scanned through three dimensions in order to produce a map of the sample. 145

7.3 Layout of the confocal fluorescence microscope. Single photon counting modules (SPCMs) are employed to detect excitation from single NVs. The addition of a single mode fibre to the excitation arm reduces the effects of misalignment and movement within the optical table. 147
7.4 Result of an HBT experiment. The characteristic anti-bunching dip must fall below $g^{(2)}(0) = 0.5$ to be considered a single emitter. Data is fit to $(1-(1+a)\cdot e^{\frac{-|x|}{\tau_1}})+a\cdot e^{\frac{-|x|}{\tau_2}}$ which describes a three-level system where τ_1 is the estimated fluorescence lifetime, τ_2 is the estimated shelving rate of the NV and x is the arrival time of a particular photon. 148
7.5 Illustration of the mapping system in use on the silicon wafer samples. 150
7.6 Nanodiamonds suspended in methanol are sprayed into an upturned glass vial and are allowed to precipitate onto the silicon sample surface. 150
7.7 a) a reflection image of a silicon map and a fluorescence image of the same region (b). The solid black vertical bar is a microwave delivery antenna positioned above the focal plane. Larger squares span 100 µm whilst the smaller cells are 25 µm across. 151
7.8 Scanning electron microscope image of a silicon map before ND deposition. Irregular dark patches are unidentified contamination which was not able to be removed, whilst rectangular dark areas are locations which have been previously imaged under SEM, with the expectation being that electron irradiation from the microscope has modified the silicon dioxide surface. 152
7.9 SEM image of nanodiamonds deposited on the surface of a silicon wafer. The large tracks visible here are part of the grid shown in figure 7.8. 153
7.10 Confocal sample holder with inbuilt coplanar waveguide and antenna for microwave delivery. The mapped region is the area described in section 7.2.2. 154
7.11 Continuous wave ODMR spectrum of ND1 (see fig. 7.13). This spectrum was taken in order to align the bias magnetic field with the symmetry axis of the NV by iteratively altering the magnet position whilst attempting to achieve the lowest possible frequency of the observed resonance (identified by the dip in fluorescence). 155

7.12 Cutting a wafer involved placing a brace (a small cylinder of metal) beneath the wafer and pushing down with a blade, causing the wafer to snap along a scored line. a) When the blade is placed against the target surface (i.e. the side to be imaged), the cutting action causes ridges to form on that surface (b). This can be alleviated by placing the wafer target side down on the brace (c) which results in the ridges being formed on the unused surface (d), meaning that an antenna can sit flush with the target surface. 157
7.13 a) Confocal microscope fluorescence heatmap of sample ND1 overlaid on reflection image. The ND is too small to resolve conclusively on the confocal microscope which is diffraction limited, so SEM imaging (b) is necessary to provide an accurate measurement of ND size. The ND inset is approximately 323 nm at its widest point. c) Fluorescence data overlaid on an SEM image, allowing ODMR data to be matched to specific diamonds. Note that sites distinguishable as multiple nanodiamonds in SEM may appear as single objects in CFM. 158
7.14 Autocorrelation values plotted against photon count rates for 69 nanodiamonds on a single silicon wafer sample. Vertical lines delineate $g^{(2)}(0)$ values corresponding to integer numbers of NVs. Horizontal lines represent average photon counts ($A_{n=x}$ where x is the number of NVs) for NDs in that category. 160
7.15 Rabi oscillations for four NVs in nanodiamond. T is the Rabi period. 161
7.16 a-d) Spin echo measurements from four nanodiamonds. Note that for ND2 (b), fluorescence measurements were taken more frequently, allowing the carbon-13 revival period to manifest in the data, leading to characteristic fringes. For other NVs more sparse data were obtained, leaving only the envelope. 162
7.17 The four nanodiamonds used for these experiments. A circle has been drawn on ND1 whose centre represents the estimated greatest distance an NV may be from the surface. However, it should be noted that as the SEM does not provide a three dimensional image, height data regarding the ND cannot be obtained. The low quality of NDs 2, 3 and 4 is a result of differing experimental conditions preventing the acquisition of high resolution data, namely sample drift due to charging on the sample during SEM imaging and operator inexperience at the time these measurements were taken. 163

8.1 An optical trap suspends a particle where the trapping force f_{trap} equilibriates with a scattering force $f_{scatter}$. A nanodiamond particle is suspended in an optical trap with the direction of weakest confinement and the NV$^-$ spin quantisation aligned along the optical axis. A magnet at z_0 means that the $|-1\rangle$ and $|+1\rangle$ states will be attracted to the centre of the harmonic well to a different degree. The gravitational force mg is oriented at a non-perpendicular angle θ to the optical axis, leading to differing gravitational potentials for the $|-1\rangle$ and $|+1\rangle$ states. As the two states (orange and green circles) oscillate along the z-axis, they accrue a gravitational phase difference. 171
8.2 The forces effective on a dielectric particle in an optical trap when viewed along the y-axis (a) and along the z-axis (b). The electric field maximum sits at the beam waist, marked $\times$. This causes an attractive force f_{trap} which is countered in the z-direction by a scattering force $f_{scatter}$ and by the gravitational force mg in the vertical x-direction. In the y-axis, the trapping force is equal in the positive and negative direction, cancelling itself out. 173
8.3 Numerical aperture of the trapping lens has a direct effect on the trap stiffness and the trapping frequency. 174
8.4 Setup of the optical trap. A 1550 nm trapping beam is amplified by an EDFA before being expanded and then focused to trap a particle. A 1064 nm probe beam is similarly expanded and then travels colinearly with the trapping beam through the trapped sample to a balanced detector. A 532 nm beam is also expanded before being focused on the trapped particle where it stimulates fluorescence from the NV centre. The fluorescence then returns along the excitation path where it is selected by a dichroic mirror before arriving at a detector. 175
8.5 A nanodiamond (indicated by white arrows) suspended in the optical trap. Note that the green light visible does not trap the particle but is used for ODMR. The 1550 nm trapping beam and the 1064 nm probe beam are invisible. 176

8.6 An FFT of balanced detector output, showing trapping frequencies measured with a 0.77 NA aspheric lens using a 1550 nm trapping laser. The x- and y-axes are well separated and the z-axis has a comparatively high trapping frequency of 221.6 kHz. Smaller peaks are thought to correspond to interference and imbalance, such as rotations or torsional motion of the particle.[15] 178
8.7 Left: Three dimensional model of the 3-axis, Helmholtz-type homogeneous magnetic field assembly. The six coils forming the three Helmholtz magnets are supported by an aluminium structure (coloured gold in this model) which also acts as a heat sink for the device. Right: photo of the chamber. Note the addition of silver paste around the coils for improved thermal management. 179
8.8 a) Heating of the z-axis coil captured by thermal imaging camera. b) Heating of the coil assembly over time. The addition of a silver paste at the interface between the assembly and the vacuum chamber reduces the heating rate and maximum temperature of the system. Temperatures were monitored by using a thermal imaging camera whilst the vacuum chamber was unsealed and the lid removed. . . . 180

Acknowledgments

Eight years ago I was working as a chef, with little understanding either of physics or the challenge of writing a thesis. To suggest that such a transition could be made without the help and guidance of many other people would be ludicrous. Firstly, my thanks go to Dr Balázs Pintér at Prifysgol Aberystwyth University, without whose confidence and encouragement I would never have even begun my foray into physics. Also to Prof Andy Evans and Dr Eleri Pryse at the same institution, who both gave me excellent support through my undergraduate studies and who encouraged me to pursue this doctorate. Without these three excellent, supportive academics I would still be arranging salads and buttering bread for sandwiches.

Foremost from my time in Warwick I must thank my supervisor Prof Gavin Morley for his endless patience, tolerance and understanding throughout my time here. Not only has he provided in depth knowledge and guidance essential to my work, he has managed to avoid screaming and calling me names (at least vocally) despite my often trying behaviour. Similar thanks go to Prof Mark Newton, whose expertise and insight have proved invaluable and whose dedication to the Diamond Science and Technology Centre for Doctoral Training has enabled me to undertake and hopefully complete this course.

I would also like to thank the many fellow students and staff in the Warwick Diamond Group, namely Dr Ben Green, who has spent many tireless hours explaining things I should really already understand with great patience; Dr Ben Breeze who has similarly shown great technical expertise and has been the person who always knew where everything was, no matter how trifling, old or insignificant; Dr Angelo Frangeskou and Dr Colin Stephen who tolerated my quirks and foibles in the

office as well as provided much valued assistance across a wide variety of fields; Phil, Enrik, Yash, Raj and James and everyone else in the group who made every day not just about work but also about friendship and thus, more bearable. Particularly I would like to thank Mark Skilbeck, whoso rapidly and effectively programmed the FPGA for the lock-in amplifier.

Finally I must thank my family: Mum and Andrew who have been ever encouraging, loving and supportive; my parents-in-law Dawn and Michael who have never once suggested a real job might have been a better idea, and lastly my wife, Katie, for supporting me emotionally, financially and psychologically through what has been a roller-coaster. Without her none of this, or indeed any of my endeavours, would be possible. I dedicate this thesis to our three beautiful sons, Idris, Merlyn and Gwydion, who have smiled and giggled and encouraged me to do the same every day since they were born. I love you all.

Declarations

I declare that the work presented in this thesis is entirely the product of my own effort except where stated otherwise and was carried out entirely at the University of Warwick, during the period of November 2016 to November 2019, under the supervision of Prof Gavin Morley. The research reported here has not been submitted, either wholly or in part, in this or any other academic institution for admission to a higher degree. Some parts of the work reported and other work not reported in this thesis have been published as listed below. It is anticipated that further work will be submitted for publication in due course.

Publications

G. A. Stimpson, M. S. Skilbeck, R. L. Patel, B. L. Green, and G. W. Morley. An open-source high-frequency lock-in amplifier, *Review of Scientific Instruments* **90**, 094701 (2019).

R.L. Patel, L.Q. Zhou, A.C. Frangeskou, G.A. Stimpson, B.G. Breeze, A. Nikitin, M.W. Dale, E.C. Nichols, W. Thornley, B.L. Green, M.E. Newton, A.M. Edmonds, M.L. Markham, D.J. Twitchen, and G.W. Morley. Subnanotesla Magnetometry with a Fiber-Coupled Diamond Sensor. *Physical Review Applied* **14**, 044058 (2020).

B. D. Wood, G. A. Stimpson, J. E. March, Y. N. D. Lekhai, C. J. Stephen, B. L. Green, A. C. Frangeskou, L. Gins, S. Mandal, O. A. Williams, S. Bose, G. W. Morley. Matter and spin superposition in vacuum experiment (MASSIVE). arXiv:2105.02105

Conferences

"Spin decoherence in high-purity nanodiamonds and digital signal processing for diamond magnetometry" 69th Annual Diamond Conference, Warwick University. (2019)

Abstract

This thesis presents research into the characteristics necessary for diamond and nanodiamond in the application of optically detected magnetic resonance (ODMR) for sensitive magnetic field detection, magnetocardiography, quantum computing and fundamental physics research and also addresses digital signal processing requirements for some of these applications.

Firstly, an open source, high frequency lock-in amplifier is presented, along with characterisation that demonstrates a sensitivity of $90\,\mathrm{nV}/\sqrt{\mathrm{Hz}}$ and a maximum demodulation frequency of 50 MHz. This device is compared with a commercial alternative, and its suitability for diamond magnetometry in magnetocardiography is discussed. Secondly, confocal fluorescence microscopy measurements of nitrogen vacancy centres in high purity nanodiamond are presented, along with a discussion of the nanoparticles' suitability for fundamental physics experiments. T_2 spin-spin decoherence times of up to 120 µs are reported, achieved using the spin echo method, twenty times longer than previous research using high yield nanodiamonds. These experiments were performed on nanodiamonds deposited on a custom designed silicon substrate marked with a simple grid for location enabling the measurement of specific nanodiamonds not only in confocal fluorescence but also under scanning electron microscopy.Finally, progress is made towards optical trapping of these nanodiamonds for the investigation of the macroscopicity of particles in a spatial quantum superposition. Trapping frequencies of 220 kHz using an aspheric lens were achieved, and a three-axis Helmholtz coil was constructed and thermally tested in aid of applying ODMR to trapped nanodiamonds.

Abbreviations

ADC	Analogue-to-digital converter
AOM	Acousto-optic modulator
ASIC	Application specific integrated circuit
μ_B	Bohr magneton ($9.274 \times 10^{-24}\,\mathrm{JT}^{-1}$)
CFM	Confocal fluorescence microscope
CLB	Configurable logic block
COM	Centre of mass
CPMG	Carr-Purcell-Meiboom-Gill (pulse sequence)
CVD	Chemical vapour deposition
CW	Continuous wave
DAC	Digital-to-analogue converter
DC	Direct current
DDS	Direct digital synthesis
DSAS	Detonation shockwave assisted synthesis
ECG	Electrocardiography
EDFA	Erbium doped fibre amplifier
EPR	Electron paramagnetic resonance
ϵ_0	Permittivity of free space ($8.854 \times 10^{-12}\,\mathrm{m}^{-3}\mathrm{kg}^{-1}\mathrm{s}^4\mathrm{A}^2$)
FFT	Fast Fourier transform
FPGA	Field programmable gate array
FWHM	Full width at half maximum
g_e	Landé g-factor
GUI	Graphical user interface

HBT	Hanbury Brown-Twiss (autocorrelation measurement)
HDL	Hardware description language
HPHT	High pressure high temperature
HPLC	High performance liquid chromatography
IIR	Infinite impulse response
ISC	Intersystem crossing
LIA	Lock-in amplifier
LP	Long pass (filter)
LTDW	Light trapping diamond waveguide
LUT	Look-up table
MCG	Magnetocardiography
MM	Multi-mode (optical fibre)
MSR	Magnetically shielded room
NA	Numerical aperture
ND	Nanodiamond
NMR	Nuclear magnetic resonance
NV	(negative) Nitrogen vacancy (centre)
ODMR	Optically detected magnetic resonance
RAM	Random access memory
RePLIA	Red Pitaya lock-in amplifier
SBC	Single board computer
SEM	Scanning electron microscope / microscopy
SM	Single mode (optical fibre)
SNR	Signal-to-noise ratio
SOC	System on a chip
SPCM	Single photon counting module
SQUID	Superconducting quantum interference device
USB	Universal serial bus
ZFS	Zero field splitting

Chapter 1

Introduction

1.1 Expecting the Unexpected

1.1.1 An Unexpected Journey

Diamond has been known since antiquity, and its perceived rarity and beauty have led to its unparalleled status as a symbol of wealth, success and enrichment. However, that the value of diamond as a material might exceed the aesthetics for which it is renowned cannot have been imagined back when it was first discovered millennia ago in antiquity.[1] However, the first clues as to diamonds' usefulness other than something at which to gaze, perhaps first came many millennia ago when they were used as engraving tools. This early observation of the gemstone's superlative hardness[2] is reflected in the widespread use today of diamond in industrial applications, where its extreme cutting and grinding capability has given it prized status nearly equalling that conferred by its aesthetic value.

That diamond could have valuable contributions to make in fields as diverse as geological dating,[3] medical imaging[4] and fundamental physics research[5, 6] would have been an outlandish idea only fifty or a hundred years ago. However, the clues to these uses for diamond have been there for all to see for many years. Jewellers and collectors have long sought 'flawless' clear diamonds, but even above these they have prized coloured diamonds. Once the origin of these attractive colours was guessed at, the journey towards manipulating and exploiting these 'colour centres' as they have become known, had begun.

In 1909, Sir William Crookes discovered that colouration of diamonds could be achieved by irradiation with radium atoms,[7] suggesting that the gemstones' interaction with light was mediated by the atomic configuration of the substance's crystal lattice. Further understanding of the effects of radiation bombardment came in the 1950's[8, 9, 10] when there was a significant amount of work investigating the effects of using different particles and varying particle energies for bombardment. Not only

did this early research begin to probe methods of effecting colour change in diamond, but it began to speculate as to the mechanisms taking place which enabled the changes.[11] More than 100 years prior to Crookes' work however, research was taking place which would revolutionise not only physics as a whole, but would also impact the future of diamond itself.

1.1.2 An Unexpected Destination

When Thomas Young performed his famous 'double slit' experiment in 1801,[12] the ramifications were not immediately clear. In fact, the experiment instead seemed to confirm that light merely propagated as a wave, a concept which, advanced by Descartes nearly two centuries earlier,[13] found many willing adherents. The competing hypothesis, that light (and indeed all things) was comprised of particles, had existed since antiquity. It was not until the late nineteenth and early twentieth centuries that it began to emerge that these competing hypotheses were not mutually exclusive. What this apparent dichotomy demonstrated was that things could, quite literally, not be what they seemed. More specifically, the work of Bohr,[14] Planck,[15, 16, 17] Heisenberg[18, 19, 20] and a great many others in the early 1900s showed that there were two regimes that seemed yo underpin the physical universe.

The great prize in modern physics has been, since these pioneering days, the unification of quantum mechanics with general relativity. The bringing together of these seemingly irreconcilable disciplines has produced some of the most notable headaches and disagreements in the scientific community, prompting Einstein to offer perhaps his most famous quotation in a letter to Max Born in 1926 in response to Born's and Heisenberg's work; "I, at any rate, am convinced that He [God] does not throw dice". Regardless of Einstein's protestations though, the study of physics has since arrived at the inescapable conclusion that both quantum mechanics and general relativity are eminently demonstrable yet mutually incompatible, and so the

search for the underlying relationship between these theories continues.

1.1.3 An Unexpected Alliance

Initial research on colour centres in diamond has found impetus from the gemological community who, by and large, have sought better understanding of diamond on an atomic and crystallographic level in order to better comprehend, identify and weed out artificial gemstones which find their way onto the black market and, increasingly, otherwise legitimate trade. That it should be this commercial driver which has led to the study of diamond for more fundamental research is perhaps the most unexpected result of these two seemingly disparate avenues of enquiry, gemmology and quantum physics.

The confluence of these two interests is embodied by the negatively charged nitrogen vacancy (NV^-)defect, the replacement of two adjacent carbon atoms in the diamond lattice by a nitrogen atom, a lattice vacancy and an extra unpaired electron. With an electron spin of $S = 1$ and a ground state splitting between $m_s = 0$ and $m_s = \pm 1$, this crystallographic defect is responsible for creating gems of purplish hue and gives rise to fluorescence in the red part of the visible spectrum where the intensity of fluorescence depends on the spin state. This fluorescence is the tell-tale sign of something deeper, and it is this which is of interest to not only researchers probing fundamental physics, but also to those pursuing the real-world applications of quantum mechanics. By being placed into a superposition of two quantum states, the unpaired electron of the nitrogen vacancy centre opens itself up as both a tool for probing the quantum nature of gravity[5] and as the potential building block of a quantum computer.

Quantum computing, and quantum information in general, relies of the use of quantum bits, or qubits. Coarsely analogous to classical bits in an ordinary computer, which may have values of 0 or 1, a quantum bit may be placed into a quantum

superposition of $|0\rangle$ and $|1\rangle$, dramatically increasing the potential speed and complexity of calculations. The nitrogen vacancy can provide just such a qubit in the form of an unpaired electron, i.e a single quantum spin, which may be accessed, manipulated and read out by comparatively simple means. Where the nitrogen vacancy truly excels in comparison to competing technologies is its capability for such operations at room temperature as opposed to cryogenic temperatures as is the case with some other qubits.

The nitrogen vacancy has attracted interest from many scientific disciplines, hinting at the diversity of potential applications for which it may be suitable. Perhaps then it should be little surprise that the study of something so ancient and universally acknowledged as diamond might lead to the development of some of humanity's most ambitious technology.

1.2 Motivation

A particle suspended in an optical trap can be among the simplest of experiments. In the most elementary of cases it represents at its heart a sphere in a vacuum; the ideal system for a physicist to probe. It is the simplicity of this system which lends itself to the investigation of quantum mechanical behaviour in mesoscopic objects.

By removing the air from the system and any mechanical interaction, the opportunities for wave function collapse when manipulating a levitated nanoparticle in a spatial superposition are greatly reduced. Diamond containing nitrogen vacancy centres offers yet another simplistic system (i.e. one where the nitrogen vacancy is suspended by a network of largely inert material in the form of the mostly non-paramagnetic carbon diamond lattice) which can be coupled to the levitated particle in order to enable the superposition in the first place. It would seem then, that with the application of some well understood physics, the boundary between classical and quantum theory could be explored.

However, as has so often been the case in scientific inquiry, the difficulty has been found in the detail. Vacua are inevitably incomplete, nanodiamonds are uncompromisingly non-spherical and their crystal lattices are rarely as pure as would ultimately be desired.

Concepts for matter-wave interferometry experiments making use of nanodiamonds in optical traps have been proposed.[5, 6] These see the electron spin of a nitrogen vacancy coupled with the mechanical oscillations of a levitated nanodiamond via an inhomogeneous magnetic field. So coupled, if the nitrogen vacancy spin is placed into a quantum superposition of its quantum states, it has been proposed that the oscillatory state of the nanodiamond to which it is coupled will also be in a superposition. This could be confirmed with an interference experiment by tilting the apparatus leading to the two states experiencing different gravitational potentials. These states could then be read out by optically detected magnetic resonance.

This experiment though relies upon several factors:

1. the nanodiamond must remain trapped for long enough that optically detected magnetic resonance can be observed, ideally several hours or longer,

2. the diamond must remain in a spatial superposition for long enough for an experiment to be performed, dependant on the particular operating procedures used,

3. the electronic spin state of the nitrogen vacancy centre must remain in its superposition long enough for an experiment to be performed, also dependent on the particular experimental procedures.

Work by Frangeskou et al[21] showed that point 1 could be addressed by reducing the substitutional nitrogen concentration of the diamond material, thereby reducing absorption of energy from the trapping beam and preventing destruction of the diamond by graphetisation. Point 2 may be addressed by reducing the gas pressure

surrounding the particle in order to reduce mechanical interactions between the particles and the gas. The research detailed in this thesis, alongside the demonstration of magnetometry techniques for which the nitrogen vacancy is also useful, will attempt to show that point 3 may also be dealt with by the same measures as point 1; by reducing the nitrogen content of the diamond material. Low numbers of nitrogen impurities and correspondingly low concentrations of nitrogen vacancies are expected to lead to high purity nanodiamonds with (T_2) spin-spin coherence times exceeding 60 µs. Furthermore it is shown that such diamonds may be fabricated using comparatively simple methods, in contrast to other nanodiamonds which require complex synthesis processes.

In parallel with the work on nitrogen vacancy centres, this thesis also describes an open source, high frequency lock-in amplifier which was developed as an aid to nitrogen vacancy magnetometry which was characterised by myself. Whilst the link between these two technologies might not be immediately apparent, it should be realised that lock-in amplifiers are invaluable in the extraction of weak signals from noisy environments, a circumstance which is certainly to be found in nitrogen vacancy electron paramagnetic resonance. The open source option detailed here provides the potential for dramatically reduced cost in this area, which is of particular interest where large numbers of diamond detectors are required.

1.3 Thesis structure

This thesis is divided into two principal sections; chapters 2 to 4, discussing lock-in amplification, nanodiamonds and electron paramagnetic resonance, provide the background theory and experimental detail upon which the later chapters rely. Chapters 5 to 8, addressing diamond magnetometry, lock-in characterisation, con-

focal microscopy and optical trapping, deal more heavily in results, although some theory is included where expansion on earlier concepts is required.

The research itself is also divided into two streams; optically detected magnetic resonance and lock-in amplification. Whilst these two seemingly disparate topics may seem unrelated, chapter 6 highlights the connection between them, and the important role lock-in amplification has to play in magnetocardiography. These two streams are presented alongside one another, in order to preserve the structure as aforementioned. Finally chapter 9 summarises and concludes this thesis.

Chapter 1 References

[1] J. W. Hershey. *The Book of Diamonds.* Hearthside Press, 1940.

[2] J. Haines, J.M. Leger, and G. Bocquillon. Synthesis and design of superhard materials. *Annual Review of Materials Research*, 31:1–23, 2001.

[3] S. B. Shirey and J. E. Shigley. Recent Advances in Understanding the Geology of Diamonds. *Gems & Gemology*, 49(4):188–222, 2013.

[4] T. Murai, T. Makino, H. Kato, M. Shimizu, T. Murooka, E. D. Herbschleb, Y. Doi, H. Morishita, M. Fujiwara, M. Hatano, S. Yamasaki, and N. Mizuochi. Engineering of Fermi level by nin diamond junction for control of charge states of NV centers. *Appl. Phys. Lett.*, 112:111903, 2018.

[5] M. Scala, M. S. Kim, G. W. Morley, P. F. Barker, and S. Bose. Matter-wave interferometry of a levitated thermal nano-oscillator induced and probed by a spin. *Phys. Rev. Lett.*, 111:180403, 2013.

[6] Zhang-qi Yin, Tongcang Li, Xiang Zhang, and L. M. Duan. Large quantum superpositions of a levitated nanodiamond through spin-optomechanical coupling. *Phys. Rev. A*, 88:033614, 2013.

[7] Sir William Crookes. On the action of radium emanations on diamond. *Proceedings of the Royal Society of London*, 74(47):497–506, 1905.

[8] J. M. Cork. Induced color in crystals by deuteron bombardment. *Phys. Rev.*, 62:80–81, 1942.

[9] R. A. Dugdale. The colouring of diamonds by neutron and electron bombardment. *British Journal of Applied Physics*, 4(11):334–337, 1953.

[10] Peter Pringsheim and Ruth Casler Voreck. Farbzentren in Diamanten. *Zeitschrift für Physik*, 133(1-2):2–8, 1952.

[11] C. D. Clark, R. W. Ditchburn, and H. B. Dyer. The Absorption Spectra of Natural and Irradiated Diamonds. *Proceedings of the Royal Society of London Series A*, 234(1198):363–381, 1956.

[12] E. Tretkoff, J. Ouelette, and A. Chodos. May 1801: Thomas Young and the Nature of Light. *APS News*, 17(5), 2008.

[13] A. Wright. Debate on the character of light. *Nature Milestones*, 1, 2010.

[14] N. Bohr. On the constitution of atoms and molecules. *The London, Edinburgh, and Dublin Philosophical Magazine and Journal of Science*, 26(151):1–25, 1913.

[15] M. Planck. Zur theorie des gesetzes der energieverteilung im normalspectrum. *Verhandlungen der Deutschen Physikalischen Gesellschaft*, 2:237, 1900.

[16] M. Planck. Über das gesetz der energieverteilung im normalspektrum. *Annalen der Physik*, 309(3):553–563, 1901.

[17] M. Planck. Zur Geschichte der Auffindung des physikalischen Wirkungsquantums. *Naturwissenschaften*, 31(14-15):153–159, 1943.

[18] W. Heisenberg. Über quantentheoretische Umdeutung kinematischer und mechanischer Beziehungen. *Zeitschrift für Physik*, 33(1):879–893, 1925.

[19] Zur Quantenmechanik. *Zeitschrift für Physik*, 34(1):858–888, 1925.

[20] M. Born, W. Heisenberg, and P. Jordan. Zur Quantenmechanik II. *Zeitschrift für Physik*, 35(8-9):557–615, 1926.

[21] A. C. Frangeskou, A. T. M. A. Rahman, L. Gines, S. Mandal, O. A. Williams, P. F. Barker, and G. W. Morley. Pure nanodiamonds for levitated optomechanics in vacuum. *New Journal of Physics*, 20, 2018.

Chapter 2

Lock-in Amplifiers

2.1 Introduction

The lock-in amplifier (LIA) has become a mainstay of digital signal processing (DSP) in scientific research, being capable of extracting meaningful data from noisy environments, even where the level of noise is much larger than that of the desired signal.[1] First described in 1941, early LIAs were based on heaters, thermocouples and transformers.[2] More modern LIAs have been fully digital[3, 4, 5, 6] or implemented on field programmable gate array (FPGA) devices,[7, 8, 9] which are able to exceed the performance of their analogue counterparts.[10] However, the cost of modern LIAs may prove prohibitive, particularly in cases where large numbers of input channels or high demodulation frequencies are required.

2.2 Principles of operation

2.2.1 Theory

Characterised by wide dynamic range and the ability to extract signal from noisy environments,[11] LIAs are phase sensitive detectors.[12] Generally:

$$V = V_{in}V_{ref}sin(\omega_{in}t + \phi_{in})sin(\omega_{ref}t + \phi_{ref}) \tag{2.1}$$

where the signal V is the product of an input signal V_{in} and a reference signal V_{ref}, where these signals are sinusoidal waves. This results in two alternating current (AC) signals. Firstly a difference frequency $\omega_{ref} - \omega_{in}$ (the reference frequency ω_{ref} and the signal frequency ω_{in}) which results in a DC signal when $\omega_{ref} = \omega_{in}$. Secondly there is a sum frequency $\omega_{ref} + \omega in$ which results in a high frequency component. The addition of a low pass filter results in:

$$V_{out} = \frac{1}{2} V_{in} V_{ref} cos(\phi_{in} - \phi_{ref}) \tag{2.2}$$

such that where the phase difference $\delta\phi = \phi_{in} - \phi_{ref} = 0$ the output will be maximised and where $\delta\phi = \frac{\pi}{2}$ the output will be zero (see figure 2.1). The high frequency component resulting from the sum frequency will be mitigated by the low pass filter.

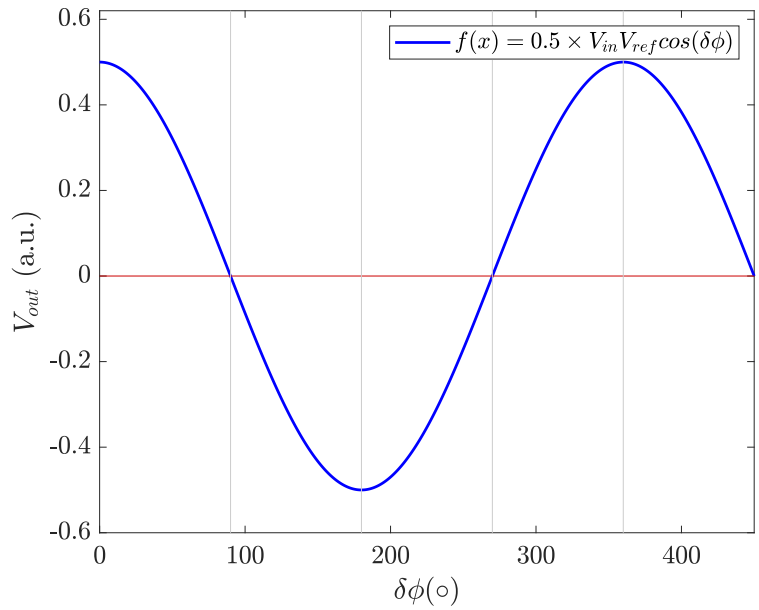

Figure 2.1: The simulated effect of phase difference $\delta\phi$ between the input and reference signals. Vertical bars indicate alternating points where $\delta\phi = \frac{\pi}{2}$ (out of phase) and $\delta\phi = 0$ (in phase).

The reference signal is generated either internally by the LIA itself or externally by some other source. The reference is multiplied by the input signal[13] which carries the desired data modulated at the reference frequency.[14] Where the frequency of the input signal does not equal the reference, and is integrated over a time large

compared to the period of the reference, the output will approach zero. Conversely, where the input frequency matches that of the reference, the output is equal to half the product of the amplitudes of the reference and input signal,[15] meaning that only signals modulated at a frequency equal to that of the reference will be amplified, and other frequencies will be attenuated.[16] Components out of phase with the sine reference will also be attenuated, due to orthogonality of the sine and cosine functions of equal frequency[17] (see equation 2.2), hence the LIA is considered phase sensitive.[18] In a single phase LIA, components in phase with the sine function will result in a non-zero value in the output called X ($X = V_{sig}\cos(\phi)$ where V_{sig} is the voltage of the input signal), whilst in a dual phase LIA, as well as X those components in phase with the cosine function will produce a non-zero value in the output called Y ($Y = V_{sig}\sin(\phi)$), hence the two outputs X and Y can be combined by:

$$R = \sqrt{X^2 + Y^2} \tag{2.3}$$

to provide a magnitude value,[19] while phase $\delta\phi = \phi_{in} - \phi_{ref} = \arctan\frac{Y}{X}$.

Practically then, this leads to a circumstance where only signals which change in intensity at the frequency of the reference (often called the (de)modulation frequency) are accepted and amplified by the LIA, to the exclusion of signals not varying at this frequency. Frequencies close to the demodulation frequency will also be accepted and amplified, but with an amplitude I_{out} which decreases approximately as:

$$I_{out} = \frac{1}{2\pi}\frac{\Gamma}{(\nu - \nu_0)^2 + (0.5\Gamma)^2} \tag{2.4}$$

where ν is the input frequency, ν_0 is the demodulation frequency and Γ is a term related to the output bandwidth.

Finite passband

This finite passband is not smooth. Instead it is populated by multiple peaks of decreasing magnitude either side of the central frequency. These fringes originate from the constructive and destructive interference caused by a continuum of permitted frequencies either side of the reference frequency. This effect can be seen in figure 2.2 where the effect of frequencies deviating from the passband central frequency (i.e. the reference frequency) by small amounts can be seen. In part (a), 101 cosinusoidal signals are modelled, with 50 at incrementally higher frequencies than the reference, the reference itself and 50 signals with slightly lower frequency than that of the reference. These represent signals which have not been rejected by the LIA, i.e. a finite passband. For simplicity of the illustration, the amplitudes of these signals have been set to unity, although in reality we might expect a variety of amplitudes. Part (b) shows the effect of combining the signals passed in part (a) by simple summation. The resulting amplitude of signal then represents the effect of both constructive and destructive interference of the summed signals. Part (c) shows the 'R' value, i.e. the square root of the squares of the components of the signal in part (b) (see equation 2.3), or the magnitude of the signal. Part (d) shows the effect of a moving average filter on the signal in part (c). Here it can be seen that smoothing of the signal comes at the expense of line width. Note that part (a) in this figure displays only a short length of time, compared to the larger range shown in parts (b-d), enabling the individual peaks and troughs to be seen.

It could be supposed that a continuum of frequencies, rather than a large number of discrete frequencies as used in this simulation, may not produce the same effect. Modelling a continuum on a computer is non-trivial, however, and so a real-world

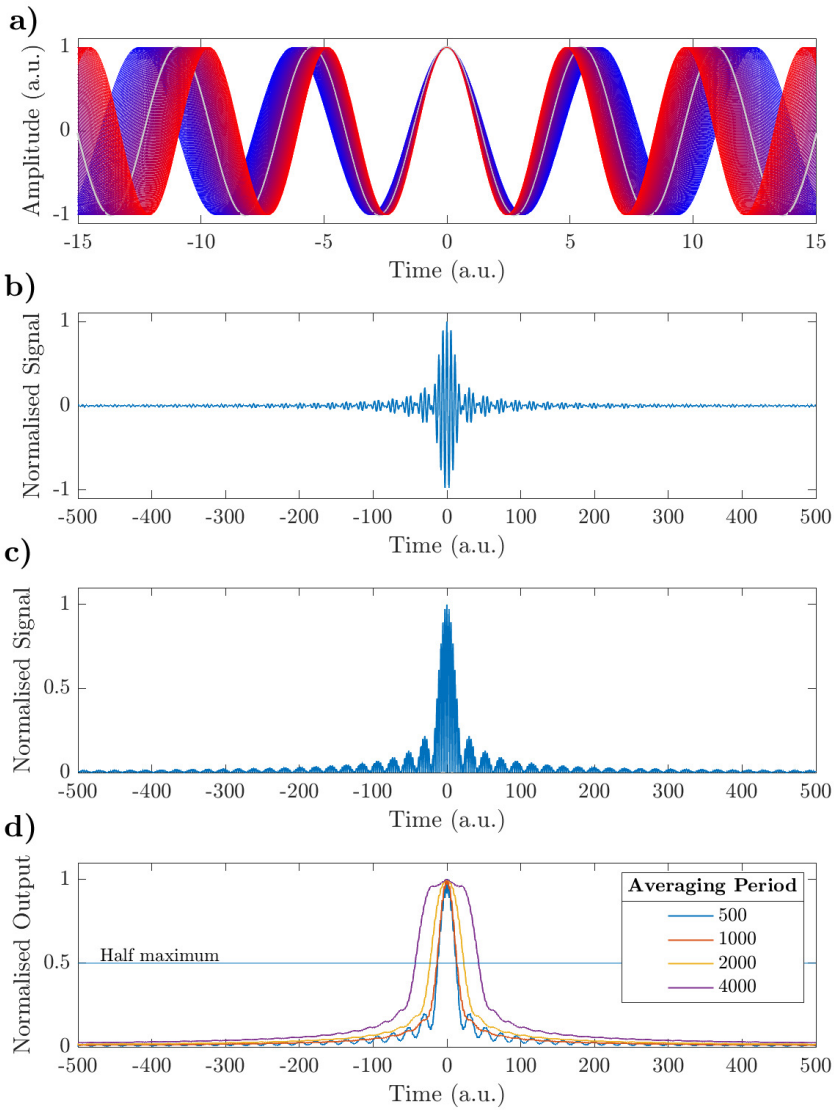

Figure 2.2: The effect of a non-zero width passband. Multiple signal components are shown in (a) where red data indicate signals with a slightly higher frequency than the reference (grey line) whilst blue data indicate lower frequency signals. b) shows a summation of the signals in (a) with the corresponding constructive and destructive interference leading to the signal shown. c) shows the magnitude of the signal in (b). d) shows the effect of a moving average filter of four different averaging periods.

analogy is useful in the form of a beam of light passing through a single slit which, incident on a screen or detector, produces both the fringing and the finer detail in the fringes. The passband used for the model (and in a real system) restricts the passage of signals in the frequency space whereas the single, physical split operates in real space, but the effect is the same. This shows that the fringing seen in non-averaged data from a finite passband is not produced solely by the physical hardware of the filtering device (an LIA for example) but as a fundamental result of imposing a passband upon a signal containing multiple frequency components. The detail in the fringes (which are coloured in the optical example if white light is used or are absent with monochromatic light) are, both in this model and real examples, determined by parameters such as sample rate, time constant and frequency resolution.

The fringing effect caused by a non-zero width passband can, as shown, be mitigated by the use of a moving average filter. However, when such a filter was implemented, I found that an unacceptable trade-off had to be made between fringes in the output signal and excessive bandwidth. To improve this, an infinite impulse response (IIR) filter was implemented by Mark Skilbeck. All results presented in chapter 3 were performed by myself and were conducted using the IIR filter. The simulations presented in figure 2.2 were performed by myself using Matlab 2019b.

2.2.2 Practical considerations

Operation of an LIA requires an understanding of the system or systems being measured. The appropriate modulation frequency for an incoming signal can be affected by processes specific to the measured system. If we consider a system where a component being modulated requires a certain time to respond to a stimulus, modulation on timescales fast compared to the response time might be inappropriate. It is important then that modulation frequencies not comparable to the timescales of these processes are chosen.

Similarly, the operator must be aware of the importance of correct parameter setting, particularly in terms of the relationship between the LIA time constant (i.e. the filter's averaging period) and demodulation frequency. As the time constant behaves as an averaging period, it is essential to ensure that sufficient modulation periods (say, ten) occur within the period encompassed by the time constant:

$$\tau_{min} = \frac{10}{\nu_{mod}} \tag{2.5}$$

where τ is the minimum effective time constant or averaging period in seconds and ν_{mod} is the demodulation frequency in Hertz.

The amplitude of the modulation must also be chosen carefully. Excessive modulation amplitudes can broaden features leading to information loss, and can also potentially cause physical damage depending on the nature of both the system being measured and any circuitry used.

2.3 Hardware

2.3.1 The STEMlab 125-14

The Red Pitaya STEMlab 125-14 is a single board computer (SBC) with an integrated field programmable gate array (FPGA) in the form of a Xilinx Zynq 7010 SOC,[20] allowing for the implementation of reprogrammable micro-architecture which would otherwise necessitate dedicated hardware. The reprogrammability[21] of FPGAs makes them applicable for the LIA functionality described here and allow for further expansion and modification by end users. Two DC coupled analogue inputs are available in the form of user selected $\pm 1\,\mathrm{V}$ or $\pm 20\,\mathrm{V}$, $125\,\mathrm{MS/s}$ analogue-to-digital converters (ADCs) with $1\,\mathrm{M\Omega}/10\,\mathrm{pF}$ input impedance/capacitance. Further hardware specifications can be found in table 2.1.

Processor	Dual Core ARM Cortex A9
FPGA	Xilinx Zynq 7010 SOC
RAM	512 MB
System Memory	$\leqslant$ 32 GB Micro SD
Power Consumption	7.5 W
Data Transfer Rate	1 Gbps
USB version	2.0
Synchronisation	SATA ($\leqslant$ 500 Mbps)
Sample rate	125 MSs^{-1}
ADC/DAC resolution	14-bit
Input impedance	1 MΩ
Input capacitance	10 pF
Input voltage range	±20 V
Load impedance	50 Ω
Output voltage range	±1 V
Output slew rate	200 $\mathrm{V\mu s}^{-1}$

Table 2.1: STEMlab 125-14 hardware specifications

2.3.2 Zurich Instruments HF2LI

Comparison is made with the Zurich Instruments HF2LI LIA, which is specified for operation up to 50 MHz demodulation frequency.[22] Whilst an extensive software application is provided with the HF2LI, the open source nature and readily available software and hardware of the RePLIA allow for an attractive option where cost is a consideration. Research into low-cost FPGA based LIAs has produced a number of alternatives[23] to commercial options, including high frequency-resolution designs operating at up to 6 MHz demodulation,[24, 25] and simulations have been presented for a high frequency LIA based on the Red Pitaya STEMlab.[26] Typically, FPGA LIAs have been developed with specific experimental objectives.[27, 28, 29] The STEMlab is the basis for a range of related measurement instrumentation from PyRPL, including an LIA.[30, 31, 32] A low cost FPGA-based LIA has also been developed which operates at low demodulation frequency,[33] and FPGA-based LIAs have been compared with analogue devices in terms of signal accuracy.[34] However, it is believed that this work is the first to characterise a high frequency, open source LIA.

The open source code may lead to a range of future uses in research, education and industry.

2.4 Field programmable gate arrays

First introduced in the 1980s,[35] FPGAs are mass manufactured integrated circuit devices which, in contrast with conventional microelectronics, can be programmed and reprogrammed by the end user.[36] This programming, more akin to rewiring of the hardware than pure logical programming, is applied to the FPGA using widely available, often freely distributed software as opposed to specialist hardware, enabling rapid prototyping and repeated reconfiguration of the device at any stage during design, implementation and use. However, this flexibility comes at the cost of operating speed when compared to application specific integrated circuits (ASICs)[37] which are produced with a single configuration and cannot be modified.

2.4.1 Principles

An FPGA consists of two principle elements, namely configurable logic blocks (CLBs) and internal circuitry.[38] CLBs are physical elements of the FPGA device which can be programmed to represent logic gates and interconnected by the internal circuitry. CLBs vary from device to device but in general will control the number of inputs and outputs and will, in their number, determine the ultimate processing capacity of the device. In figure 2.3 the basic layout of a CLB can be seen. A look-up table (LUT), a predefined truth table, will determine the response to input values (4 in the diagram). This result will be implemented by a 'flip-flop' which synchronises logic and stores logical states between the device's clock cycles. The output of the flip-flop, either 0 or 1, can then be output, can be stored in static random-access memory (SRAM), or both.[39] It is the LUTs which enable the reprogrammability of FPGAs. However, in most cases the user / programmer does not

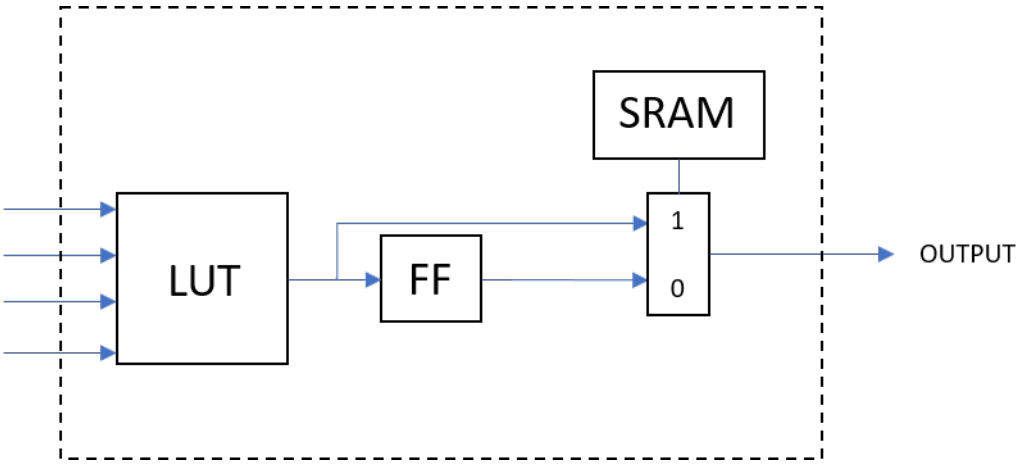

Figure 2.3: Simplified layout of a CLB comprising a look-up table (LUT), flip-flop (FF) and an output and a block of static random-access memory (SRAM).[39]

require knowledge of this underlying architecture to design and implement changes. Instead, graphical user interface (GUI) based software[40] and hardware description languages (HDLs) such as Verilog[41] can be employed to reduce the implementation of harware based algorithms to coding problems, rather than electronic engineering exercises.

2.4.2 LIA Implementation

Signals received by the ADCs are passed to processing blocks (figure 2.4) where they are multiplied by the sine and cosine multiplications (see equation 2.1), which has a fixed phase relationship with the modulation, is generated internally by direct digital synthesis (DDS) and filtered using a single pole infinite impulse response (IIR) filter. The resulting output is written to the STEMlab's random access memory (RAM) via the FPGA's memory interface block. These data are written to a ramdisk file also contained within the host's RAM, alleviating high read/write workloads which were observed to cause critical failures of the SBC's flash memory. The data are also passed to on-board digital-to-analogue converters (DACs) along with the reference signal which is used to modulate the input signal. This reference can be extracted

via the DAC output for external use.

2.4.3 Hardware & software

The FPGA system design and implementation was performed using software provided by the manufacturer of the FPGA, Xilinx. A simplified version of the design circuitry block diagram can be seen in figure 2.4. This was conceived and programmed by Mark Skilbeck who was a postdoctoral researcher in Gavin Morley's group. All characterisation of the device was performed by myself as well as the writing of the data acquisition software to interface with the RePLIA.

Data retrieval from the STEMlab can be achieved via the DACs which are provided with SMA connections for output to a digital oscilloscope and/or computer. These DACs have 14-bit resolution combined with a maximum 125 MS/s data rate. Non-offset, digital amplification of up to two thousand times the DAC output is available. However, unexpected noise introduced by the DACs makes the output undesirable in cases where small changes in signal intensity are to be detected. The origin of this noise was not experimentally determined, though the suspicious was that interactions between the STEMLab and electrical equipment in close proximity could be to blame. Alternatively, data may be transferred to a host PC via file transfer from the STEMlab's RAM. This produces low noise data but can only be performed on the entirety of data stored in RAM simultaneously, approximately 65 megabytes as limited by the FPGA code. In future iterations of the RePLIA this could potentially be increased depending on other processing demands. Whilst this process may last for tens of seconds, all data (X, Y, R and ϕ) for both output channels is received simultaneously. Further limitations include the inability to operate using an external lock-in reference, cross-talk between the two DC coupled fast input channels (see section 3.2.1) and no facility for subtraction of channels (e.g. A-B). Due to the programmable nature of the STEMlab, end users are able to implement

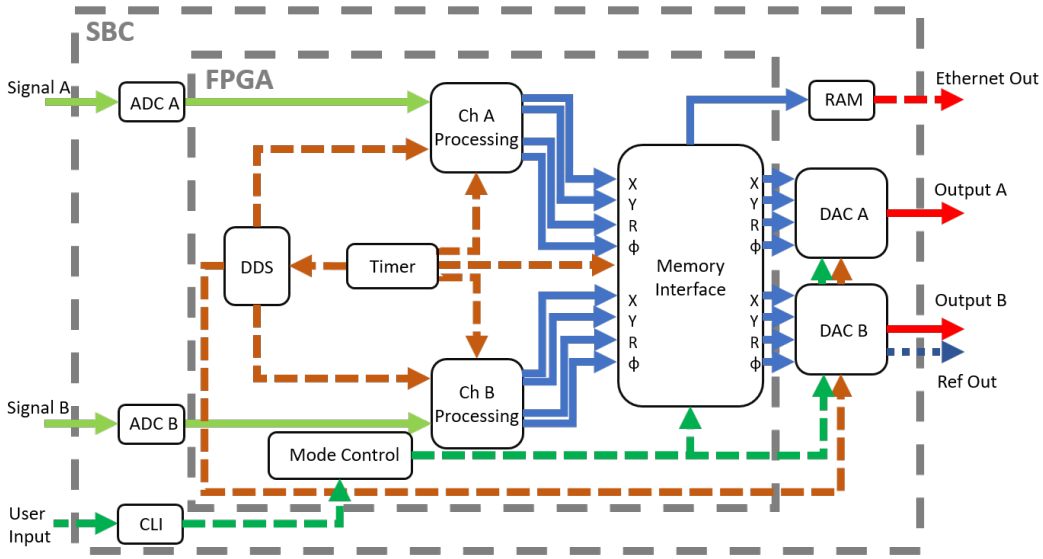

Figure 2.4: Simplified schematic of circuitry layout on Red Pitaya lock-in amplifier FPGA. Signals (solid green arrows) are received at channel processing, where they are multiplied by a reference signal generated in the direct digital synthesis (DDS) block, which takes time data (dashed brown arrows) from the timer and distributes it as a reference. After the multiplication, data are passed through a single pole infinite impulse response (IIR) filter, currently limited to a single pass. Filtered data (solid blue arrows) are then passed to the memory allocation block and subsequently to the digital to analogue converters (DACs), converted to analogue data (solid red arrows) and passed out to the user or saved to the random access memory (RAM) where they can be accessed via ethernet (dashed red arrow). The reference signal is extracted from the DACs in analogue form (dashed blue arrow). Operating parameters and modes are set by the user (dashed green arrows), via the command line interface (CLI) which communicates with the mode control block on the FPGA.

their own data transfer methods, which may be shown to alleviate some or all of these limitations.

Whilst the FPGA is responsible for signal processing and data transfer, parameter setting takes place on the STEMlab's Linux SBC. This device is packaged along with the FPGA on the STEMlab board, allowing the user to operate the Red Pitaya LIA (RePLIA) or any other custom FPGA application entirely using the STEMlab itself. Parameter setting and system control are performed using C and Python codes written specifically for use with the LIA. These codes may be accessed via SSH or a terminal emulator, but in practice are accessed via a Java-based graphical user interface (GUI) on a client computer which allows the user to largely ignore the STEMlab's Linux element. This open-source GUI, written by myself, allows for the setting of all available RePLIA parameters.

2.4.4 Characterisation methodology

Data were extracted from both the RePLIA and Zurich Instruments HF2LI via Ethernet connection. In the case of the RePLIA aboard the STEMlab, this avoided noise from its DACs which were found to increase noise by up to three orders of magnitude compared to identical conditions when extracting data via the network.

Noise for both LIAs during operation was measured at various demodulation frequencies with no input signal present and with a constant amplitude signal produced with an Agilent N5172B EXG vector signal generator. Similarly, noise was measured whilst varying the time constant of the LIAs, with the demodulation frequency fixed at the value determined to be the least noisy by the previous method. As with input noise, these data are presented after a fast Fourier transform (FFT) into the frequency domain.

Passbands for each LIA at various demodulation frequencies were obtained by applying a constant amplitude signal at the specified demodulation frequency. This signal was then combined with a frequency sweep through the demodulation frequency, with a 10 s sweep time. The signal and sweep were combined using a custom-built signal mixer designed by Ben Green and constructed by myself. The extremes of the sweep were chosen such that the sweep width was large compared to the output bandwidth for a practically useful time constant, ensuring a flattened baseline surrounding output peaks.

Zurich Instruments HF2LI

The HF2LI provides a built in input noise measurement protocol. The experimental conditions detailed in the HF2LI user notes were replicated[22] and the input noise measured. Noise was collected whilst inputs were terminated for periods of 1, 10 and 100 seconds. This noise was then subjected to an FFT and the noise level assessed and compared with the manufacturer's stated input noise level of $5\,\mathrm{nV}/\sqrt{\mathrm{Hz}}$ at 1 MHz demodulation for output frequencies greater than 10 kHz.[42]

Red Pitaya Lock-In Amplifier (RePLIA)

Optimal operational parameters (see fig. 3.2) for all lock-in experiments were deduced by examining the output of the RePLIA at varying demodulation frequencies and time constants. The optima chosen were those which resulted in the lowest output noise level. This behaviour was examined both with an applied signal and with terminated inputs. The RePLIA maintains capability over a wide range of demodulation frequencies ($10\,\mathrm{kHz} - 50\,\mathrm{MHz}$) which were also characterised, but figures are quoted using 500 kHz demodulation unless otherwise stated.

Results from the characterisation, all performed by myself, follow in the next chapter.

2.4.5 Magnetocardiography

One potential use for LIAs is in the detection of magnetocardiography (MCG) signals. The signal used in MCG is produced by the same processes which give rise to the signal in electrocardiography (ECG), namely small ion currents generated by the depolarisation and subsequent repolarisation of muscular tissue comprising the beating of the heart.[43] For the purposes of the physics involved however, these signals can be treated merely as signals generated by currents in a 'wire'.

The Biot-Savart law:[44]

$$\bar{B}(\bar{r}) = \frac{\mu_0}{4\pi} \int \frac{\nabla' \times \bar{j}(\bar{r}')}{|\bar{r} - \bar{r}'|} d^3 r' \tag{2.6}$$

simplified to:

$$B_r = \frac{\mu_0 I}{2\pi r} \tag{2.7}$$

where B_r is the magnetic field at a given distance r from an infinitely long wire, $\mu_0 = 1.256\,637\,062\,12 \times 10^6\,\mathrm{Hm}^{-1}$, demonstrates a simple relationship between a flowing current I and the strength of the resulting magnetic field. In the case of a human heart, assuming that the signal originates within a few centimetres of the detector, B_r has a strength of a few tens of pT.[45] MCG as a use for LIAs is discussed in chapter 6.

Chapter 2 References

[1] L. C. Caplan and R. Stern. An Inexpensive Lock-In Amplifier. *Rev. Sci. Instrum.*, 42:689–695, 1971.

[2] W. C. Michels and N. L. Curtis. A pentode lockin amplifier of high frequency selectivity. *Rev. Sci. Instrum.*, 12(9):444, 1941.

[3] X. Wang. Sensitive digital lock-in amplifier using a personal computer. *Rev. Sci. Instrum.*, 61(7):1999–2000, 1988.

[4] P.-A. Probst and A. Jaquier. Multiple-channel digital lock-in amplifier with ppm resolution. *Rev. Sci. Instrum.*, 65(3):747, 1998.

[5] M. Hofmann, R. Bierl, and T. Rück. Implementation of a dual-phase lock-in amplifier on a TMS320C5515 digital signal processor. *2012 5th European DSP Education and Research Conference (EDERC)*, pages 20–24, 2012.

[6] M. O. Sonnaillon and F. J. Bonetto. A low-cost, high-performance, digital signal processor-based lock-in amplifier capable of measuring multiple frequency sweeps simultaneously. *Rev. Sci. Instrum.*, 76(024703):1–7, 2005.

[7] G. Macias-Bobadilla, J. Rodríguez-Reséndiz, G. Mota-Valtierra, G. Soto-Zarazúa, M. Méndez-Loyola, and M. Garduno-Aparicio. Dual-Phase Lock-In Amplifier Based on FPGA for Low-Frequencies Experiments. *Sensors*, 16:379, 2016.

[8] G. C. Giaconia, G. Greco, L. Mistretta, and R. Rizzo. Exploring FPGA-based Lock-In Techniques for Brain Monitoring Applications. *Electronics*, 6(1):18, 2017.

[9] S. G. Castillo and K. B. Ozanyan. Field-programmable data acquisition and processing channel for optical tomography systems. *Rev. Sci. Instrum.*, 76:095109, 2005.

[10] M. Carminati, G. Gervasoni, M. Sampietro, and G. Ferrari. Note: Differential configurations for the mitigation of slow fluctuations limiting the resolution of digital lock-in amplifiers. *Rev. Sci. Instrum.*, 87(2):026102, 2016.

[11] M. Meade. *Lock-in amplifiers: Principles and Applications.* Peter Peregrinus Ltd., 1983.

[12] F. Humayun, R. Khan, S. Saadman, and R. Haque. Design of a Cost-Effective Analog Lock-In Amplifier Using Phase Sensitive Detector. In *2018 International Applied Computational Electromagnetics Society Symposium (ACES)*, 2018.

[13] J. H. Scofield. Frequency-domain description of a lock-in amplifier. *American Journal of Physics*, 62(2):129–133, 1994.

[14] P. Horowitz and W. Hill. *The Art of Electronics, 2nd Edition.* Cambridge University Press, 1989.

[15] R. W. M. Smith, I. L. Freeston, B. H. Brown, and A. M. Sinton. Design of a phase-sensitive detector to maximize signal-to-noise ratio in the presence of gaussian wideband noise. *Measurement Science and Technology*, 3(11):1054, 1992.

[16] E. Theocharous. Absolute linearity characterization of lock-in amplifiers. *Appl. Opt.*, 47(8):1090–1096, Mar 2008.

[17] S. DeVore, A. Gauthier, J. Levy, and C. Singh. Development and evaluation of a tutorial to improve students' understanding of a lock-in amplifier. *Physical Review Physics Education Research*, 12(2):020127, 2016.

[18] Stanford Research Systems. *Stanford Research Systems: About Lock-in Ampli-*

fiers. https://www.thinksrs.com/downloads/pdfs/applicationnotes/AboutLIAs.pdf.

[19] Zurich Instruments AG. White paper: Principles of lock-in detection and the state of the art. https://www.zhinst.com/sites/default/files/li_primer/zi_whitepaper_principles_of_lock-in_detection.pdf. Accessed: September 28, 2021.

[20] Red Pitaya STEMlab board. https://www.redpitaya.com/f130/STEMlab-board, 2018. Accessed: 2018-09-05.

[21] A. Restelli, R. Abbiati, and A. Geraci. Digital field programmable gate array-based lock-in amplifier for high-performance photon counting applications. *Review of Scientific Instruments*, 76(9):093112, 2005.

[22] Zurich Instruments. HF2 User Manual - LabOne Edition. https://www.zhinst.com/manuals/hf2, 2018.

[23] R. Li and H. Dong. Design of digital lock-in amplifier based on dsp builder. In *2018 IEEE 4th Information Technology and Mechatronics Engineering Conference (ITOEC)*, pages 222–227, Dec 2018.

[24] G. Gervasoni, M. Carminati, G. Ferrari, M. Sampietro, E. Albisetti, D. Petti, P. Sharma, and R. Bertacco. A 12-channel dual-lock-in platform for magneto-resistive dna detection with ppm resolution. In *2014 IEEE Biomedical Circuits and Systems Conference (BioCAS) Proceedings*, pages 316–319, Oct 2014.

[25] G. Gervasoni, M. Carminati, and G. Ferrari. A general purpose lock-in amplifier enabling sub-ppm resolution. *Procedia Engineering*, 168:1651–1654, 2016.

[26] L. H. Arnaldi. Implementation of an axi-compliant lock-in amplifier on the redpitaya open source instrument. In *2017 Eight Argentine Symposium and Conference on Embedded Systems (CASE)*, pages 1–6, Aug 2017.

[27] D. Divakar, K. Mahesh, M. M. Varma, and P. Sen. FPGA-based lock-in amplifier for measuring the electrical properties of individual cells. In *2018 IEEE 13th Annual International Conference on Nano/Micro Engineered and Molecular Systems (NEMS)*, pages 1–5, April 2018.

[28] A. Chighine, E. Fisher, D. Wilson, M. Lengden, W. Johnstone, and H. McCann. An FPGA-based lock-in detection system to enable chemical species tomography using TDLAS. In *2015 IEEE International Conference on Imaging Systems and Techniques (IST)*, pages 1–5, Sep. 2015.

[29] Y. Sukekawa, T. Mujiono, and T. Nakamoto. Two-dimensional digital lock-in circuit for fluorescent imaging of odor biosensor system. In *2017 New Generation of CAS (NGCAS)*, pages 241–244, Sep. 2017.

[30] PyRPL GUI Manual. https://pyrpl.readthedocs.io/en/latest/gui.html. Accessed: September 28, 2021.

[31] Adding voltage regulators for the RedPitaya output stage. https://ln1985blog.wordpress.com/2016/02/07/adding-voltage-regulators-for-the-redpitaya-output-stage/. Accessed: September 28, 2021.

[32] Red Pitaya DAC performance. https://ln1985blog.wordpress.com/2016/02/07/red-pitaya-dac-performance/. Accessed: September 28, 2021.

[33] Lock-in amplifier for myrio. https://delacor.com/products/lock-in-amplifier/. Accessed: September 28, 2021.

[34] J. Vandenbussche, P. Lee, and J. Peuteman. On the Accuracy of Digital Phase Sensitive Detectors Implemented in FPGA Technology. *IEEE Transactions on Instrumentation and Measurement*, 63(8):1926–1936, Aug 2014.

[35] S. Hauck. The roles of FPGAs in reprogrammable systems. *Proceedings of the IEEE*, 86(4):615–638, April 1998.

[36] E. Monmasson, L. Idkhajine, M. N. Cirstea, I. Bahri, A. Tisan, and M. W. Naouar. Fpgas in industrial control applications. *IEEE Transactions on Industrial Informatics*, 7(2):224–243, 2011.

[37] I. Kuon and J. Rose. Measuring the Gap Between FPGAs and ASICs. *IEEE Transactions on Computer-Aided Design of Integrated Circuits and Systems*, 26(2):203–215, Feb 2007.

[38] E. Monmasson and M. N. Cirstea. Fpga design methodology for industrial control systemsa review. *IEEE Transactions on Industrial Electronics*, 54(4):1824–1842, Aug 2007.

[39] M. Khaled. *Enhancing the Performance of Digital Controllers using Distributed Multicore/Heterogeneous Embedded Systems*. PhD thesis, Minia University, 01 2014.

[40] Y. P. Siwakoti and G. E. Town. Design of FPGA-Controlled Power Electronics and Drives Using MATLAB Simulink. In *2013 IEEE ECCE Asia Downunder (ECCE Asia)*, pages 571–577, 2013.

[41] P. Jamieson, K. B. Kent, F. Gharibian, and L. Shannon. Odin II - An Open-source Verilog HDL Synthesis Tool for CAD Research. In Sass, R and Tessier, R, editor, *2010 18th IEEE Annual International Symposium On Field-Programmable Custom Computing Machines (FCCM 2010)*, Annual IEEE Symposium on Field-Programmable Custom Computing Machines, pages 149–156, 2010.

[42] ZI HF2LI Leaflet. https://www.zhinst.com/sites/default/files/zi_hf2li_leaflet_web_0.pdf, 2018. Accessed: 2018-10-02.

[43] D. Cohen. Magnetic fields around the torso: production by electrical activity of the human heart. . *Science*, 156:652–654, 1967.

[44] P. J. Karp, T. E. Katila, M. Saarinen, P. Siltanen, and T. T. Varpulax. The normal human magnetocardiogram. II. A multipole analysis. *Circulation Research*, 47(1):117–30, 1980.

[45] K. Jensen, M. A. Skarsfeldt, H. Strkind, J. Arnbak, M. V. Balabas, S.-P. Olesen, B. Hjorth-Bentzen, and E. S. Polzik. Magnetocardiography on an isolated animal heart with a room-temperature optically pumped magnetometer. *Scientific Reports*, 8:16218, 2018.

Chapter 3

LIA Results

3.1 Results

Chapter 2 discussed the principles and operation of lock-in amplifiers, and the realisation of an LIA based on a single board computer with an integrated FPGA was described. In the following chapter, the characterisation of this LIA is detailed and the performance compared to that of a commercially available alternative.

Figures 3.1a) and 3.1b) compare the input noise from the RePLIA device and a Zurich Instruments HF2LI, a commercially available, high frequency LIA, where 'input noise' is defined as the inherent noise measured at a terminated input. Noise data was collected for 1 second, 10 seconds and 100 seconds and then fast Fourier transforms (FFTs) calculated for each data set. The noise level is then produced by averaging the output of the FFT. The results of this for the RePLIA can be seen in table 3.1, whilst the results for the HF2LI conform with the specifications set down by the manufacturer, quoted as achieving sensitivities of 5 nV·Hz$^{-\frac{1}{2}}$. It should be noted that in the published article,[1] these data were presented as noise spectral density $\rho_n = V_{FFT}/\nu_{FFT}$ where ν_{FFT} is the FFT output frequency and V_{FFT} the corresponding voltage. However, the correct definition of noise spectral density is $V_{FFT}/1Hz$. In this thesis, the noise spectrum is presented for clarity. Figure 3.1c shows the predicted noise level of both devices, calculated using both the 1 s noise level and the 100 s level as initial values. Both the RePLIA and HF2LI remain within this predicted range.

Collection time (s)	Level (nV)	Sensitivity (nV· Hz$^{-\frac{1}{2}}$)
1	89	89
10	21	66
100	6	60

Table 3.1: RePLIA input noise level and corresponding sensitivity as measured after three different collection periods.

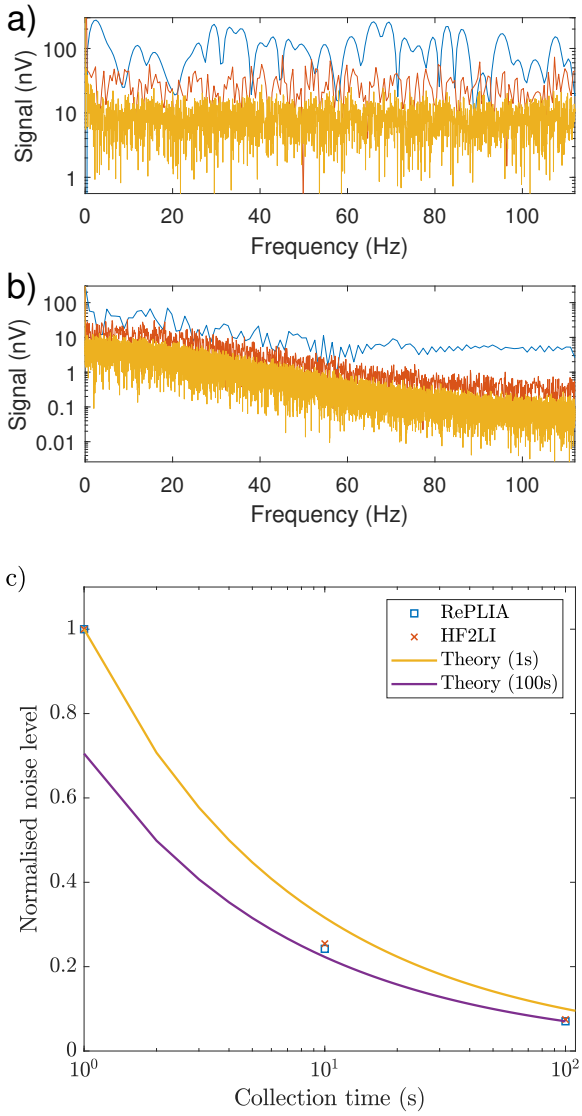

Figure 3.1: Noise spectrum from a) RePLIA at 500 kHz demodulation with a 1 ms time constant (with 1 s data zero padded) and b) HF2LI at 1 MHz demodulation and 700 µs time constant, at 1 second (blue trace), 10 seconds (red trace) and 100 seconds (orange trace) collection time (output data is R for both devices). c) noise level decays with increased collection time, close to the predicted $1/\sqrt{time}$ relationship (top trace) calculated based on noise measured after 1 second of collection. The lower trace indicates theoretical values back calculated from the 100 seconds data point.

Hardware constraints are expected to limit the sensitivity of the RePLIA under various operating conditions. Figure 3.2 shows the FFT output of the device operating under a range of demodulation frequencies. Time constants were optimised for each demodulation frequency to limit the effect of the time constant on the output. From this it is evident that the lowest input noise is recorded at a demodulation frequency of 500 kHz (with a corresponding time constant of 1 ms). At demodulation frequencies below 100 kHz it can be seen that significant noise is recorded at regular output frequency intervals. This is expected to arise from electrical interference, although specific noise sources were not identified. For demodulation frequencies greater than the optimum, noise level does marginally increase but is broadband and does not produce the frequency specific peaks as seen with lower demodulation frequencies.

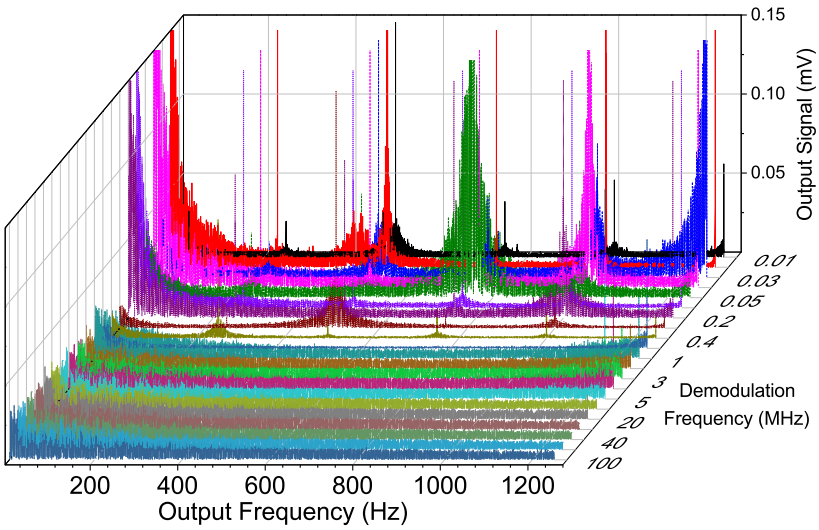

Figure 3.2: FFTs of terminated input data, extracted via file transfer, at various RePLIA demodulation frequencies with 100 s collection time. Two distinct noise regimes seem to exist, with demodulation frequencies above 100 kHz producing significantly lower noise. Time constants were varied dependent on demodulation frequency (see table 3.2). Note that low frequency and high intensity data have been cropped for visual clarity.

The linewidth of an LIA's 'passband' is an important characteristic as it quantifies the output at unwanted frequencies either side of the demodulation frequency. In figures 3.3a and 3.3b this passband is plotted for a range of demodulation frequencies. The magnitude of the output peak for both LIAs is plotted in figure 3.3c. From this it is observed that though the RePLIA output contains a greater contribution from unwanted frequencies, the output is more consistent as the demodulation frequency approaches the maximum specified value. For the HF2LI, at frequencies above the 50 MHz demodulation frequency specified by the manufacturer, the output drops below the 'half power point', i.e. $0.77\times$ the maximum output. This occurs at roughly the same demodulation frequency for the RePLIA, hence the maximum demodulation frequency for our device is also quoted as 50 MHz.

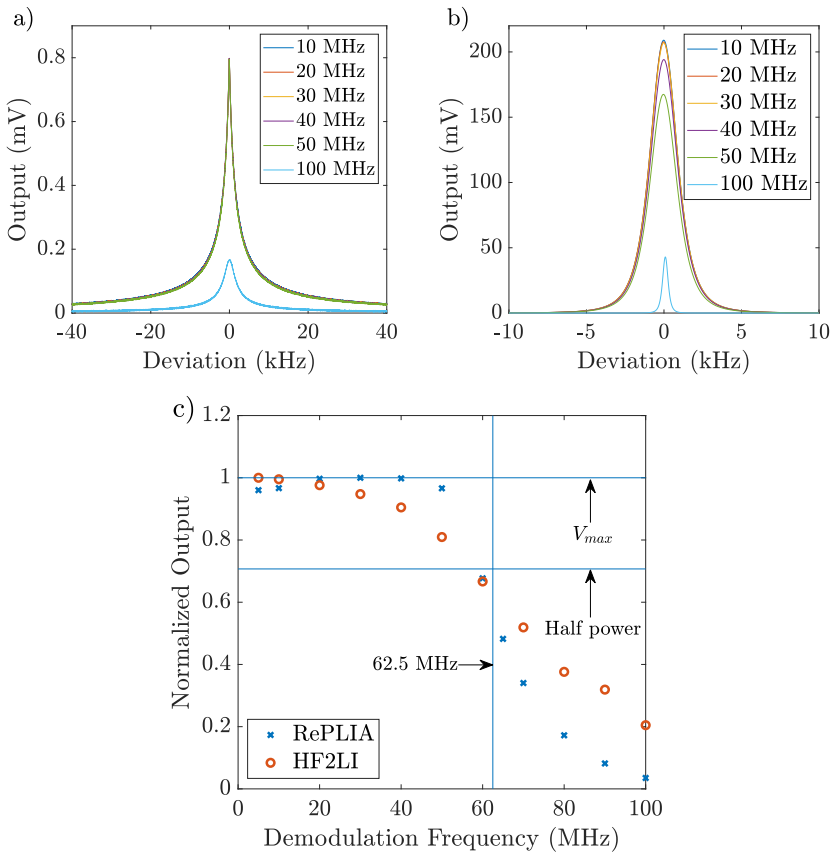

Figure 3.3: Output of frequency sweep for MHz demodulation frequencies for the a) RePLIA and b) HF2LI. c) Maximum output voltage of the RePLIA plotted against demodulation frequency, showing the half power point. Note that the RePLIA has a sampling rate of 125 MHz.

The linearity of the RePLIA's output was measured by adjusting the input voltage of a constant sine wave at the device's demodulation frequency and measuring the magnitude of the output signal. This produced a linear output region between $-0.7\,\mathrm{V}$ and $0.7\,\mathrm{V}$ (see figure 3.4). Therefore output magnitudes resulting from input voltages within this range can be considered consistent, whereas input voltages lying outside this range cannot be relied upon. This does not necessarily limit the device's usefulness as input signals can be scaled to be accommodated by this input range.

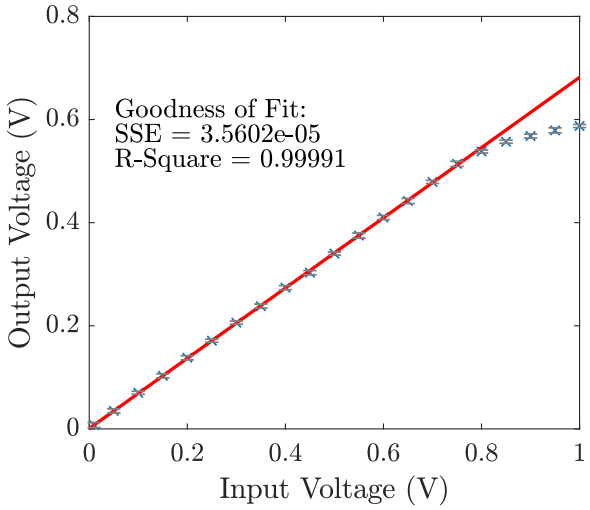

Figure 3.4: Demodulated RePLIA output against input voltage, operating at 500 kHz demodulation for a ±1 V input range. Solid red line is a linear fit of the 0 to 0.7 V linear region.

Data can be extracted from the LIA in one of two ways. Firstly, the STEMlab 125-14 is supplied with two 14-bit digital-analogue converters (DACs). Secondly, the RePLIA is written to allow for data extraction via the STEMlab's Ethernet socket. Data for figures 3.1 and 3.2 were extracted by the latter method. Figure 3.5a shows the noise spectral density when input noise data is measured using the DACs to obtain data. The input noise is much greater than data obtained via the Ethernet connection(140 $\mu V/\sqrt{Hz}$ for 1 s collection time).

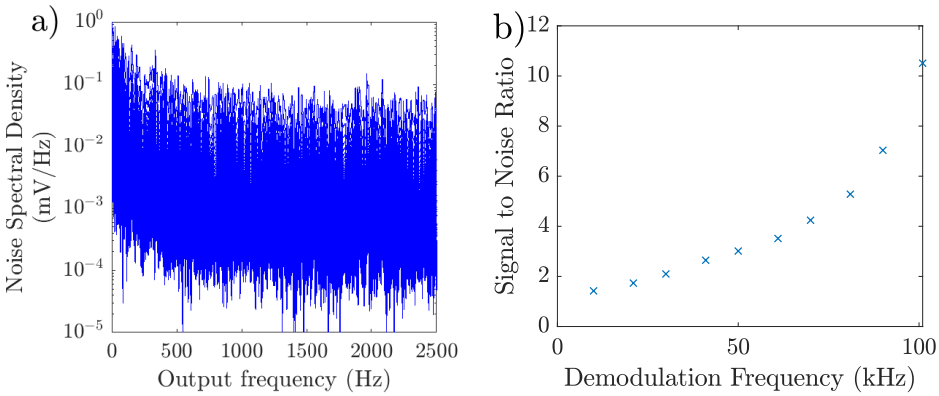

Figure 3.5: a) FFT of 10 kHz demodulation data taken from the RePLIA's DAC outputs, demonstrating significantly greater noise $140\,\mu\mathrm{V}/\sqrt{\mathrm{Hz}}$ than data taken from Ethernet output. b) Output signal to noise from the DAC outputs improves dramatically with demodulation frequency throughout lower frequency ranges due to increased signal.

The signal to noise ratio (SNR) of data obtained via the DACs is heavily compromised at lower demodulation frequencies (figure 3.5b).

Further data taken from the DAC outputs shows that the DAC multiplier - an amplification factor - does not have a major effect on the noise level (figures 3.6a-c).

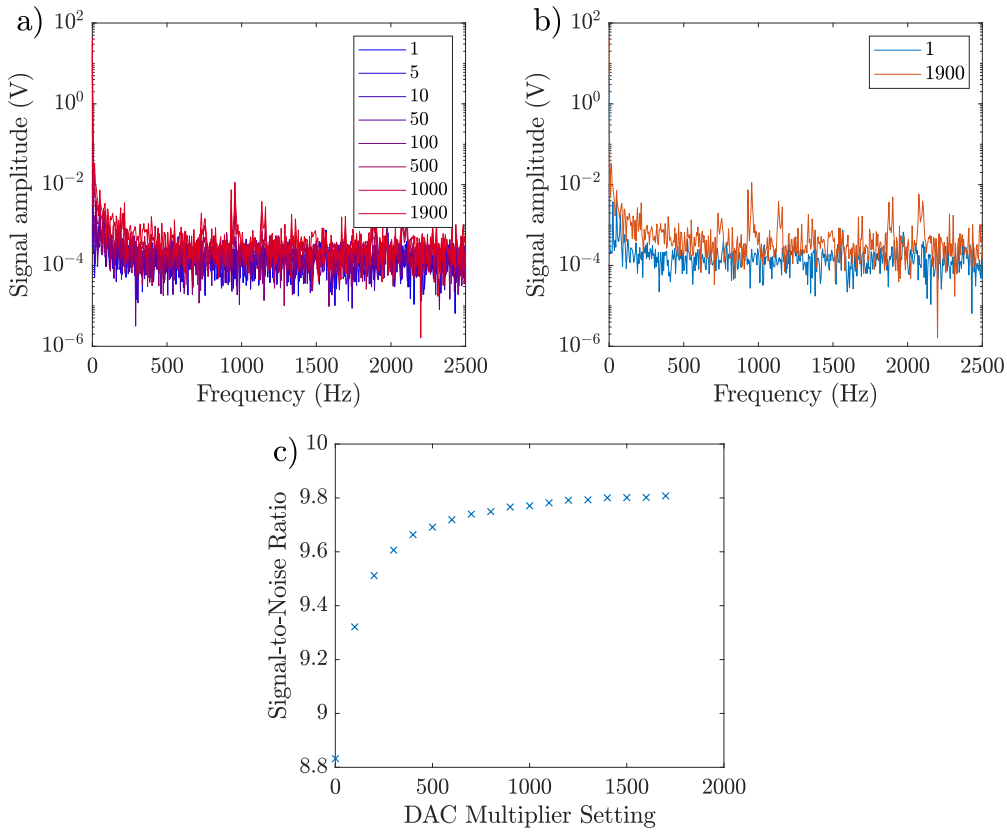

Figure 3.6: Fast Fourier transforms of RePLIA input noise at varying DAC multiplier settings (a) with extremes only plotted for clarity (b). c) The signal to noise ratio at the RePLIA's digital-to-analogue outputs increases with larger DAC multiplier. However, even small signals can lead to saturation of these outputs. Data obtained at 500 kHz demodulation frequency and a 10 ms time constant.

The time constant set by the user can have a significant effect on both the sensitivity of the LIA and the quality of the output data (figure 3.7). Though longer time constants produce narrower passbands, they also produce passband fringes which lead to inconsistent contributions from frequencies either side of the demodulation frequency. Overly short time constants meanwhile produce broader passbands and therefore greater (though consistent) contributions from undesirable frequencies. Further to this, it is important to select a time constant (also known as the averaging period) which contains enough data points such that the resulting output is a

reliable average. As such, time constants were chosen which were at least ten times the period of the demodulation frequency (see table 3.2).

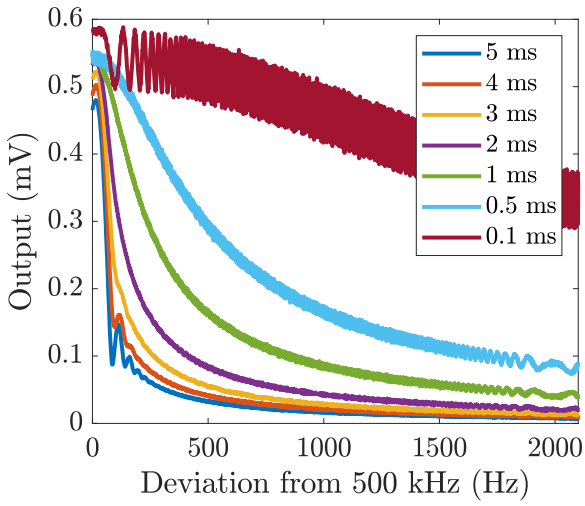

Figure 3.7: The effect of the time constant setting on the resulting passband. An 80 kHz sweep over 10 seconds through the demodulation frequency of 500 kHz at varying time constants results in distortion of the passband. Longer time constants result in fringes in the unwanted frequency regions and shorter time constants result in excessive acceptance of unwanted frequencies. For 500 kHz, a time constant of 1 ms was chosen as a suitable compromise. The small section of the sweep output shown above shows only the part of the passband affected by the time constant.

Time Constants (τ)		
F_{mod}(MHz)	τ_{min}(ms)	τ(ms)
0.001	10	100
0.01	1	100
0.1	0.1	10
0.5	$2 \cdot 10^{-2}$	1
1	$1 \cdot 10^{-2}$	1
10	$1 \cdot 10^{-3}$	1
100	$1 \cdot 10^{-4}$	0.1

Table 3.2: Time constants τ for the RePLIA at various demodulation frequencies. The central column contains the minimum usable time constant and the right hand column details the actual time constants used which were determined by ensuring a near-Lorentzian passband at the relevant demodulation frequency. Note that this table is not exhaustive and longer/shorter time constants and lower/higher demodulation frequencies may be used.

FFTs of DAC data for low ($1-10\,\mathrm{kHz}$) demodulation frequencies can be seen in figure 3.8. A large number of peaks at various output frequencies are present and are so throughout this low demodulation frequency range.

Noise as a function of time constant can be seen in figure 3.9. Though a longer time constant results in a lower noise figure, care must be taken in choosing an appropriate averaging period as discussed in figure 3.7.

Output passbands were expected to be Lorentzian in shape. Some deviation from this shape is visible in data from both the RePLIA and the HF2LI (see figure 3.10) and this deviation is more pronounced for the RePLIA. However, this does not necessarily detract from the usefulness of the device, provided that a user is aware of this characteristic. The $1/f$ nature of the input noise can be seen in figure 3.11 and is consistent with the flicker noise of the input stage.

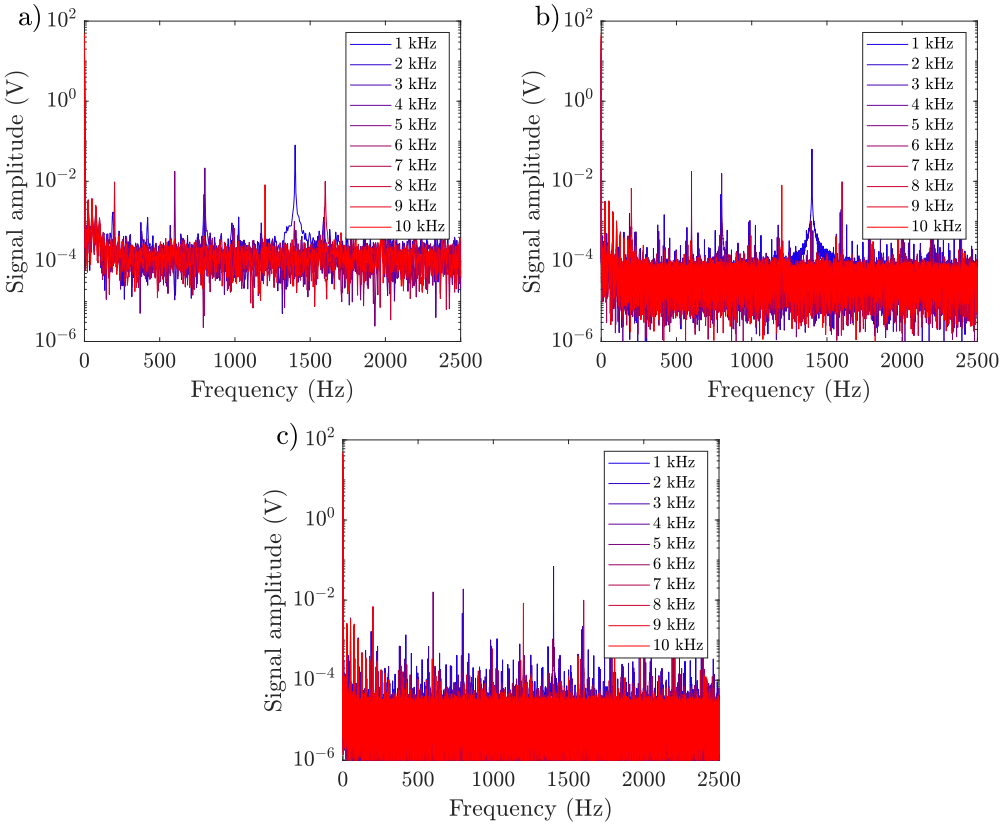

Figure 3.8: Low Frequency (1-10 kHz) FFTs of RePLIA input noise from a) 1 second, b) 10 seconds and c) 100 seconds of DAC data. Frequency-specific spikes are common at low demodulation frequency.

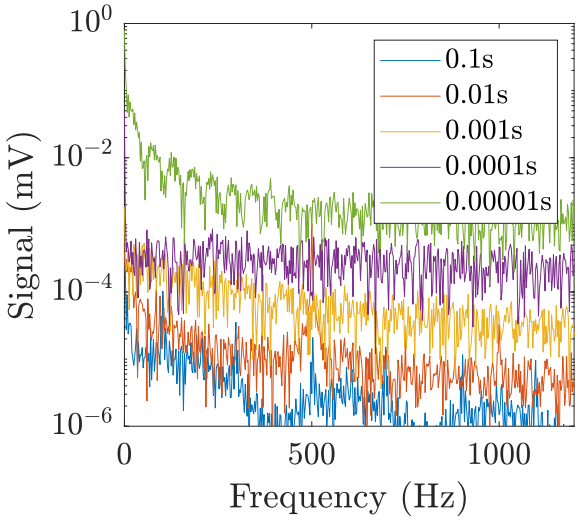

Figure 3.9: FFTs of noise at varying time constant at a demodulation frequency of 500 kHz.

3.2 Discussion

The input noise of the RePLIA is significantly higher than that of the HF2LI but is still low enough such that the RePLIA remains useful for many applications, particularly where high lock-in frequencies are required or where large numbers of input channels are needed and cost is a limiting factor. The high demodulation frequency capability of the device allows it to be competitive where other more expensive commercial devices are not.

Whilst commercial devices remain superior for high precision measurements, the open source nature and low cost of the RePLIA make it a practical option when cost and/or flexibility are a factor.

3.2.1 Cross-talk

During several experiments it was observed that cross-talk was sometimes present where an applied signal at one ADC input resulted in a non-zero signal detected at the second ADC input. Figure 3.12 shows the results of an experiment intended to

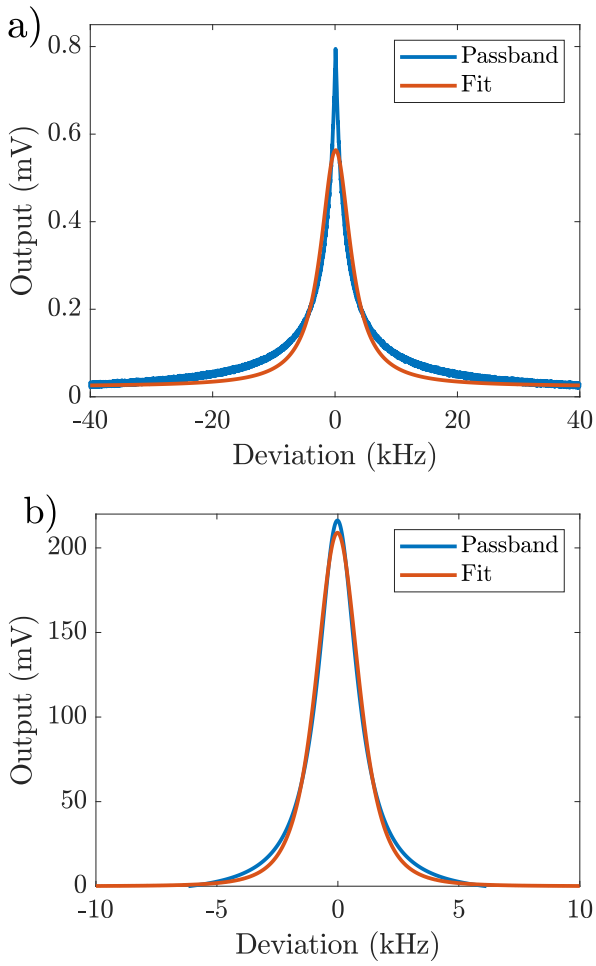

Figure 3.10: a) RePLIA and b) HF2LI 10 MHz passbands with Lorentzian fits with 2.6 kHz and 2 kHz linewidths respectively. Note that the x-axes cover different ranges for these data.

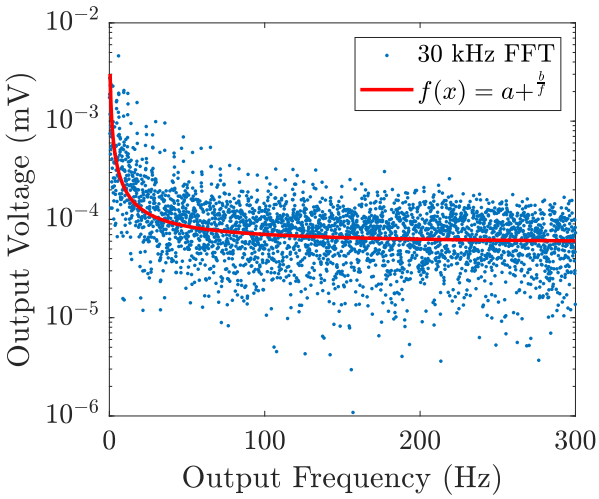

Figure 3.11: FFT of signal demodulated at 30 kHz, with a fit of $f(x) = a + b \cdot 1/f$ where $a = 5.6 \cdot 10^{-5}, b = 0.001$, consistent with flicker noise of the board.

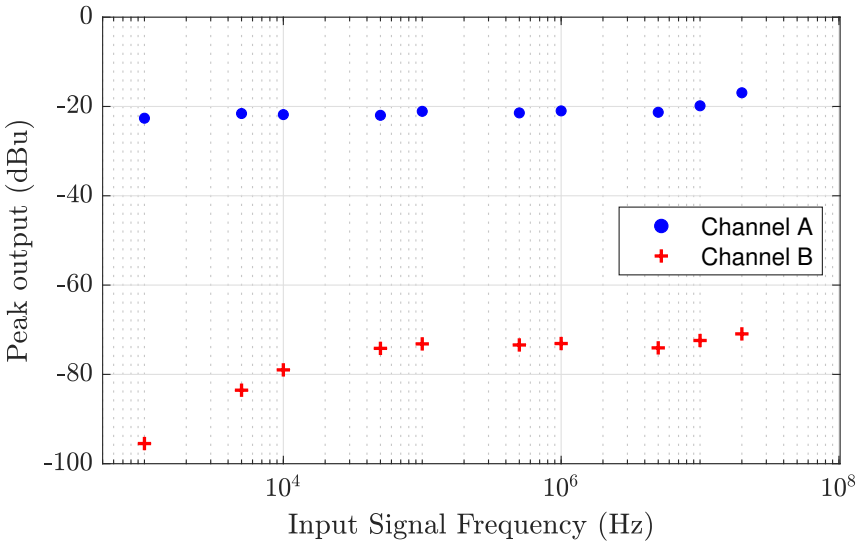

Figure 3.12: Cross-talk between the two fast input channels was detected using the STEMLab hardware and software. A sine wave input signal was applied at channel A with a significant signal detected at channel B. Note that cross-talk is minimal at lower frequency and was indistinguishable from background noise at input frequencies below 1 kHz.

quantify this cross-talk. A sinusoidal 1 V signal delivered by a shielded cable was applied to one ADC input whilst the second input was terminated. A fast Fourier transform (FFT) of the resultant output for each input channel was calculated by the STEMLab's Spectrum Analyser application. The peak FFT output at the frequency of the input signal was measured. This was repeated for a range of input frequencies. This demonstrates that the magnitude of the cross-talk is not trivial at higher input frequency, although at input frequencies below 1 kHz the signal in the second channel was indistinguishable from background noise. It should be noted that this experiment was performed using the STEMLab's own software, rather than the RePLIA software, in order to ensure that the observed cross-talk was not a product of the LIA, but rather a fundamental limitation of the hardware itself. The origin of this cross-talk remains unclear, but may be a result of insufficient shielding of the circuitry around the STEMLab's inputs.

Chapter 3 References

[1] R. L. Patel B. L. Green G. A. Stimpson, M. S. Skilbeck and G. W. Morley. An open-source high-frequency lock-in amplifier. *Review of Scientific Instruments*, 90:094701, 2019.

Chapter 4

Nanodiamonds

4.1 Introduction

Diamond is solid allotrope of carbon, typically metastable except in high pressure, high temperature regimes.[1, 2, 3] The carbon atoms are arranged tetrahedrally, such that each atom has four equidistant nearest neighbours.[4] Although diamond itself comprises only carbon, the lattice may contain defects.[5, 6] Many of these come in the form of substitutional impurities, where a carbon atom in the lattice is replaced by an atom of another element, such as nitrogen, boron, silicon or oxygen.[7] Another known defect is the lattice vacancy defect, an unoccupied lattice point.[8] When a lattice vacancy has a substitutional nitrogen atom as a nearest neighbour, the result is known as a nitrogen-vacancy (NV) defect.[9]

4.2 Diamond as a material

4.2.1 Crystallographic structure

Diamond is comprised of two intersecting face centred cubic (fcc) structures with short, rigid bonds. This rigid lattice lends to the material a number of superlative physical properties.

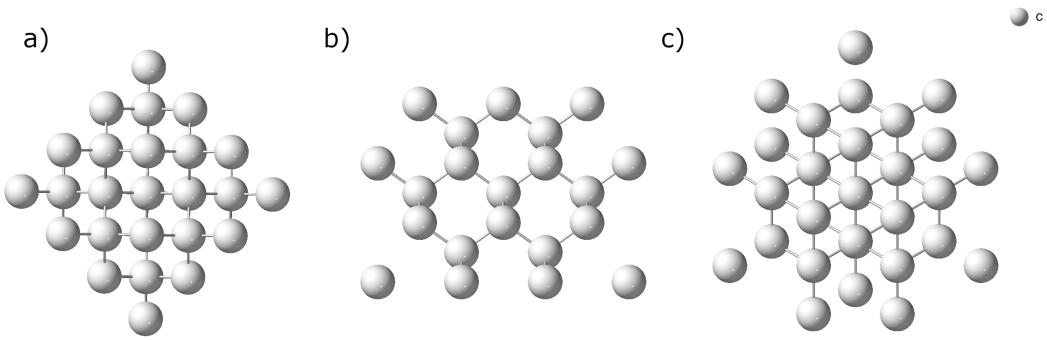

Figure 4.1: The diamond crystal lattice along the three principle axes; a) [100], b) [110] and c) [111].

4.2.2 Intrinsic material properties

As a bulk material, diamond owes many of its attributes to its chemical bonding and electronic properties, in particular its hardness (Vickers hardness of 115 GPa vs. 76 GPa for cubic-BC_2N[10]), thermal conductivity ($\approx$2000 W/m $\cdot$ K compared to 385 W/m $\cdot$ K for copper at room temperature[11]) and appearance.

The transparency of diamond can be attributed to its wide band gap (E_{gap} = 5.47 eV). The rigid, purely covalent bonds found in diamond interact only weakly with passing photons, resulting in a broad optical transmission range beginning at around 225 nm and extending far into the infrared, with the exception of lattice absorption between 2.6 µm and 6.2 µm.[12] Contributing to its propensity for effective phonon transport,[13] these short, strong bonds and diamond's high Debye temperature lead to itss superlative thermal conductivity at room temperature. These material properties are of high importance in many avenues of modern technological development. In particular, materials with high thermal conductivity are in demand for their usefulness in facilitating the removal of heat from central processing units (CPUs) and other microelectronic components in high performance computing[14] and for thermal management in solid state lasers.[15] The transparency of diamond, particularly in the infrared range,[16] combined with its thermal conductivity and hardness, make diamond a highly appropriate choice as a material for inspection windows in research and manufacturing.[17, 16]

4.2.3 Bonding

Carbon in atomic form has an electronic configuration of $1s^2 2s^2 2p^2$. In the diamond structure, it forms covalent bonds with four neighbours to form the diamond lattice. These sp^3 hybridised bonds are of length 1.541 Å (154.1 pm) in pure un-strained material.

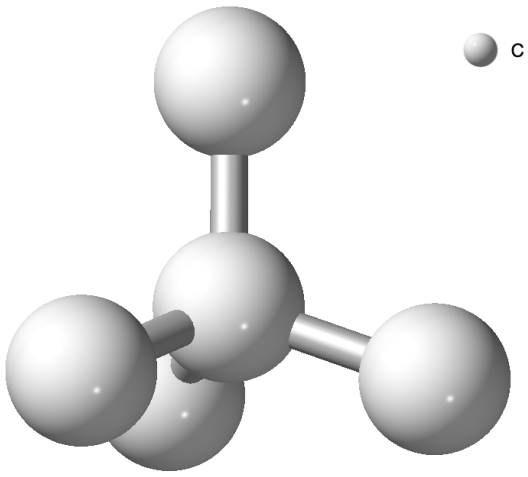

Figure 4.2: Each carbon atom in the diamond lattice is covalently bonded to four identical carbon atoms.

4.2.4 The tight binding model

Electrons are bound to the nucleus of an atom by the Coulomb interaction with a $\frac{1}{r}$ potential, forming a potential well. The resultant electronic wavefunctions have discrete energy levels within this potential well (see fig. 4.4). A carbon atom has four valence electrons; two in the $2s$ shell and two in the $2p$ shell. When a second atom is introduced, it too has discrete energy levels which are identical to those of the original atom. However, once the two atoms and their respective electron shells are brought together, the wave functions of the various shells overlap, forming a set of bonding levels and a set of anti-bonding levels, where the overall number of energy levels is preserved. In diamond, the electrons from the $2p$ shell join those from the $2s$ shell, forming hybrid sp^3 bonds between the two atoms (see fig. 4.3). As the number of atoms is increased further, the energy difference between the bonding and anti-bonding states forms diamond's band gap (see figs. 4.4 & 4.3).

The size of the band gap, as can be seen in fig.4.4 is determined by the atomic separation. At atomic separations where a gap exists between the p and s states, semiconducting (or insulating) behaviour will be observed. At atomic separations

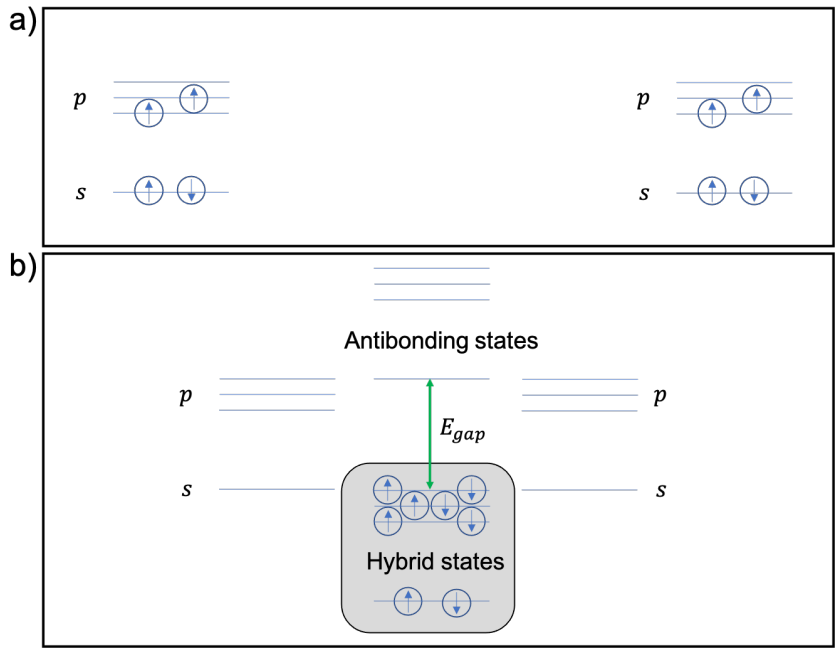

Figure 4.3: a) Two isolated carbon atoms at an infinite distance have four electrons available for bonding (circles with arrows showing spin) i.e. two electrons in each p-orbital and 2 in each s-orbital. The 2 core electrons are not concerned with bonding and are not shown. b) When two such atoms are brought close together, the p- and s-orbitals overlap and the electrons from the p-orbitals join with those from the s-orbitals to form the sp^3 hybrid state with a band gap E_{gap} up to the antibonding states.

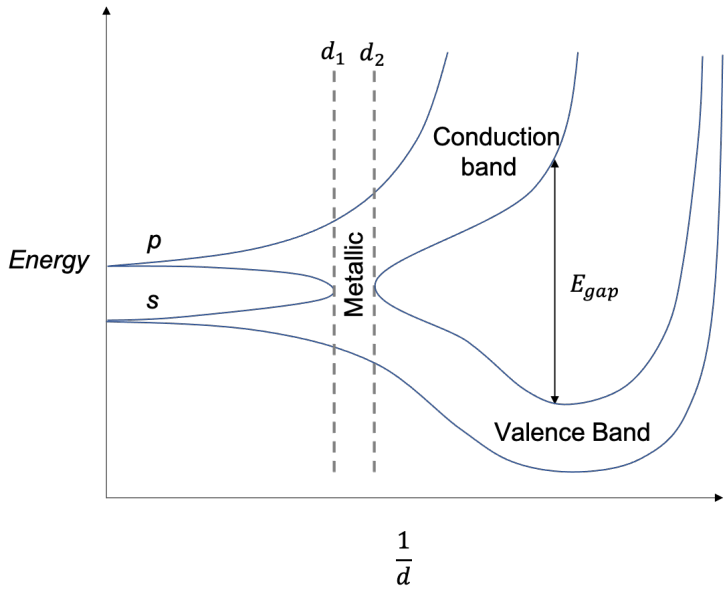

Figure 4.4: A drawing of the band structure of a semiconductor (adapted from[18]). As the energy levels from multiple atoms accumulate they 'smear out', forming bands. The atomic separation d determines the energy gap (band gap) between the conduction and valence bands. For atomic separations between d_1 and d_2, metallic behaviour (i.e. high electrical conductivity) will be extant.

where no such gap exists metallic behaviour including electrical conductivity will be observed.

4.2.5 Electronic properties

Though the transparency, thermal conductivity and hardness described above are indeed directly related to the nature of diamond's bonding, this is realised through the material's electronic band structure.

A semiconductor's band structure is such that the valence band is full (at 0 K) and yet no electrons may be excited to the (empty) conduction band as a gap exists between the two bands.[18] In order for an electron to make the transition between the valence and conduction bands (thereby also creating a 'hole' in the valence band), it must acquire at least as much energy as the difference between the two bands. This can happen in various ways, chiefly through thermal heating

of the material to a finite temperature or by optical absorption. In diamond at room temperature (300 K), this band gap is 5.47 eV meaning that energy of 5.47 eV ($\approx$ 227 nm in terms of optical wavelength) or greater is required to excite an electron to the conduction band. Photons of lower energy (longer wavelength) than this are therefore not absorbed by this mechanism and so are transmitted (other excitation phenomena notwithstanding).

As well as the transparency, this band structure leads to the electronically insulating (and semiconducting) properties of diamond. With an empty conduction band, diamond is unable to conduct electricity unless a sufficient modification is made to the band structure, which can be achieved for example by boron doping. A p-type acceptor dopant, boron can cause conductive behaviour in diamond depending on dopant concentration.[19] Research has also taken place on the role of nitrogen, a deep n-type donor, in semiconductor phenomena in diamond,[20, 21] as well as many other dopants.[22]

Indirect band gap

Figure 4.5[23] shows the electronic band structure of diamond at 300 K. The offset in k-vector between the highest occupied energy level in the valence band and the lowest unoccupied energy level in the conduction band indicates that diamond is an indirect band gap semiconductor, meaning that further to the absorption of a photon close to E_{gap}, an electron will also require an increase in momentum via phononic interactions in order to make the transition to the conduction band. Similarly, in order for an electron to annihilate with a 'hole' in the valence band (created when an electron is excited to the conduction band), a phonon must be absorbed or emitted in order to conserve the crystal momentum.

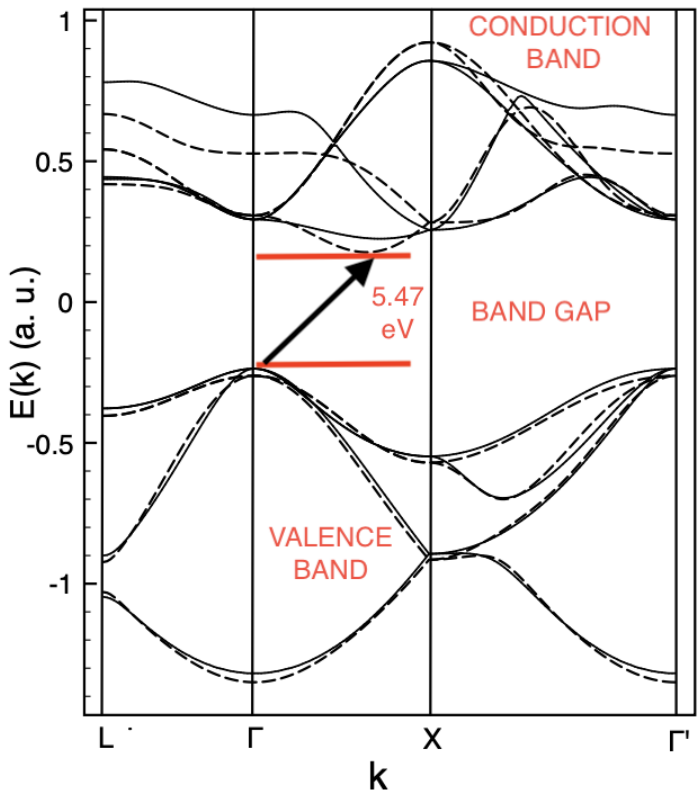

Figure 4.5: A simulation of the band structure of diamond adapted from Smith et al.[23] The vertical axis denotes the energy of an occupied or unoccupied state, whilst the horizontal axis shows the 'crystal momentum' or k-vector in the lattice's Brillouin zone. Occupied energy levels reside within the valence band and require an energy greater than or equal to the band gap to make the transition to the lowest unoccupied conduction band energy level. The horizontal offset between the top of the valence band and the bottom of the conduction band shows that diamond is an indirect band gap semiconductor.

4.2.6 Thermal conductivity

In general, good electrical insulators make poor thermal conductors. Sulphur, for example, has a thermal conductivity of $0.2\,\mathrm{W \cdot m^{-1}K^{-1}}$ and an electrical conductivity of just $5 \times 10^{-14}\,\mathrm{S \cdot m^{-1}}$.[24] The high thermal conductivity of diamond, along with its comparatively low electrical conductivity ($1 \times 10^{-11}\,\mathrm{S \cdot m^{-1}}$ or less) seem at first to be in contradiction of one another. In metals, the combination of both thermal and electrical conductivity is due to the free movement of electrons which carry both electronic charge and thermal energy.[18] In diamond with its wide band gap, electrons cannot flow and so are unable to conduct either charge or thermal energy. However, the strong, rigid bonds discussed in section 4.2.3 allow for a high degree of *phonon* transport,[25] the bonds themselves carrying thermal energy through the diamond lattice.

4.3 Diamond synthesis

Natural diamonds are typically either reserved for the jewellery industry or are of an insufficient quality for many industrial and research applications. As such, it has become necessary in the field to develop artificial fabrication methods, by which material properties[26, 27, 28] and dopant levels[29] can be tightly controlled.

Mimicking the natural formation process, high pressure high temperature (HPHT) diamond synthesis (see 4.3.1) takes either graphite (sp^2 carbon) or a diamond grit and exposes it to pressures typically exceeding 5 GPa and temperatures above 1500 K where diamond is a more stable allotrope than graphite.[30] Direct conversion of pure graphite to diamond however, even under conditions where diamond is stable, is difficult[31, 32] (see 4.5.1) due to the strong carbon-carbon sp^2 bonds which require high activation energies in order for the carbon atoms to be liberated for incorporation into diamond material. In order to lessen this energy

barrier then (see fig. 4.6) a metal catalyst/solvent such as iron, nickel and/or cobalt may be employed.[33]

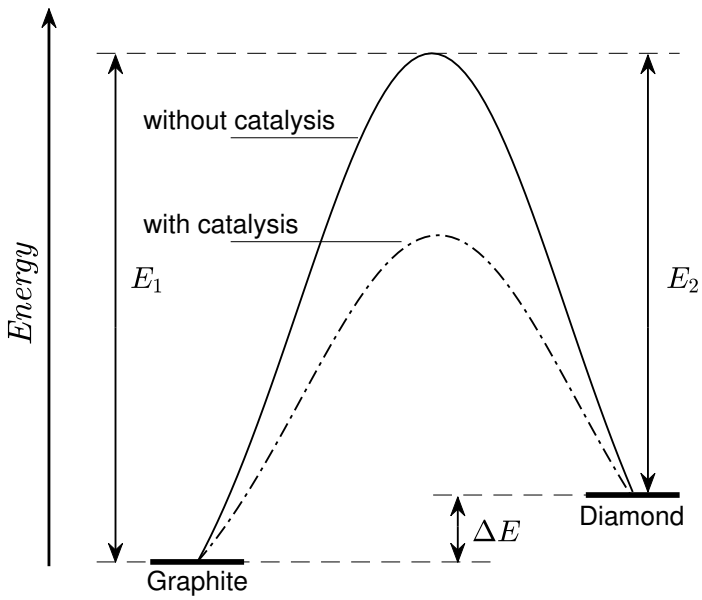

Figure 4.6: Though both diamond and graphite are stable at room temperature and pressure, carbon can be converted from one allotrope to the other by supplying sufficient energy to overcome the energy barrier, or activation energy, between them. This barrier can be reduced by the use of a metal catalyst in HPHT synthesis.

At lower temperatures and/or pressures, the sp^2 phase is stable whilst diamond (sp^3) is metastable. At higher temperatures and pressures, the reverse is true, with diamond being stable whilst sp^2 carbon is metastable.[34] The phase boundary between these regimes[35] is commonly known as the Berman-Simon[36] line (see figure 4.7).

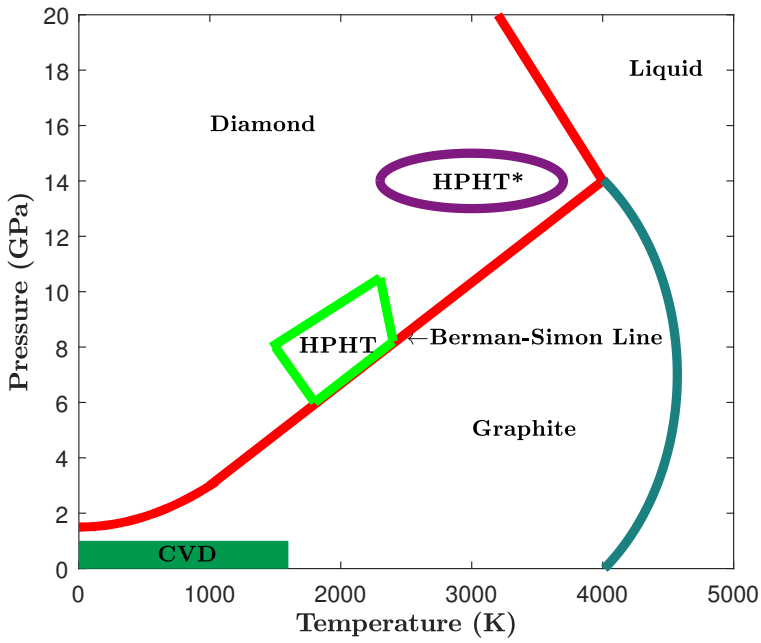

Figure 4.7: Phase diagram for carbon. Each synthesis method requires specific growth conditions, with two distinct regions for HPHT (using molten metal catalysts to reduce the formation temperature) and HPHT* (without catalysis). Chemical vapour deposition (CVD - see 4.3.2) takes place at comparatively low pressures and temperatures, well within the stable graphite region. It should be noted that the specific temperatures and pressures employed for CVD diamond synthesis have a significant effect on the size, quality and physical & chemical properties of the resulting material.

4.3.1 High Pressure High Temperature

Requiring extreme pressure, HPHT synthesis requires large 'cubic presses' or 'belt presses'. This process typically produces low strain material but does not always provide a convenient method for dopant control which can be important for some research and industrial applications.

In the temperature gradient growth (TGG) process,[37] large,[38] single crystal HPHT synthesis usually makes use of a seed crystal[39] embedded in a mixture of carbon

source material (graphite[40] or a diamond grit[41]) and a metal catalyst which is compressed until such temperatures ($\approx 1500\,\mathrm{K}$) and pressures ($> 5\,\mathrm{GPa}$) as the carbon can be dissolved into the molten catalyst. A temperature difference of a few tens of Kelvin[42] leads to a solubility gradient throughout the mixture, with the carbon solubility (and therefore the carbon concentration) greater in the higher temperature region. Migration of the carbon through diffusion and convection allows the carbon atoms to move towards the cooler region where they begin to precipitate onto the surface of the seed crystal (figure 4.8) which grows, forming a larger diamond crystal. This homo-epitaxial growth leads to low lattice mismatch and, therefore, low strain[43] in the resultant material.

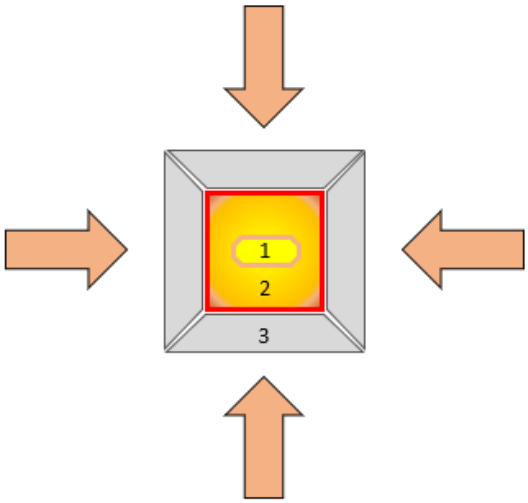

Figure 4.8: A schematic diagram of an HPHT press. The seed crystal (1) acts as foundation upon which carbon atoms precipitating from the graphite/catalyst mixture (2) can undergo homo-epitaxial growth. Pressure (indicated by the arrows) is applied via anvils (3).

Diamond grits up to several hundred microns or more[44] can be manufactured from non-diamond carbon, i.e. graphite, by also making use of a solubility difference, this time due to the greater solubility of non-diamond carbon under high temperature and pressure,[45] which dissolves in the catalyst and is allowed to spon-

taneously nucleate on the seed crystal surface(s). Multiple nucleation sites lead to multiple growth regions and non-single crystal growth ensues.

Nitrogen incorporation is common in these process due to atmospheric gas contained in the carbon-catalyst mixture which is difficult, though not impossible, to prevent. Typically, the level of nitrogen incorporation in the HPHT process results in material with approximately $100-500$ ppm of substitutional nitrogen ($N_S{}^0$) unless "nitrogen getters", additives which will bond with nitrogen and precipitate out of the diamond formation region, are used. These may reduce $N_S{}^0$ to less than 1 ppm, although boron may be incorporated at similar levels. However, nitrogen incorporation can often be more tightly controlled in CVD processes, as can the inclusion or exclusion of other dopants at the expense of creating more strained[46]material.

4.3.2 Chemical Vapour Deposition

Operating at comparatively low pressures (up to 200 mbar)[47] and substrate temperatures as low as a few hundred Celsius,[48, 49] the CVD process dissociates a mixture of gases containing hydrogen (H), oxygen (O) and carbon (C) by applying high intensity microwaves which cause the mixture to form a plasma (see figure 4.9). Mediated by the hydrogen (see 4.3.3), carbon atoms precipitate from this plasma onto a substrate typically of diamond, silicon or indium. The heteroepitaxial process (using a silicon or indium substrate) frequently results in highly strained or polycrystalline material[50] due to lattice mismatch between the substrate and the resulting diamond film. Also, the high (compared to ambient) temperatures in the synthesis chamber cause the substrate to thermally expand prior to deposition. When the substrate and deposited material are removed from the chamber and allowed to cool, they contract to different degrees, leading to a warped substrate and strained material.[51] Individual dislocations, i.e. abrupt changes in the arrangement of atoms within a crystal structure, and dislocation complexes can lead to strain within diamond material, as well as affecting birefringence.[52] These dislocations can be common at the

interface between the grown material and the substrate.[53]

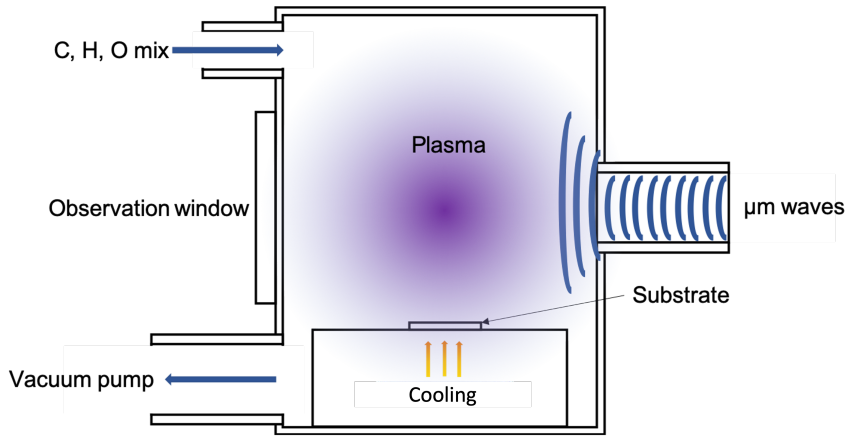

Figure 4.9: Simplified layout of a CVD reactor. Gases entering the vacuum chamber are separated into their constituent atoms by microwave radiation and assist the carbon in being deposited upon the substrate. Cooling may be applied beneath the substrate to control formation parameters.

Conditions within the synthesis chamber ('reactor') have a direct result on the physical properties of the resulting material. Substrate temperature,[49, 54] gas mixture ratios,[55] substrate material[56, 57] and substrate surface roughness (i.e. nucleation efficiency) all affect the growth process. Though adequate control of these factors[58] is necessary to ensure that diamond growth proceeds as expected, they may also be manipulated to produce diamond, either single crystal (SCD), microcrystalline (MCD), nanocrystalline (NCD) or ultrananocrystalline (UNCD) products with a degree of control over the resulting optical, thermodynamic and electronic properties. These polycrystalline diamond (PCD) forms typically develop through nucleation at multiple sites, which leads to the simultaneous growth of multiple crystallites. As these crystallites grow they may merge into a single polycrystalline film, leading to MCD, NCD or UNCD depending on the ratio of CH_4 to H_2 in the gas mixture.[59] Greater levels of CH_4 lead to a finer grain size, with UNCD having the finest grains. PCD usually contains a degree of sp^2 carbon deposition within grain boundaries between crystallites.[60, 61] The level of sp^2 carbon, and the cor-

responding grain size and other factors imparted by growth conditions can have a significant effect on the physical properties[62] of the grown material and therefore on the suitability of PCD material for certain applications.[63]

Strict limits on the precise mixture of the gases used determine the formation of diamond (figure 4.10) in the reactor, and dopants can be controlled closely by tailoring these gases to suit the requirements of the final product.[55] CVD material therefore can be fabricated with specific optical and electronic properties,[64] although due to high strain in the resulting crystal it may not be appropriate for certain applications, particularly where high degrees of mechanical stress are imparted on the diamond.

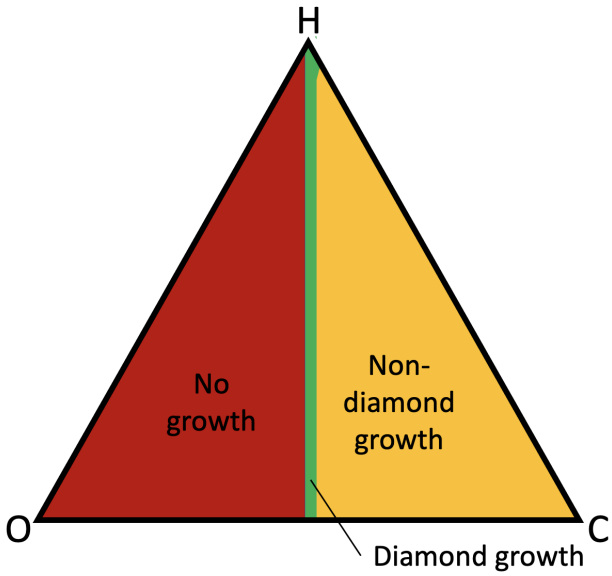

Figure 4.10: Varying atomic composition ratios of carbon, hydrogen and oxygen determine the feasibility of diamond growth. Each corner of the triangle denotes 100% composition by a particular element, with a fractional ratio between two elements leading down each edge, and a three element mixture anywhere within the triangle. Adapted from Bachmann, 1991.[55]

4.3.3 The role of hydrogen in CVD synthesis

The effect of hydrogen on the growth of diamond by CVD has been studied extensively,[65, 55] but the reason for the importance of this light element is not immediately evident, seeing as diamond itself does not necessarily contain hydrogen (although hydrogen defects are an active area of study). Instead of being incorporated in the diamond as a significant contributor to the material then, hydrogen must presumably take an active role in the diamond formation process.

In a microwave plasma reactor such as that shown in figure 4.9, the energy delivered by the microwaves (or by a hot filament or other heat source in differing reactors) is able to dissociate H_2 into its atomic form,[66] which is prevented from recombining into the molecular form by the chamber pressure. This atomic hydrogen is effective at etching away sp^2 carbon but less efficient at etching diamond. More than this though, the atomic hydrogen is able to take part in hydrogen abstraction reactions with hydrocarbon species which have bonded to the substrate and/or diamond surface by recombining with the H to form H_2. This leaves the remaining carbon species attached to the growing diamond crystal.[67] A number of hydrocarbon species, almost exclusively involving C_1 molecules, in a number of processes facilitate this hydrogen mediated growth.[67] One possible method is shown in fig.4.11.

4.4 The nitrogen vacancy centre

Nitrogen incorporated as substitutional nitrogen ($N_S^{0/+}$), nitrogen-vacancy-hydrogen defects ($NVH^{-/0}$) and nitrogen vacancies ($NV^{-/0}$) constitutes the dominant impurity in CVD diamond, with the ratio of $N_S^{0/+}$:$NVH^{-/0}$:$NV^{-/0}$ expected to be approximately 300:30:1.[69] $N_S^{0/+}$, being the most prevalent form of nitrogen incorporation, can play an important role in the determination of the charge state of other defects. Aside from nitrogen, other impurities such as Si and H may also be incorporated, however, this section will focus on the nitrogen vacancy (NV) colour centre.

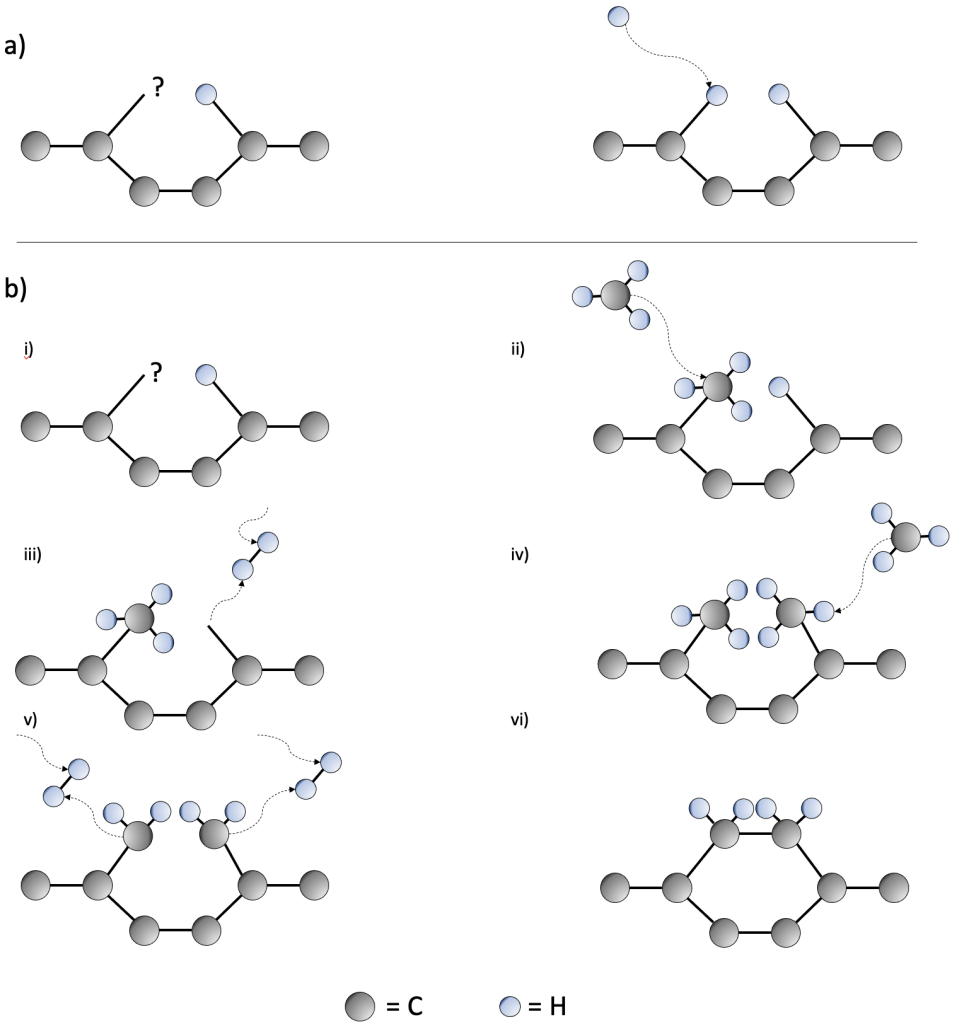

Figure 4.11: One possible mechanism of hydrogen mediated diamond growth in the CVD process. a) In most cases, dangling bonds on the growth surface are simply occupied by atomic hydrogen drawn from the gas mixture. b) However, (ii)sometimes a CH_3 molecule may occupy this site. (iii)A neighbouring H atom may also recombine with a loose H atom to form molecular hydrogen, leaving a dangling bond adjacent to the CH_3. (iv) This dangling bond may also become occupied by a second CH_3 and (v) each of these CH_3s may lose an H atom, becoming CH_2. (vi) The two carbon atoms now each have a spare bond which they now join together, becoming fully part of the diamond surface with two attached hydrogen atoms each, which may now continue the process from step (i). Note that atom sizes, bond lengths and bond angles are not to scale in this diagram. Adapted from[68] and.[67]

The nitrogen vacancy colour centre in diamond is a point crystallographic defect comprised of a single substitutional nitrogen atom and an adjacent lattice vacancy (figure 4.12). This defect maintains one of three charge states; neutral (NV^0), negative (NV^-)[70, 71] and the positive charge state (NV^+),[72] and over the past few decades it is the negative charge state which has attracted the most attention.

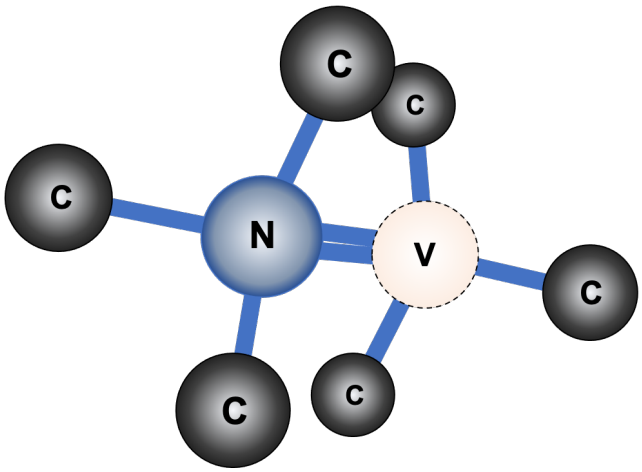

Figure 4.12: Two carbon atoms (C) in the diamond lattice are removed and replaced with a nitrogen atom (N) and a lattice vacancy (V) to form the nitrogen vacancy defect.

The reason for this attention can be attributed to the NV^-'s optical and spin properties. Being a spin-1 system[9] and having C_{3v} symmetry,[73] it is active in both electron paramagnetic resonance (EPR) and optically detected magnetic resonance (ODMR) experiments. The nitrogen vacancy is explored in more detail in chapter 5.

4.5 Fabrication of nanodiamonds

Fluorescent nanodiamonds containing both single and multiple NV^-s are of interest in a number of avenues of scientific inquiry, with the properties of the precursor material and the methods of manufacture having important effects on the suitability of resulting nanodiamonds for their particular area of usefulness.

The particular fabrication method employed to produce nanodiamond (ND) samples can have a considerable effect on the physical and chemical properties[74] of the NDs themselves. In particular, the resultant size and surface chemistry can lead to changes in the behaviour of the NV centre.[75]

4.5.1 Detonation Nanodiamonds

First fabricated in 1963[76] detonation shockwave assisted synthesis (DSAS) uses the pressure generated at an explosive shock front[77] to achieve extreme temperatures ($3000 - 4200\,\mathrm{K}$[78]) and pressures ($18 - 35\,\mathrm{GPa}$[78]), even higher than those seen in HPHT presses, for extremely short time periods.[79] This rapid synthesis leads to small diamond crystals, generally on the scale of a few nanometres, due to the minuscule time available for crystallisation, compared to e.g. CVD synthesis which may continue for many hours or days. Though these diamonds can be desirable for many applications due to this small size (4-5nm),[80] this along with high surface graphite (sp^2) accumulation[81] makes them unsuitable for many quantum sensing and information applications where larger nanodiamonds and highly transparent material is required for practical excitation and probing of colour centres.

4.5.2 Ball milling

The ball milling process

Ball milling is a mechanical process by which materials or particles of material may be reduced in size via impact and attrition[82] by a milling material in the form of balls which reside within a rotating drum. As the drum rotates (see figure 4.13), the milling balls are carried to the top half of the drum where gravity causes them to fall down onto the material to be milled (precursor material). It is these impacts, as well as grinding actions as the balls and material move around the base of the drum, which lead to the mechanical erosion of the precursor material into smaller pieces. Ball milling apparatus may measure from a few centimetres[83] up to several metres

in length.[84] In general (i.e. not specifically milling of diamond), ball milling has a number of advantages and disadvantages over competing methods of fabrication. Advantages include:[85]

- chemically simple[86] - fewer or no chemical solvents are required for the production of materials, compared to many 'wet' synthesis approaches,
- high yield[87] - large amounts of desired material can be produced with respect to the amount of precursor material consumed,
- mechanically simple[88] - depending on the materials involved, ball mills may be simple to manufacture and operate and are both reliable and safe,
- consistent[89] - provided milling materials are replenished as they wear and operating conditions remain constant, resulting powders should require no homogenisation.

Disadvantages include:[85]

- bulk - some milling machines can be large and heavy,
- energy consumption - large ball mills may consume high amounts of energy which is consumed by rotational motion and wear of milling balls rather than milled material

Broadly, the synthesis of materials using ball milling can be split into two categories:[90]

- mechanical alloying (MA) where two or more materials are combined to form a composite powder, or
- mechanical grinding (MG) where a single precursor material is processed to form a single material powder.

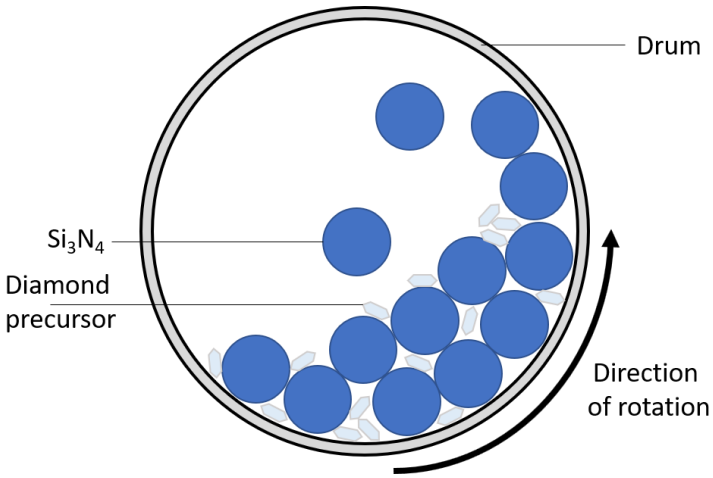

Figure 4.13: Ball milling uses mechanical crushing to reduce diamond precursor to a nanodiamond powder. The drum rotates causing the milling balls to grind the precursor material gradually, with the size distribution of the resulting powder determined by the material of the milling balls, the size of balls and drum and the duration of the milling process.

Ball milling can also be used to break materials into smaller molecular components and for the production of organic compounds[91] in what is termed a mechanochemical (MC) process.[92]

Due to the wide range of applications for ball milling synthesis,[85] there is a similarly wide range of parameters contributing to the efficacy and consistency of resulting material. Firstly, the physical properties of the material to be milled will have an impact on the material chosen for the milling balls. Harder materials will require balls to be sufficiently hard so that it is the desired material which is eroded rather than the balls themselves. This in turn has an effect on how the balls erode the walls of the milling chamber and vice-versa.[93] The mass of the grinding balls has an impact on the size of resulting particles, with balls that are too light failing to crush the material at all.[94] The rotational speed of the milling chamber also has an effect on the efficacy of the grinding process, with faster milling leading to decreased particle size,[95] although presumably at sufficiently high rotational speeds,

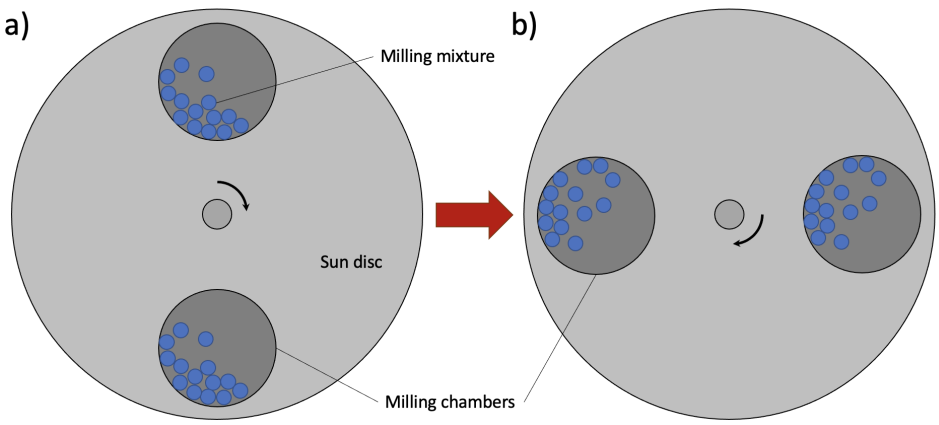

Figure 4.14: In a planetary mill, one or more milling chambers orbit a common centre of rotation on a 'sun' disc. This offset from the centre leads to higher kinetic energy in the milling mixture (balls and precursor material) and greater velocity differences between particles. In a) the milling mixture is falling down the side of the chamber due to gravity, as will a simple mill. However, in b) the rotation of the sun disc means that particles fall from a greater height and are moved with greater force, leading to more effective milling.

mechanical grinding is reduced to zero as centripetal forces restrict movement of the balls away from the chamber walls, preventing mechanical action.

Planetary ball mills

The most simple form of ball mill consists of a single rotating drum containing the material to be milled and the milling balls. However, higher energies and greater differences in velocities between balls and precursor material can be achieved by the use of a planetary mill.[88] In this configuration, one or more milling chambers are sited on a 'sun' disc away from the axis of rotation.

Ball milling of diamond nanoparticles

Ball milling of diamond has led to the production of tailor-made nanodiamonds with a high degree of control over contaminants (particularly metals) in the resultant powder.[96] For the research detailed in this thesis, precursor diamond material (see

section 5.5 for details) was placed into a Pulverisette 7 planetary mill with balls of silicon nitride (Si_3N_4). The mechanical action between the milling balls and the precursor material resulted in the formation of a nanodiamond powder. Due to the random and destructive nature of the process, a wide size distribution is found in the subsequent material (figure 4.15).

Diamond, being among the hardest of materials, is by its nature difficult to cut or abrade using conventional materials. With a Mohs hardness of around 8.5, Si_3N_4 is as prone to damage as the diamond in this process, if not more, which was suspected to lead to high levels of silicon nitride contamination in the nanodiamond powder. This contamination was hinted at when the author inspected ball milled diamond powders with energy dispersive X-ray (EDX) analysis under scanning electron microscopy (SEM)(see fig. 4.16). This method, which measures atomic weight across a sample, enabled the positive identification of silicon deposits throughout the diamond powders either covering diamond particles or forming particles entirely comprised of silicon-based material. This Si contamination can be reduced by treatment with phosphoric acid which in turn leads to silicon dioxide contamination which can be again reduced by treatment with sodium hydroxide. Leaving sodium silicate, this final contaminant is water soluble and can be washed off, leaving a relatively clean nanodiamond powder with an expected oxygen termination. This cleaning process was performed by Soumen Mandal at Cardiff University.

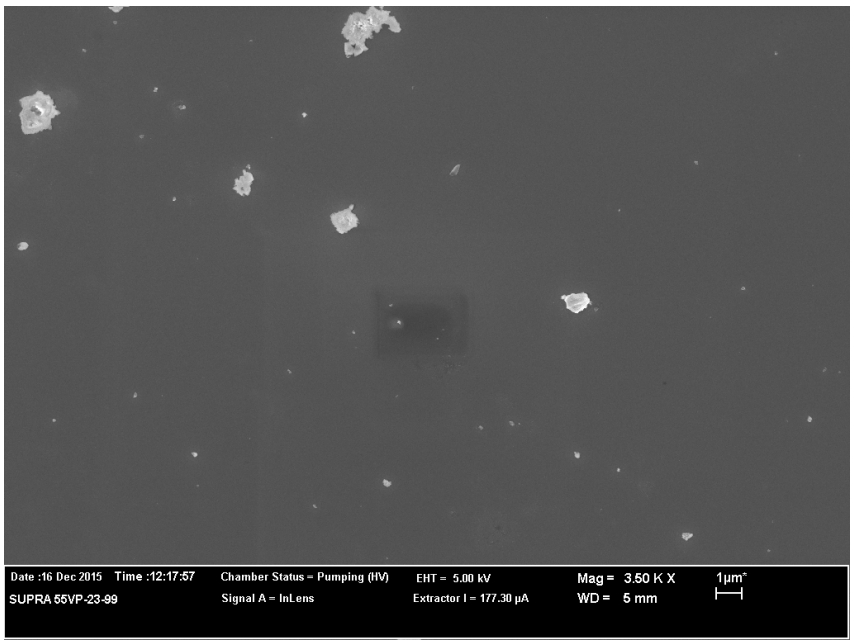

Figure 4.15: Scanning electron microscopy (SEM) image of ball milled nanodiamonds. Dimensions range from a few nanometres to a few microns in diameter.

Steel balls can be used in the milling process[96] in place of silicon nitride, leading to metallic contaminants and a more spherical shape in the nanodiamonds produced. The effect of the milling ball material leads to flexibility in the final product which can therefore be tailored to specific applications.

This methodology may yield in excess of fifteen percent weight-for-weight[97] of the original mass milled (though some portion of this mass could be represented by e.g. sp^2 carbon), significantly higher than other non-detonation methods such as nano-pillar etching.[98, 99]

4.5.3 Nanopillars

High quality, low yield[100] nanodiamonds can be fabricated in the form of so-called 'nanopillars' or 'nanograss'. By depositing metallic masks and etching away the surrounding material, these NDs can have excellent spin properties.[100, 101] However, the low yield and complex manufacturing process involved can be prohibitive for

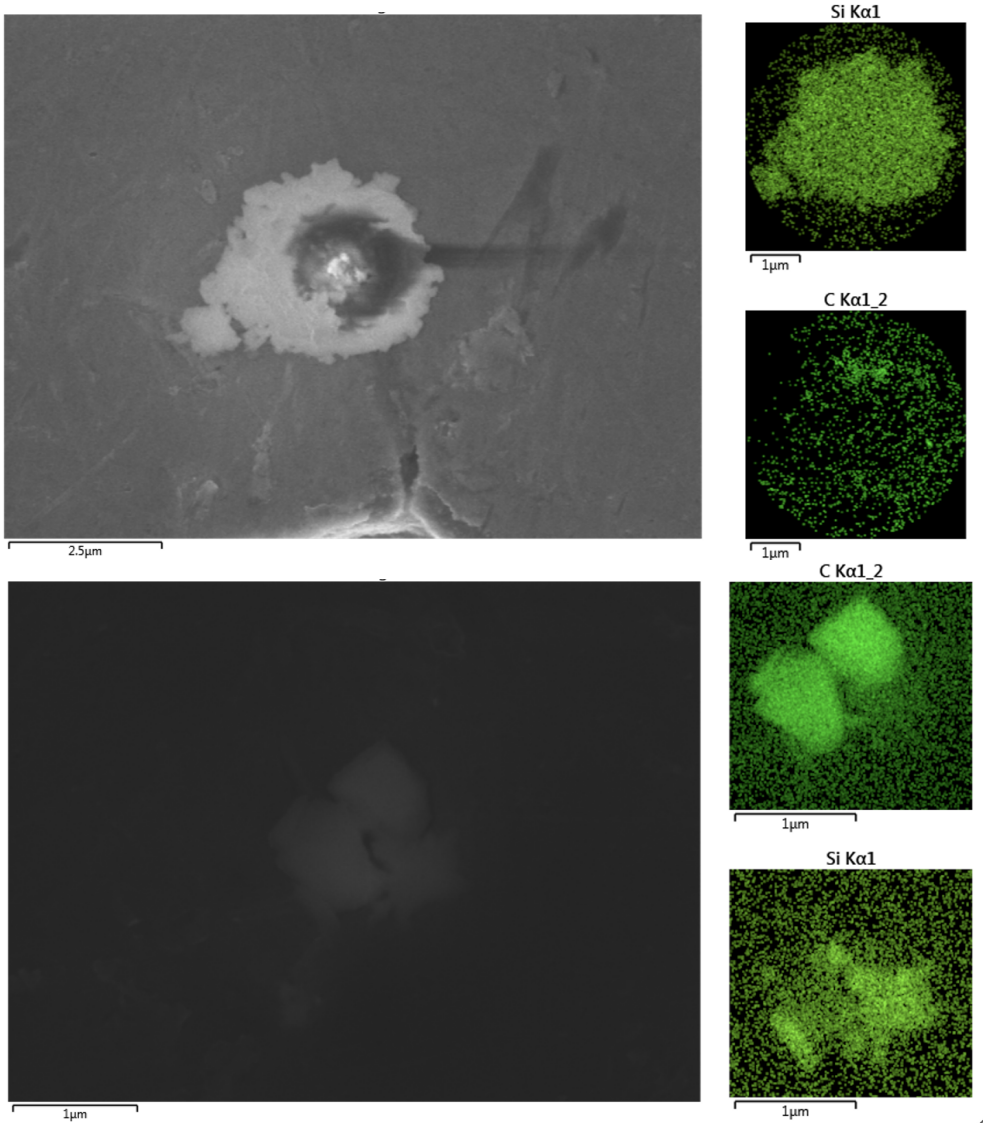

Figure 4.16: SEM images (left) of two suspected diamond particles. EDX analysis (right) showed that whilst carbon (most likely diamond) was present at both sites, silicon contamination was also present, in some cases more so than the carbon, suggesting widespread contamination.

many applications.

Table 4.1 provides a brief comparison of nanodiamonds produced by three main methods.

Fabrication Method	Detonation[102, 103]	Nanopillars[99]	Ball milling[96, 97]
Size range	$\leq$10 nm	Any	Any
Surface contaminants	High	Low	Moderate
Yield	High	Low	High
Notes	Agglomeration of NDs	Complex process	Irregularly shaped NDs

Table 4.1: Qualitative comparison of nanodiamonds produced by three fabrication methods.

4.5.4 Treatment of nanodiamonds

Electron irradiation

Nitrogen in the diamond lattice is typically 'grown-in' during the manufacturing stage as single substitutional nitrogen (N_s^0),[104, 105] and such nitrogen atoms are therefore available for the creation of nitrogen vacancies, although without processing these do occur in small numbers.[106] Vacancies themselves however, though they may be created in small numbers during growth,[107] must be added at a later date in order to be present in sufficient concentrations for large scale NV production (it should be noted that at around 900 K vacancies may become mobile[108]). This can be achieved by electron irradiation,[109, 110] with electron energies of $\geq$ 145 keV required to displace a carbon atom from the diamond lattice.[111] The irradiation process sees energetic electrons bombarding the diamond lattice and creating damage where they encounter carbon atoms which are displaced, leaving a vacant lattice site.[112] The efficiency of vacancy creation using this process depends on electron beam energy and intensity.[113]

Annealing

Though electron irradiation alone can lead to NV creation,[114] this is less efficient than annealing after the irradiation step has been completed. Recent work[110] also suggests that simultaneous irradiation and annealing may be more efficient again. Annealing diamond at temperatures ranging from $\approx 700\,\mathrm{K}$ to $1500\,\mathrm{K}$ allows vacancies to migrate through the diamond lattice before joining with a substitutional nitrogen atom to form an NV.[115] Note that at temperatures above $\approx 1400\,^{\circ}\mathrm{C}$ the NV becomes unstable and "anneals out", forming alternative nitrogen impurities. The conversion efficiency of vacancies and nitrogen to NVs depends on the annealing conditions. Using a method detailed by Chu et al.,[116] a V:NV conversion rate of 10% is expected with excess nitrogen remaining as $N_s{}^0$.

4.6 Surface Chemistry

The surface of smaller nanodiamonds makes up a considerable proportion of the atoms which make up the particle. As the structure and makeup of the surface differ from that of the bulk material, the behaviour of the nanodiamond as a whole is necessarily altered.

4.6.1 Termination

Four main surface terminations are considered for nanodiamond; reconstructed termination, where the surface of the diamond is comprised of sp^2 carbon-carbon bonds, and oxygen, nitrogen or hydrogen termination, where atoms or molecular species containing these elements form the outermost layers of the particle. However, it should be noted that in real world cases, the surface of diamond is likely to comprise of a mixture of terminations with wide and varied chemistry[117] occurring due to e.g. multiple C-O bonding regimes[118, 119] & the presence of carboxyl[120] groups and other chemical species during the formation or alteration of the diamond surface.

Reconstructed surface

Depending on the crystallographic plane which makes up a portion of a surface, highly ordered π-bonds may be encouraged to form by either thermal treatment[121] or electron irradiation[122] within a vacuum.

Oxygen termination

Usually, oxygen termination of the [001] surface takes one of two forms; oxygen double bonded to a single carbon atom, the so called 'ketone arrangement',[118] and an oxygen atom being singly bonded to two carbon atoms, forming a bridge.[119] These terminations can be achieved by annealing diamond or nanodiamond samples in an oxygen atmosphere, with control of the relative abundance of sp^2 and sp^3 bonded carbon at the surface possible.[123]

Hydrogen termination

Effective hydrogen termination of the nanodiamond surface can be complex, more often than not leading to the formation of hydroxyl functions.[124] However, effective hydrogenation of the diamond surface can be achieved by the application of H_2[125] at high temperature,[126, 127] although these methods are not without complications. The size of the nanodiamonds being terminated is also significant, as at small scales (<100 nm) the temperatures required for this kind of termination can cause graphetisation of the diamond.[128, 129]

Nitrogen termination

A fully or partially nitrogen terminated surface can be achieved by the application of a nitrogen plasma in a CVD reactor[130, 131] or by molecular beam epitaxy (MBE).[132] Simulated results[131] suggest that nitrogen surface termination is preferable where the spin properties of the NV^- are of chief concern. Multiple surface terminations making use of nitrogen as the terminating element are possible.[130]

Alternative terminations

A wide variety of surface terminations can be achieved, dependent on the physical properties required. Examples of such terminations include, but are not limited to:

- sulphur[133] and oxygenated sulphur[134]
- halogenation[135]
- fluorine[136]

4.7 Elemental Purity

Carbon-12 has no net nuclear spin and so is inactive in terms of magnetic resonance effects. However, unless a diamond is isotopically purified, the effects of carbon-13, which is active in magnetic resonance, become significant. Atomic defects, such as substitutional nitrogen, can also have an effect on the behaviour of the NV centre.[137]

4.7.1 Carbon isotopes

Carbon naturally occurs in three isotopic forms; ^{12}C, ^{13}C and ^{14}C, the latter of which is a radioisotope only found in trace amounts. ^{12}C and ^{13}C however are stable isotopes[138] and occur with natural abundances (a) of 98.9% and 1.1% respectively.[139] ^{12}C has no net nuclear spin[140] and so, as a result, is inactive in terms of magnetic resonance. This, due to its dominant abundance, makes up the majority of the diamond lattice. ^{13}C however has a nuclear spin $I_{^{13}C} = \frac{1}{2}$ and therefore is able to interact with paramagnetic centres such as the NV. This interaction leads to increased decoherence of the NV spin state and is therefore significant where long coherence times are required.

4.7.2 Nitrogen

In chemical vapour deposition (CVD) diamond, nitrogen is generally incorporated into the lattice during growth,[141] although it can be added later by ion implantation in some cases. Not only are ^{14}N ($I_{^{14}N} = 1$, $a_{^{14}N} > 99.6\%$) and ^{15}N ($I_{^{15}N} = \frac{1}{2}$, $a_{^{15}N} < 0.4\%$ where I is the nuclear spins and a is the natural abundance) active in magnetic resonance, substitutional nitrogen defects in the diamond lattice can absorb incoming electromagnetic radiation (specifically around visible wavelengths which are used for spin polarisation and read out of the NV$^-$ spin state) and subsequently cause heating which can pose a challenge for certain applications. Decoherence due to spin-spin interactions between the electron spin of substitutional nitrogen and the NV centre is well documented,[137] and heating of nanodiamonds due to absorption by nitrogen defects has been shown to be deleterious in optical levitation.[128]

4.8 Effect of Size

Section 4.6 discusses the existence of defects and spins on the surface of nanodiamonds, but these factors become more or less significant dependent on the overall size of the nanodiamond in question. The size of the ND also has ramifications for many of the prospective applications for which it might be considered.

The ratio of surface area to volume (see figure 4.17) is significant to the chemical and physical properties of nanodiamonds.

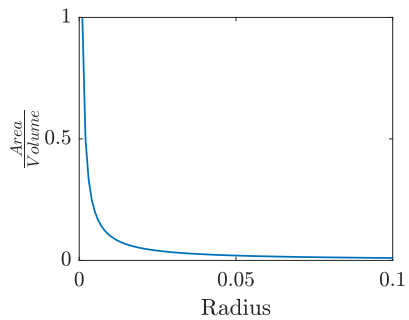

Figure 4.17: The ratio of nanodiamond surface area to bulk volume decreases rapidly.

This effect primarily arises due to the presence of surface molecules such as COOH and carboxyl groups among others, whose chemistry differs from that of the bulk diamond material. Under such circumstances the nanodiamond will react with overall chemical properties more akin to the surface than to the bulk material. From the perspective of physical processes (as opposed to chemical processes), it is the presence of surface electron spins which is of relevance. These spins can interact with nitrogen vacancies (or other defects) within the bulk material, leading to shortened coherence times (see chapter 5).

Absolute dimensions of the ND are also important for similar reasons. The larger a given ND, the less likely an NV is to be in close enough proximity to the surface to interact with surface spins. Therefore, on average we would expect larger NDs to contain NVs with longer coherence times.

Chapter 4 References

[1] J Angus and C Hayman. Low-pressure, metastable growth of diamond and "diamondlike" phases. *Science*, 241(4868):913–921, 1988.

[2] R. J. Nemanich, J. A. Carlisle, A. Hirata, and K. Haenen. CVD diamond-Research, applications, and challenges. *MRS Bulletin*, 39(6):490–498, Jun 2014.

[3] J. E. Field. *The Properties of Natural and Synthetic Diamond*. Academic Press, London, 1992.

[4] W H Bragg and W L Bragg. The structure of the diamond. *Nature*, 91(91):557, 1913.

[5] F. Bridges and G. Davies and J. Robertson and A. M. Stoneham. The spectroscopy of crystal defects: a compendium of defect nomenclature. *J. Phys.: Condens. Matter*, (2):2875–2928, 1990.

[6] A. M. Zaitsev. *Optical Properties of Diamond*. Springer (Berlin), 2001.

[7] Alison Mainwood. Substitutional impurities in diamond. *Journal of Physics C: Solid State Physics*, 12(13):2543, 1977.

[8] F P Larkins and A M Stoneham. Lattice distortion near vacancies in diamond and silicon. i. *Journal of Physics C: Solid State Physics*, 4(13):143, 1971.

[9] Marcus W. Doherty, Neil B. Manson, Paul Delaney, Fedor Jelezko, Jörg Wrachtrup, and Lloyd C. L. Hollenberg. The nitrogen-vacancy colour centre in diamond. *Physics Reports*, 528(1):1 – 45, 2013.

[10] V. L. Solozhenko and D. Andrault and Y. Le Godec and M. Mezouar. Ultimate Metastable Solubility of Boron in Diamond: Synthesis of Superhard Diamondlike BC_5. *Phys. Rev. Lett.*, 102:015506, 2009.

[11] G. Chai and Q. Chen. Characterization Study of the Thermal Conductivity of Carbon Nanotube Copper Nanocomposites. *Journal of Composite Materials*, 44(24):2863–2873, Nov 2010.

[12] Richard P. Mildren. *Optical Engineering of Diamond*. Wiley-VCH Verlag GmbH & Co. KGaA, first edition edition, 2013.

[13] P. Chakraborty, G. Xiong, L. Cao, and Y. Wang. Lattice thermal transport in superhard hexagonal diamond and wurtzite boron nitride: A comparative study with cubic diamond and cubic boron nitride. *Carbon*, 139:85 – 93, 2018.

[14] R. Diversi, A. Bartolini, and L. Benini. Thermal Model Identification of Computing Nodes in High-Performance Computing Systems. *IEEE Transactions On Industrial Electronics*, 67(9):7778–7788, Sep 2020.

[15] P. Millar, R. B. Birch, A. J. Kemp, and D. Burns. Synthetic diamond for intracavity thermal management in compact solid-state lasers. *IEEE Journal of Quantum Electronics*, 44(7-8):709–717, Jul-Aug 2008.

[16] S. Guo, L. Yang, B. Dai, F. Geng, V. Ralchenko, J. Han, and J. Zhu. Past Achievements and Future Challenges in the Development of Infrared Antireflective and Protective Coatings. *Physica Status Solidi A - Applications and Materials Science*, 217(16), AUG 2020.

[17] L. Huang, T. Wang, X. Li, X. Wang, W. Zhang, Y. Yang, and Y. Tang. UV-to-IR highly transparent ultrathin diamond nanofilms with intriguing performances: Anti-fogging, self-cleaning and self-lubricating. *Applied Surface Science*, 527, Oct 2020.

[18] J. Singleton. *Band theory and electronic properties of solids.* Oxford University Press, 2001.

[19] R.F. Mamin and T. Inushima. Conductivity in boron-doped diamond. *Physical Review B*, 63(3), 2001.

[20] Y. Dai, D. Dai, C.X. Yan, B.B. Huang, and S.H. Han. N-type electric conductivity of nitrogen-doped ultrananocrystalline diamond films. *Physical Review B*, 71(7), 2005.

[21] M.N.R. Ashfold, J.P. Goss, B.L. Green, P.W. May, M.E. Newton, and C.V. Peaker. Nitrogen in diamond. *Chemical Reviews*, 120(12):5745–5794, 2020.

[22] R Kalish. The search for donors in diamond. *Diamond and Related Materials*, 10(9-10):1749–1755, 2001.

[23] A. Stoyanova, A. O. Mitrushchenkov, L. Hozoi, H. Stoll, and P. Fulde. Electron correlation effects in diamond: A wave-function quantum-chemistry study of the quasiparticle band structure. *Physical Review B*, 89(23), 2014.

[24] D. R. Lide. *Handbook of Chemistry and Physics.* CRC Press, 71st edition, 1991.

[25] G. A. Slack. Thermal Conductivity of Pure and Impure Silicon, Silicon Carbide, and Diamond. *Journal of Applied Physics*, (35):3460, 1964.

[26] Yuri N. Palyanov, Igor N. Kupriyanov, Alexander F. Khokhryakov, and Yuri M. Borzdov. High-pressure crystallization and properties of diamond from magnesium-based catalysts. *CrystEngComm*, 19:4459–4475, 2017.

[27] J. J. Gracio, Q. H. Fan, and J. C. Madaleno. Diamond growth by chemical vapour deposition. *Journal of Physics D - Applied Physics*, 43(37), Sep 2 2010.

[28] CF Chen, SH Chen, and KM Lin. Electrical properties of diamond films grown at low temperature. *Thin Solid Films*, 270(1-2):205–209, Dec 1995.

[29] R. Kalish. Doping of diamond. *Carbon*, 37(5):781 – 785, 1999.

[30] Y.N. Palyanov, I.N. Kupriyanov, A.F. Khokhryakov, and V.G. Ralchenko. 17 - Crystal Growth of Diamond. In Peter Rudolph, editor, *Handbook of Crystal Growth (Second Edition)*, Handbook of Crystal Growth, pages 671–713. Elsevier, Boston, second edition edition, 2015.

[31] Bundy F.P. Direct conversion of graphite to diamond in static pressure apparatus. *Journal of Chemical Physics*, 38(3):631, 1963.

[32] P.S. DeCarli and J.C. Jamieson. Formation of diamond by explosive shock. *Science*, 134(3472):92–92, 1961.

[33] Larissa F. Dobrzhinetskaya. Microdiamonds - Frontier of ultrahigh-pressure metamorphism: A review. *Gondwana Research*, 21(1):207 – 223, 2012.

[34] V.D. Blank, V.D. Churkin, B.A. Kulnitskiy, I.A. Perezhogin, A.N. Kirichenko, V.N. Denisov, S.V. Erohin, P.B. Sorokin, and M. Yu Popov. Phase diagram of carbon and the factors limiting the quantity and size of natural diamonds. *Nanotechnology*, 29(11):115603, Feb 2018.

[35] R. Berman. *Properties & Growth of Diamond*. INSPEC, the Institute of Electrical Engineers, 1994.

[36] F. P. Bundy, H. P. Bovenkerk, H. M. Strong, and R. H. Wentorf Jr. Diamond-Graphite Equilibrium Line from Growth and Graphitization of Diamond.

[37] Zang Chuan-Yi, Jia Xiao-Peng, Ren Guo-Zhong, and Wang Xian-Cheng. Dependence of Growing High-Quality Gem Diamonds on Growth Rates by Temperature Gradient Method. *Chinese Physics Letters*, 21(8):1648–1650, jul 2004.

[38] H.M. Strong and R.M. Chrenko. Further studies on diamond growth rates and physical properties of laboratory-made diamond. *Journal of Physical Chemistry*, 75(12):1838, 1971.

[39] Meiguang Zhang, Haiyan Yan, and Fang Peng. Analysis of the Phenomena of Diamond Synthesis by Seeding with Diamond. *Journal of Materials Science & Technology*, 24(5):809–812, Sep 2008.

[40] Y. Zhang, C. Zang, H. Ma, Z. Liang, L. Zhou, S. Li, and X. Jia. Hpht synthesis of large single crystal diamond doped with high nitrogen concentration. *Diamond and Related Materials*, 17(2):209–211, 2008.

[41] Zang C.and Chen X., Hu Q., Ma H., and Jia X. Mechanism of diamond-to-graphite transformation at diamond-stable conditions. *Chinese Science Bulletin*, 54(14):2535–2538, Jul 2009.

[42] Y. Babich, B. Feigelson, and A.I. Chepurov. Stages of the temperature gradient growth of hpht diamonds. *High Temperatures - High Pressures*, 44:93–103, 01 2015.

[43] Masfer Alkahtani, Johannes Lang, Boris Naydenov, Fedor Jelezko, and Philip Hemmer. Growth of High-Purity Low-Strain Fluorescent Nanodiamonds. *ACS Photonics*, 6(5):1266–1271, May 2019.

[44] Zhou S., Zang C., Ma H., Li X., Zhang H., and Jia X. Study on growth of coarse grains of diamond with high quality under HPHT. *Chinese Science Bulletin*, 54(1):163–167, 2009.

[45] L.W. Yin, M.S. Li, D.S. Sun, F.Z. Li, and Z.Y. Hao. Some aspects of diamond crystal growth at high temperature and high pressure by TEM and SEM. *MAaterials Letters*, 55(6):397–402, Sep 2002.

[46] H. Windischmann, G.F. Epps, Y. Cong, and R.W. Collins. Intrinsic stress in diamond films prepared by microwave plasma cvd. *Journal of Applied Physics*, 69(4):2231–2237, 1991.

[47] A comparison of low-pressure CVD synthesis of diamond and c-BN. *International Journal of Refractory Metals and Hard Materials*, 14(1):145 – 157, 1996.

[48] YZ Wan, DW Zhang, ZJ Liu, and JT Wang. Effects of temperature and pressure on CVD diamond growth from the C-H-O system. *Applied Physics A - Materials Science & Processing*, 67(2):225–231, 1998.

[49] J. Stiegler, T. Lang, M. Nygard-Ferguson, Y. von Kaenel, and E. Blank. Low temperature limits of diamond film growth by microwave plasma-assisted CVD. *Diamond and Related Materials*, 5(3):226–230, 1996.

[50] J.A. Baglio, B.C. Farnsworth, S. Hankin, G. Hamill, and D. O'Neil. Studies of Stress Related Issues in Microwave CVD Diamond on (100) Silicon Substrates. *Thin Solid Films*, 212(1-2):180–185, 1992.

[51] L. Schäfer, X. Jiang, and C.-P. Klages. In-situ Measuring of Stress Development in Diamond Thin Films, journal=Materials Science Monographs. 73(C):121–128, 1991.

[52] P. M. Martineau, S. C. Lawson, A. J. Taylor, S. J. Quinn, D. J. F. Evans, , and M. J. Crowder. Identification of Synthetic CVD Diamond. *Gems and Gemology*, 40.

[53] M.P. Gaukroger, P.M. Martineau, M.J. Crowder, I. Friel, S.D. Williams, and D.J. Twitchen. X-ray topography studies of dislocations in single crystal cvd diamond. *Diamond and Related Materials*, 17(3):262–269, 2008.

[54] H. Guo and M. Alam. Residual stress in cvd diamond films. *Materials Science Monographs*, 73(C):149–154, 1991.

[55] P.K. Bachmann, D. Leers, and H. Lydtin. Towards a general concept of Diamond Chemical Vapor-Deposition. *Diamond and Related Materials*, 1(1):1–12, 1991.

[56] J J Gracio, Q H Fan, and J C Madaleno. Diamond growth by chemical vapour deposition. *Journal of Physics D: Applied Physics*, 43(37):374017, sep 2010.

[57] Y. Zhao, Ya. Guo, L. Lin, Y. Zheng, L. Hei, J. Liu, J. Wei, L. Chen, and C. Li. Comparison of the quality of single-crystal diamonds grown on two types of seed substrates by MPCVD. *Journal of Crystal Growth*, 491:89–96, Jun 1 2018.

[58] P. W. May, M. N. R. Ashfold, and Yu. A. Mankelevich. Microcrystalline, nanocrystalline, and ultrananocrystalline diamond chemical vapor deposition: Experiment and modeling of the factors controlling growth rate, nucleation, and crystal size. *Journal of Applied Physics*, 101(5), Mar 1 2007.

[59] V.S. Sedov, A.K. Martyanov, A.A. Khomich, S.S. Savin, E.V. Zavedeev, and V.G. Ralchenko. Deposition of diamond films on Si by microwave plasma CVD in varied CH_4-H_2 mixtures: Reverse nanocrystalline-to-microcrystalline structure transition at very high methane concentrations. *Diamond and Related Materials*, 109:108072, 2020.

[60] A Dychalska, P Popielarski, W Frankow, K Fabisiak, K Paprocki, and M Szybowicz. Study of CVD diamond layers with amorphous carbon admixture by Raman scattering spectroscopy. *MAaterials Science-Poland*, 33(4):799–805, Dec 2015.

[61] K.Y. Teng, H.C. Chen, H.Y. Chiang, C.C. Horng, H.F. Cheng, K.J. Sankaran, N.H. Tai, C.Y. Lee, and I.N. Lin. The role of nano-graphite phase on the enhancement of electron field emission properties of ultrananocrystalline diamond films. *Diamond and Related Materials*, 24:126–133, 2012.

[62] H. Cheng, C. Yang, L. Yang, K. Peng, C. Chia, S. Liu, I. Lin, and K. Lin. Effective thermal and mechanical properties of polycrystalline diamond films. *Journal of Applied Physics*, 123(16), Apr 28 2018.

[63] Irena Kratochvilova. Polycrystalline diamond thin films for advanced applications. In Adrian M.T. Silva and Sonia A.C. Carabineiro, editors, *Advances in Carbon Nanostructures*, chapter 8. IntechOpen, Rijeka, 2016.

[64] A. Gicquel, K. Hassouni, F. Silva, and J. Achard. CVD diamond films: from growth to applications. *Current Applied Physics*, 1(6):479–496, 2001.

[65] J. E. Butler, R. L. Woodin, L. M. Brown, and P. Fallon. Thin film diamond growth mechanisms [and comment]. *Philosophical Transactions: Physical Sciences and Engineering*, 342(1664):209–224, 1993.

[66] J. J. Gracio, Q. H. Fan, and J. C. Madaleno. Diamond growth by chemical vapour deposition. *Journal of Physics D: Applied Physics*, 43(37):374017, Sep 2010.

[67] Yu. A. Mankelevich and P.W. May. New insights into the mechanism of cvd diamond growth: Single crystal diamond in mw pecvd reactors. *Diamond and Related Materials*, 17(7):1021–1028, 2008. Proceedings of Diamond 2007, the 18th European Conference on Diamond, Diamond-Like Materials, Carbon Nanotubes, Nitrides and Silicon Carbide.

[68] Modelling CVD Diamond Growth. http://www.chm.bris.ac.uk/pt/diamond/growthmodel.htm. Accessed: September 28, 2021.

[69] A. M. Edmonds, U. F. S. D'Haenens-Johansson, R. J. Cruddace, and M. E. Newton. Production of oriented nitrogen-vacancy color centers in synthetic diamond. *Phys. Rev. B*, 86:035201, 2012.

[70] M. Pfender, N. Aslam, P. Simon, D. Antonov, G. Thiering, S. Burk, F. Fávaro de Oliveira, A. Denisenko, H. Fedder, J. Meijer, J. A. Garrido, A. Gali, T. Teraji, J. Isoya, M. W. Doherty, A. Alkauskas, A.and Neumann P. Gallo, A.and Grüneis, and J. Wrachtrup. Protecting a diamond quantum memory by charge state control. *Nano Letters*, 17(10):5931–5937, 2017.

[71] C. Schreyvogel, V. Polyakov, S. Burk, H. Fedder, A. Denisenko, F. Fávaro de Oliveira, R. Wunderlich, J. Meijer, V. Zuerbig, J. Wrachtrup, and C. E. Nebel. Active and fast charge-state switching of single nv centres in diamond by in-plane al-schottky junctions. *Beilstein Journal of Nanotechnology*, 7:1727–1735, 2016.

[72] Matthias Pfender, Nabeel Aslam, Patrick Simon, Denis Antonov, Gergö Thiering, Sina Burk, Felipe Fvaro de Oliveira, Andrej Denisenko, Helmut Fedder, Jan Meijer, Jose A. Garrido, Adam Gali, Tokuyuki Teraji, Junichi Isoya, Marcus William Doherty, Audrius Alkauskas, Alejandro Gallo, Andreas Grüneis, Philipp Neumann, and Jrg Wrachtrup. Protecting a Diamond Quantum Memory by Charge State Control. *Nano Letters*, 17(10):5931–5937, 2017.

[73] N. B. Manson, J. P. Harrison, and M. J. Sellars. Nitrogen-vacancy center in diamond: Model of the electronic structure and associated dynamics. *Phys. Rev. B*, 74:104303, Sep 2006.

[74] O. A. Williams, J. Hees, C. Dieker, W. Jaeger, L. Kirste, and C. E. Nebel. Size-Dependent Reactivity of Diamond Nanoparticles. *ACS Nano*, 4(8):4824–4830, 2010.

[75] Carlo Bradac, Torsten Gaebel, Chris. I. Pakes, Jana M. Say, Andrei V. Zvyagin, and James R. Rabeau. Effect of the Nanodiamond Host on a Nitrogen-Vacancy Color-Centre Emission State. *Small*, 9(1):132–139, 2013.

[76] V. V. Danilenko. On the History of the Discovery of Nanodiamond Synthesis. *Physics of the Solid State*, 46(4):595–599, 2004.

[77] Nubuo Setaka and Yoshizo Sekikawa. Diamond synthesis from carbon precursor by explosive shock compression. *Journal of Materials Science*, 16(6):1728–1730, Jun 1981.

[78] V. Yu. Dolmatov. On the mechanism of detonation nanodiamond synthesis. *Journal of Superhard Materials*, 30(4):233–240, Aug 2008.

[79] JB Donnet, C Lemoigne, TK Wang, CM Peng, M Samirant, and A Eckhardt. Detonation and shock synthesis of nanodiamonds. *Bulletin de la Societe Chimique de France*, 134(10-11):875–890, Nov-Dec 1997.

[80] Amanda M. Schrand, Suzanne A. Ciftan Hens, and Olga A. Shenderova. Nanodiamond Particles: Properties and Perspectives for Bioapplications. *Critical Reviews in Solid State and Materials Sciences*, 34(1-2):18–74, 2009.

[81] V. Pichot, M. Comet, E. Fousson, C. Baras, A. Senger, F. Le Normand, and D. Spitzer. An efficient purification method for detonation nanodiamonds. *Diamond and Related Materials*, 17(1):13–22, Jan 2008.

[82] Chapter 3 - Quantum Nanostructures (QDs): An Overview. In Sneha M.B., Oluwatobi S. O., Nandakumar K., and Sabu T., editors, *Synthesis of Inorganic Nanomaterials*, Micro and Nano Technologies, pages 59–88. Woodhead Publishing, 2018.

[83] Tungstennanodiamond composite powders produced by ball milling. *Journal of Nuclear Materials*, 426(1):115–119, 2012.

[84] A. Jankovic. 8 - Developments in iron ore comminution and classification technologies. In Liming Lu, editor, *Iron Ore*, pages 251–282. Woodhead Publishing, 2015.

[85] Chapter 2 - Mechanical Crushing and Grinding. In O.D. Neikov and S.S. Naboychenko and N.A. Yefimov, editor, *Handbook of Non-Ferrous Metal Powders (Second Edition)*, pages 65–90. Elsevier, Oxford, second edition edition, 2019.

[86] I.N. Egorov, S. Santra, D.S. Kopchuk, I.S. Kovalev, G.V. Zyryanov, A. Majee, B. C. Ranu, V.L. Rusinov, and O.N. Chupakhin. Ball milling: an efficient and green approach for asymmetric organic syntheses. *Green Chem.*, 22:302–315, 2020.

[87] A. Bruckmann, A. Krebs, and C. Bolm. Organocatalytic reactions: effects of ball milling, microwave and ultrasound irradiation. *Green Chemistry*, 10:1131–1141, 2008.

[88] C. F. Burmeister and A. Kwade. Process engineering with planetary ball mills. *Chem. Soc. Rev.*, 42:7660–7667, 2013.

[89] C. Suryanarayana, editor. *Non-equilibrium Processing of Materials*. Pergamon, 1999.

[90] M. H. Enayati and F. A. Mohamed. Application of mechanical alloying/milling for synthesis of nanocrystalline and amorphous materials. *International Materials Reviews*, 59(7):394–416, 2014.

[91] P. Chauhan and S.S. Chimni. Mechanochemistry assisted asymmetric organocatalysis: A sustainable approach. *Beilstein Journal of Organic Chemistry*, 8:2132–2141, Dec 2012.

[92] G. Mugunthan and K. P. Ravindranathan Kartha. Application of ball milling technology to carbohydrate reactions-II. Solvent-free mechanochemical synthesis of glycosyl azides. *Journal of Carbohydrate Chemistry*, 27(5):294–299, 2008.

[93] S.Y. Zhao, H.T. Lin, Y.D. Zeng, J.C. Lu, and Z.C. Chang. The optimal mating of balls and lining plates in ball mills. *Wear*, 178(1-2):79–84, Nov 1994.

[94] L. Titscher, S. Breitung-Faes, and A. Kwade. Experimental parameter study on dry crushing in planetary ball mills. *Chemie Ingenieur Technik*, 88(10):1524–1529, 2016.

[95] E. Enqvist, D. Ramanenka, P.A.A.P. Marques, J.Gracio, and N. Emami. The effect of ball milling time and rotational speed on ultra high molecular weight polyethylene reinforced with multiwalled carbon nanotubes. *Polymer Composites*, 37:1128–1136, 2014.

[96] Laia Gines, Soumen Mandal, David John Morgan, Ryan Lewis, Philip R. Davies, Paola Borri, Gavin W. Morley, and Oliver A. Williams. Production of Metal-Free Diamond Nanoparticles. *ACS Omega*, 3(11):16099–16104, NOV 2018.

[97] Jean-Paul Boudou, Patrick A. Curmi, Fedor Jelezko, Joerg Wrachtrup, Pascal Aubert, Mohamed Sennour, Gopalakrischnan Balasubramanian, Rolf Reuter, Alain Thorel, and Eric Gaffet. High yield fabrication of fluorescent nanodiamonds. *Nanotechnology*, 20(23), JUN 10 2009.

[98] Jiabao Zheng, Benjamin Lienhard, Gregory Doerk, Mircea Cotlet, Eric Bersin, Harrison Sejoon Kim, Young-Chul Byun, Chang-Yong Nam, Jiyoung Kim, Charles T. Black, and Dirk Englund. Top-down fabrication of high-uniformity nanodiamonds by self-assembled block copolymer masks. *Scientific Reports*, 9, 2019.

[99] Fabrication of diamond nanopillars and their arrays. *Applied Physics Letters*, 92, 2008.

[100] Paolo Andrich, Benjamn J. Alemn, Jonathan C. Lee, Kenichi Ohno, Charles F. de las Casas, F. Joseph Heremans, Evelyn L. Hu, and David D. Awschalom. Engineered micro- and nanoscale diamonds as mobile probes for high-resolution sensing in fluid. *Nano Letters*, 14(9):4959–4964, 2014.

[101] Matthew E. Trusheim, Luozhou Li, Abdelghani Laraoui, Edward H. Chen, Hassaram Bakhru, Tim Schroeder, Ophir Gaathon, Carlos A. Meriles, and Dirk Englund. Scalable Fabrication of High Purity Diamond Nanocrystals with Long-Spin-Coherence Nitrogen Vacancy Centers. *Nano Letters*, 14(1):32–36, Jan 2014.

[102] A. E. Aleksenskiy, E. D. Eydelman, and A. Ya Vul'. Deagglomeration of Detonation Nanodiamonds. *Nanoscience and Nanotechnology Letters*, 3(1, SI):68–74, Feb 2011.

[103] Pavla Stenclova, Vladyslava Celedova, Anna Artemenko, Vit Jirasek, Jaroslav Jira, Bohuslav Rezek, and Alexander Kromka. Surface chemistry of water-dispersed detonation nanodiamonds modified by atmospheric DC plasma afterglow. *RSC Advances*, 7(62):38973–38980, 2017.

[104] Karen M. McNamara. Aggregate nitrogen in synthetic diamond. *Applied Physics Letters*, 87(7):1325, 2003.

[105] M. Lobaev, A Gorbachev, Sergey Bogdanov, A Vikharev, Dmitry Radishev, Valerii Chernov, and M Drozdov. Influence of CVD diamond growth conditions on nitrogen incorporation. *Diamond and Related Materials*, 72:1–6, Jan 2017.

[106] A. M. Edmonds, U. F. S. D'Haenens-Johansson, R. J. Cruddace, Mark E. Newton, K.-M. C. Fu, C. Santori, R. G. Beausoleil, D. J. Twitchen, and M. L. Markham. Production of oriented nitrogen-vacancy color centers in synthetic diamond. *Physical Review B*, Vol.86(No.3):Article no. 035201, 2012.

[107] C. C. Battaile, D. J. Srolovitz, and J. E. Butler. Point defect incorporation during diamond chemical vapor deposition. *Journal of Materials Research*, 14(8):34393446, 1999.

[108] D. J. Twitchen, M. E. Newton, J. M. Baker, T. R. Anthony, and W. F. Banholzer. Electron-paramagnetic-resonance measurements on the divacancy defect center $r4/w6$ in diamond. *Phys. Rev. B*, 59:12900–12910, May 1999.

[109] I. Kiflawi, A. T. Collins, K. Iakoubovskii, and D. Fisher. Electron irradiation and the formation of vacancy–interstitial pairs in diamond. *Journal of Physics: Condensed Matter*, 19(4):046216, Jan 2007.

[110] M. Capelli, A.H. Heffernan, T. Ohshima, H. Abe, J. Jeske, A. Hope, A.D. Greentree, P. Reineck, and B.C. Gibson. Increased nitrogen-vacancy centre creation yield in diamond through electron beam irradiation at high temperature. *Carbon*, 143:714 – 719, 2019.

[111] C. A. McLellan, B. A. Myers, S. Kraemer, K. Ohno, D. D. Awschalom, and A. C. Bleszynski Jayich. Patterned Formation of Highly Coherent Nitrogen-Vacancy Centers Using a Focused Electron Irradiation Technique. *Nano Letters*.

[112] B. Campbell and A. Mainwood. Radiation Damage of Diamond by Electron and Gamma Irradiation. *Physica Solidus Solidi (a)*, 181(1):99–107, 2000.

[113] A. Edmunds. *Magnetic resonance studies of point defects in single crystal diamond*. PhD thesis, University of Warwick, 7 2008.

[114] J Schwartz, S Aloni, D F Ogletree, and T Schenkel. Effects of low-energy electron irradiation on formation of nitrogen–vacancy centers in single-crystal diamond. *New Journal of Physics*, 14(4):043024, apr 2012.

[115] S Lawson, G Davies, A T Collins, and A Mainwood. Migration energy of the neutral vacancy in diamond. *Journal of Physics: Condensed Matter*, 4(9):L125–L131, mar 1992.

[116] Y. Chu, N. P. de Leon, B. J. Shields, B. Hausmann, R. Evans, E. Togan, M. J. Burek, M. Markham, A. Stacey, A. S. Zibrov, A. Yacoby, D. J. Twitchen, M. Loncar, H. Park, P. Maletinsky, and M. D. Lukin. Coherent Optical Transitions in Implanted Nitrogen Vacancy Centers. *Nano Letters*, 14(4):1982–1986, Apr 2014.

[117] A. V. Khomich, M. V. Kanzyuba, I. I. Vlasov, V. G. Ral'chenko, and N. I. Gorbachuk. Optical Spectroscopy of the Surface of Nanoporous Diamond Films. *Journal of Applied Spectroscopy*, 78(4):563–571, Sep 2011.

[118] K. M. O'Donnell, T. L. Martin, N. A. Fox, and D. Cherns. Ab initio investigation of lithium in the diamond C(100) surface. *Physical Review B*, 82:115303, 2010.

[119] J. Navas, D. Araujo, J. C. Piñero, A. Sánchez-Coronilla, E. Blanco, P. Villar, R. Alcántara, J. Montserrat, M. Florentin, D. Eon, and J. Pernot. Oxygentermination of homoepitaxial diamond surface by ozone and chemical methods: An

experimental and theoretical perspective. *Applied Surface Science*, 433:408–418, 2018.

[120] J. Niedziolka-Joensson, S. Boland, D. Leech, R. Boukherroub, and S. Szunerits. Preparation and reactivity of carboxylic acid-terminated boron-doped diamond electrodes. *Electrochemica Acta*, 55(3):959–964, Jan 1 2010.

[121] V.L. Kuznetsov and Yu.V. Butenko. Nanodiamond graphitization and properties of onion-like carbon. In Dieter M. Gruen, Olga A. Shenderova, and Alexander Ya. Vul', editors, *Synthesis, Properties and Applications of Ultrananocrystalline Diamond*, pages 199–216, Dordrecht, 2005. Springer Netherlands.

[122] Lu-Chang Qin and Sumio Iijima. Onion-like graphitic particles produced from diamond. *Chemical Physics Letters*, 262(3):252 – 258, 1996.

[123] Sebastian Osswald, Gleb Yushin, Vadym Mochalin, Sergei O. Kucheyev, and Yury Gogotsi. Control of sp^2/sp^3 Carbon Ratio and Surface Chemistry of Nanodiamond Powders by Selective Oxidation in Air. *J. Am. Chem. Soc.*, 128(35):11635–11642, 2006.

[124] Anke Krueger and Daniel Lang. Functionality is key: Recent progress in the surface modification of nanodiamond. *Advanced Functional Materials*, 22(5):890–906, 2012.

[125] T. Ando, M. Ishii, M. Kamo, and Y. Sato. Thermal hydrogenation of diamond surfaces studied by diffuse reflectance fourier-transform infrared, temperature-programmed desorption and laser raman spectroscopy. *Journal of the Chemical Society, Faraday Transactions*, 89(11):1783–1789, 1993.

[126] B. V. Spitsyn, S. A. Denisov, N. A. Skorik, A. G. Chopurova, S. A. Parkaeva, L. D. Belyakova, and O. G. Larionov. The physical-chemical study of detonation nanodiamond application in adsorption and chromatography. *Diamond and Related Materials*, 19:123127, 2010.

[127] S. Ida, T. Tsubota, O. Hirabayashi, M. Nagata, Y. Matsumoto, and A. Fujishima. Chemical reaction of hydrogenated diamond surface with peroxide radical initiators. *Diamond and Related Materials*, 12:601605, 2003.

[128] A. T. M. A. Rahman, A. C. Frangeskou, M. S. Kim, S. Bose, G. W. Morley, and P. F. Barker. Burning and graphitization of optically levitated nanodiamonds in vacuum. *Scientific Reports*, 6:21633, 2016.

[129] ZJ Qiao, JJ Li, NQ Zhao, CS Shi, and P Nash. Graphitization and microstructure transformation of nanodiamond to onion-like carbon. *Scripta Materiala*, 54(2):225–229, Jan 2006.

[130] Alastair Stacey, Kane M. ODonnell, Jyh-Pin Chou, Alex Schenk, Anton Tadich, Nikolai Dontschuk, Jiri Cervenka, Chris Pakes, Adam Gali, Alon Hoffman, and Steven Prawer. Nitrogen terminated diamond. *Advanced Materials Interfaces*, 2:1500079, 2015.

[131] Jyh-Pin Chou, Alex Retzker, and Adam Gali. Nitrogen-terminated diamond (111) surface for room-temperature quantum sensing and simulation. *Nano Letters*, 17(4):2294–2298, 2017.

[132] S. Kawai, H. Yamano, T. Sonoda, K. Kato, J. J. Buendia, T. Kageura, R. Fukuda, T. Okada, T. Tanii, T. Higuchi, M. Haruyama, K. Yamada, S. Onoda, T. Ohshima, W. Kada, O. Hanaizumi, A. Stacey, T. Teraji, S. Kono, J. Isoya, and H. Kawarada. Nitrogen-terminated diamond surface for nanoscale nmr by shallow nitrogen-vacancy centers. *The Journal of Physical Chemistry C*, 123(6):3594–3604, 2019.

[133] T. Nakamura, T. Ohana, Y. Hagiwara, and T Tsubota. Photochemical modification of diamond powders with elemental sulfur and their surface-attachment behavior on gold surfaces. *Phys. Chem. Chem. Phys.*, 11(4):730–734, 2009.

[134] Siheng Su, Junhua Wei, Kun Zhang, Jingjing Qiu, and Shiren Wang. Thermo- and ph-responsive fluorescence behaviors of sulfur-functionalized detonation nanodiamond-poly(n-isopropylacrylamide). *Colloid and Polymer Science*, 293(4):1299–1305, 2015.

[135] Yu Liu, Zhenning Gu, John L. Margrave, and Valery N. Khabashesku. Functionalization of Nanoscale Diamond Powder: Fluoro-, Alkyl-, Amino- and Amino Acid-Nanodiamond Derivatives. *Chemistry of Materials*, 16(20):3924–3930, 2004.

[136] M.A. Ray, T. Tyler, B. Hook, A. Martin, G. Cunningham, O. Shenderova, J.L. Davidson, M. Howell, W.P. Kang, and G. McGuire. Cool plasma functionalization of nano-crystalline diamond films. *Diamond and Related Materials*, 16(12):2087 – 2089, 2007.

[137] A.P. Nizovtsev, S.Y. Kilin, F. Jelezko, I. Popa, A. Gruber, and J. Wrachtrup. NV centers in diamond: spin-selective photokinetics, optical ground-state spin alignment and hole burning. *Physica B - Condensed Matter*, 340:106–110, 2003.

[138] G.D. Farquhar, J.R. Ehleringer, and K.T. Hubick. Carbon Isotope Discrimination and Photosynthesis. *Annual Review of Plant Physiology and Plant Molecular Biology*, 40:503–537, 1989.

[139] J. R. Ehleringer and P. W. Rundel. Stable Isotopes: History, Units, and Instrumentation. In P. W. Rundel, J. R. Ehleringer, and K. A. Nagy, editors, *Stable Isotopes in Ecological Research*, pages 1–15, New York, NY, 1989. Springer New York.

[140] Gopalakrishnan Balasubramanian, Philipp Neumann, Daniel Twitchen, Matthew Markham, Roman Kolesov, Norikazu Mizuochi, Junichi Isoya, Jocelyn Achard, Johannes Beck, Julia Tissler, Vincent Jacques, Philip R. Hemmer, Fedor Jelezko, and Jörg Wrachtrup. Ultralong spin coherence time in isotopically engineered diamond. *Nature Materials*, 8:383–387, 2009.

[141] R. Samlenski, C. Haug, and R. Brenn. Incorporation of nitrogen in chemical vapor deposition diamond. *Applied Physics Letters*, 67(19):2798, 1995.

Chapter 5

Electron Paramagnetic Resonance

5.1 Spin dynamics

Spin is a quantum number describing the intrinsic angular momentum of a given particle which can take either half-integer or integer values. Those particles exhibiting integer spin are known as bosons, whilst fermions have half-integer spin.

The spin of a particle, can be considered as a magnetic dipole. Interaction between spins and magnetic fields leads to both nuclear magnetic resonance (NMR) and electron paramagnetic resonance (EPR).

5.1.1 The spin Hamiltonian

The electron spin Hamiltonian describes the interaction energy of the spin system in distinct terms including the electronic Zeeman interaction, the zero-field splitting (ZFS), the hyperfine and quadrupole interactions and a nuclear Zeeman term along with higher order terms not covered here..

$$H = \underbrace{\mu_B \underline{B}^T \cdot \underline{g} \cdot S}_{\text{Electronic Zeeman}} + \overbrace{S^T \cdot \underline{D} \cdot S}^{\text{Zero-field}} + \underbrace{\sum_i S^T \cdot \underline{A_i} \cdot I_i}_{\text{Hyperfine}} + \overbrace{\sum_i I_i^T \cdot \underline{P_i} \cdot I_i}^{\text{Quadrupole}} - \underbrace{\sum_i g_N \mu_N B^T \cdot I_i}_{\text{Nuclear Zeeman}} + \ldots \tag{5.1}$$

Equation 5.1 describes the spin Hamiltonian[1, 2] of an electron where the terms are as follows:

μ_B: the Bohr magneton ($9.274\,009\,994 \times 10^{-24}\,\mathrm{J \cdot T^{-1}}$)
μ_N: the nuclear magneton ($5.050\,783\,699 \times 10^{-27}\,\mathrm{J \cdot T^{-1}}$)
$\underline{B}^T$: the transpose of the magnetic field vector
$\underline{g}$: the electronic g-factor matrix
g_N: the nuclear g-factor
$\underline{D}$: the zero-field matrix
$\underline{A}$: the hyperfine tensor
$\underline{P}$: the nuclear quadrupole coupling matrix
$\underline{S}$: the electron spin operator

I: the nuclear spin operator
i: number of nuclear spins present

These interactions can each cause 'splitting' of the energy levels which can be observed as the division (or splitting) of resonant lines in paramagnetic resonance techniques.

5.1.2 Electronic Zeeman splitting

The electronic Zeeman term is written as:

$$H_{EZ} = \mu_B B^T \cdot \underline{g} \cdot S \tag{5.2}$$

The Bohr magneton, $\mu_B = \frac{e\hbar}{2m_e}$, where $e \approx 1.6 \times 10^{-19}$ C is the elementary charge, $\hbar$ is the modified Planck constant and m_e is the rest mass of an electron, is defined as the natural unit of the magnetic moment of an electron imparted by either orbital or spin angular momentum. The electronic g-factor matrix, $\underline{g}$ contains information about the environment surrounding the unpaired electron. For a single electron[3] in free space $g_e \approx 2.0023$.

The Zeeman term is typically the largest term in the Hamiltonian for $B_0 > 0.3$ T, common in EPR. The term occurs solely as an interaction between unpaired electrons and the external magnetic field. Due to the quantisation of energy, an unpaired electron may exist in one of two states (or as a superposition of those states), either parallel (lower energy) or anti-parallel (higher energy) to the magnetic field.[4] The difference in the energies of these two states, $\Delta E = h\nu$ provides a condition for an EPR transition to occur[5] (where $\Delta m_s = \pm 1$):

$$h\nu = g_e \mu_B B \tag{5.3}$$

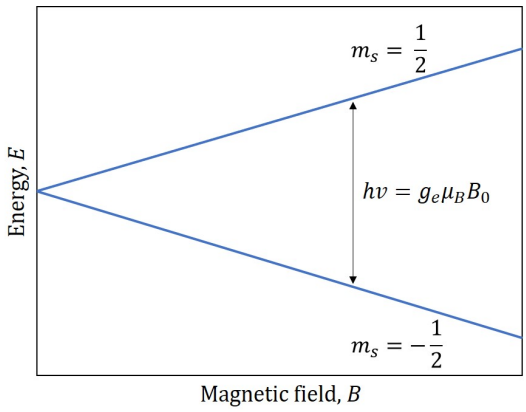

Figure 5.1: Illustration of the splitting of energies in a lone, unpaired electron under the influence of a magnetic field, where B_0 is the applied magnetic field in EPR.

for an isotropic $\underline{g}$ with magnitude g_e which allows for the measurement of an applied magnetic field (where h is the Planck constant and ν is the frequency of resonant excitation - see section 5.2). Equation 5.3 can be written as:

$$\Delta E = \gamma B \tag{5.4}$$

where $\gamma = g_e\mu_B$ is the gyromagnetic ratio and $\gamma = 28\,\mathrm{GHz/T}$ for $g_e \approx 2$ as with the NV centre.

From equation 5.3 is becomes apparent that under an applied magnetic field $B_0 = 0\,\mathrm{T}$ (in practical EPR, the static applied field is commonly referred to as B_0), the difference in energy between the parallel and anti-parallel states is also zero, meaning that these states are degenerate, with no way to differentiate between the two (in the absence of other forms of splitting - see below). Similarly, it should be noted that the equation also predicts a linear relationship between the magnetic field and the resultant splitting of energies (see figure 5.1).

5.1.3 Zero-field splitting

Independently of an applied magnetic field, zero field splitting (ZFS) occurs in a spin system with non-cubic symmetry and $S > 1/2$. Arising from electron-electron dipolar interactions or spin-orbit coupling, the ZFS term can be extracted from equation 5.1:

$$H_{ZFS} = \tilde{S}\mathbf{D}S \tag{5.5}$$

(where $\mathbf{D}$ is the zero field interaction tensor) and can be expanded to:[6]

$$H_{ZFS} = D_x S_x^2 + D_y S_y^2 + D_z S_z^2 \tag{5.6}$$

$$H_{ZFS} = D\left(S_z^2 - \frac{(S(S+1))}{3}\right) + E(S_x^2 - S_y^2) \tag{5.7}$$

where S_x, S_y and S_z are spin matrices and $D = {}^{3D_z}/_{2}$ and $E = {}^{(D_x - D_y)}/_{2}$.

5.1.4 Hyperfine interactions

Hyperfine splitting stems from the magnetic interaction between an electron spin and nuclear spins in the environment. As such it can be used to probe the region immediately surrounding the electron(s). For hyperfine interactions to occur, the nuclei must possess net nuclear spin.

The hyperfine interaction:[7]

$$H_{HF} = \underline{S}^T \cdot \underline{\underline{A_i}} \cdot \underline{I_i} \tag{5.8}$$

is comprised of the system's electron spin, its nuclear spin and the hyperfine tensor $\underline{A}$ which is expressible as the sum of the isotropic contact interaction H_F and the electron nuclear dipole-dipole coupling[2] H_{DD}, where

$$H_F = a_{iso}\underline{S} \cdot \underline{I} \tag{5.9}$$

and

$$a_{iso} = \frac{2}{3}\frac{\mu_0}{\hbar} g_e \mu_B g_N \mu_N \rho_e \tag{5.10}$$

where $\rho_e = |\psi_0(0)|^2$ is the electron spin density as measured at the nucleus. Meanwhile, the electron-nuclear dipole-dipole coupling is:

$$H_{DD} = \frac{\mu_0}{4\pi\hbar} g_e \mu_B g_N \mu_N \left[\frac{(3\underline{S} \cdot \underline{r})(\underline{r} \cdot \underline{I})}{r^5} - \frac{\underline{S} \cdot \underline{I}}{r^3} \right] \tag{5.11}$$

where $\underline{r}$ is a vector describing the relative position of the electron and nucleus, and this must be calculated over the unpaired electron distribution.

5.1.5 Quadrupole interactions

Where nuclei possess a non-spherical charge distribution, i.e. in cases where the nuclear spin I is unity or greater, they have a nuclear electrical quadrupole moment Q.[2] This non-spherical charge interacts with the electric field gradient. This interaction leads to changes to resonant frequencies and the manifestation of forbidden transitions in EPR spectra.

5.1.6 Nuclear Zeeman splitting

Similarly to coupling between an electron and an external magnetic field, the nuclear Zeeman interaction sees the interplay between the nuclear spin $\underline{I}$ and the field $\underline{B_0}$ resulting in the following:[8]

$$H_{NZ} = -g_N \mu_N \underline{B}_0 \underline{I} \tag{5.12}$$

The nuclear Zeeman interaction is far weaker than the electronic Zeeman and, in EPR, is usually isotropic.[2] This may present as small shifts of resonances or "forbidden" satellite lines under specific conditions.

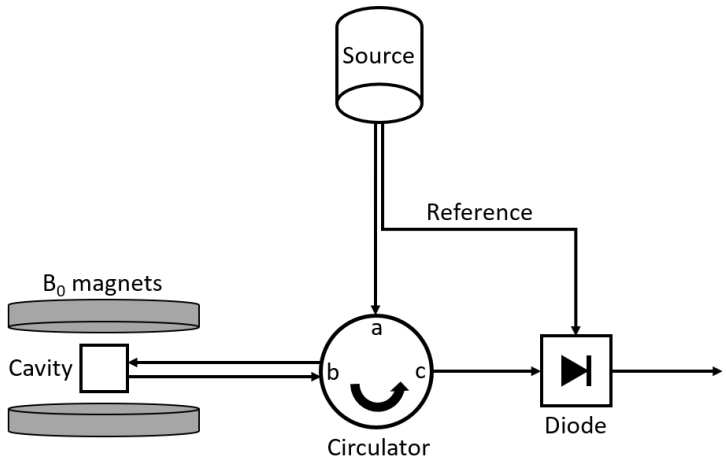

Figure 5.2: Functional layout of an EPR spectrometer. Microwave emission from the source enters the circulator at 'a' and exits *only* at 'b', after which it enters the cavity and interacts with the sample. The resultant emission from the cavity returns to the circulator at 'b' and exits *only* at 'c'. The difference between the reference and the signal exiting the circulator forms the output signal, constructed by a detector diode.

5.2 Practical EPR

To observe the phenomena discussed in section 5.1 in the laboratory, transitions between states must be effected by the application of resonant excitation in the form of photons. For the NV^- defect in diamond (see section 4.4, $g = 2.0028$[9]), this takes the form of microwaves at a frequency of around 2.88 GHz in the absence of an applied magnetic field.

5.2.1 The EPR spectrometer

An EPR spectrometer consists of four major components - a magnet, a microwave bridge, a cavity and a detector (see figure 5.2). The microwave bridge is comprised of a source (microwave generator) and a circulator, which separates the input microwaves from the signal returning from the cavity. The detector is usually included in the microwave bridge.

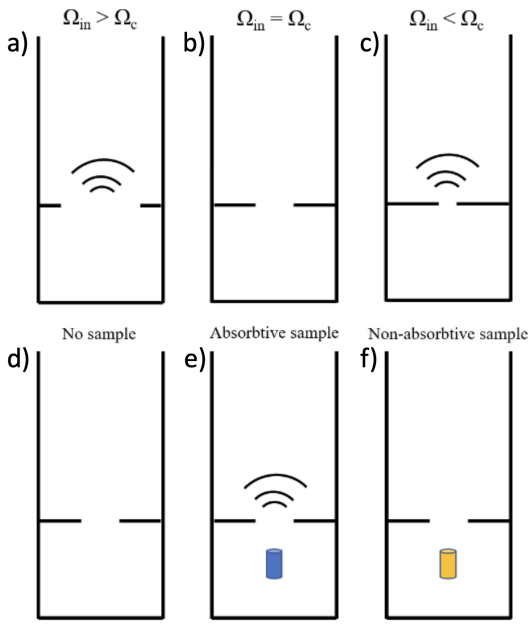

Figure 5.3: Behaviour of an EPR cavity under various conditions. An unloaded cavity will reflect microwave radiation when not critically coupled (a, c), i.e. the iris is either too large or too small. An unloaded and critically coupled cavity (b), an unloaded and non-critically coupled cavity (d) or a cavity containing a non-absorptive sample (f) will not reflect microwaves. A loaded (and critically coupled) cavity will only reflect microwaves, and therefore generate a signal, when a sample which absorbs at the resonant frequency is present (e).

The cavity must be tuned to the microwave frequency and impedance matched by the use of an iris (which adjusts the ratio between microwaves passed through it and microwaves reflected back away from the cavity by changing the width of the aperture into the cavity), so that when 'critically coupled' and without the presence of a resonant sample, no microwaves are reflected back from the cavity to the detector (see fig. 5.3). Where either the cavity is not critically coupled (when the iris is too wide/narrow) or there is a sample which is able to absorb incoming radiation through excited magnetic dipole interactions, microwave energy will be reflected by the cavity to produce a signal.

In conventional continuous wave (CW) EPR, typically the magnetic field

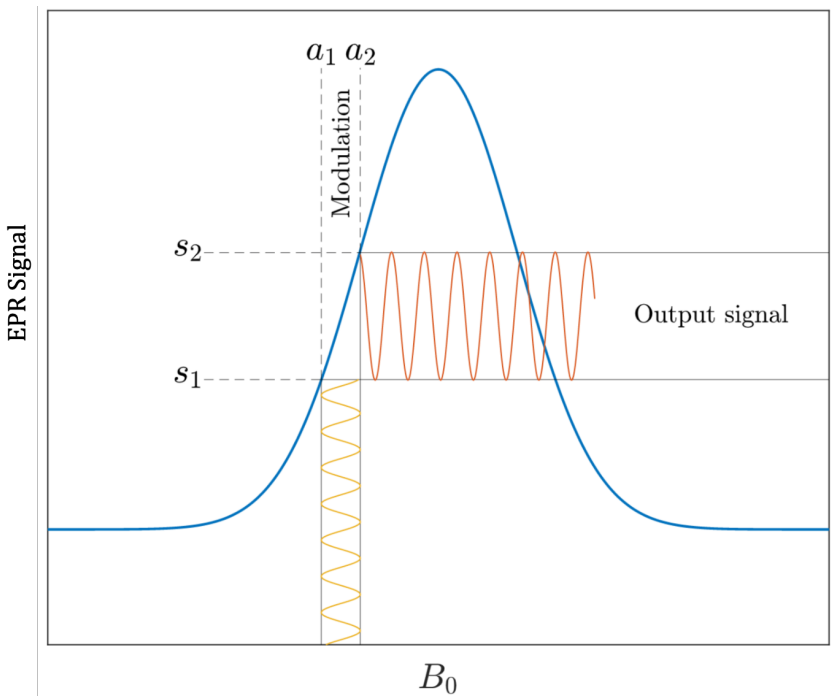

Figure 5.4: As the B_0 field is swept, absorption occurs where the magnitude of the field matches the microwave excitation frequency (see eqn. 5.3). A second, oscillating field is applied parallel to B_0 to which a lock-in amplifier is tuned. This modulation scans a small region of the total scanning range at any one time, giving an output signal at the upper extent of the modulation amplitude (a_1) and and an output signal at the lower extent (a_2), leading to the respective outputs s_1 and s_2. The LIA output represents the difference in these values for each 'segment' (modulation amplitude) of the sweep range, leading to the derivative line shape seen in figure 5.5.

B_0 is swept. Where $|B_0|$ matches the value of the microwave frequency ν with respect to equation 5.3, a microwave photon may be absorbed, causing a transition between the two electronic spin states. Resonant lines therefore appear as changes in the absorption and dispersion of microwave photons by the sample leading to an increase in the microwave power reflected back from the cavity to the detector. As the signal may be extremely weak and/or noisy, an LIA (lock-in amplifier, see section 2.2) is usually employed, leading to a derivative line shape (figures 5.4 and 5.5) as the change in absorption across the amplitude of the LIA's modulation.

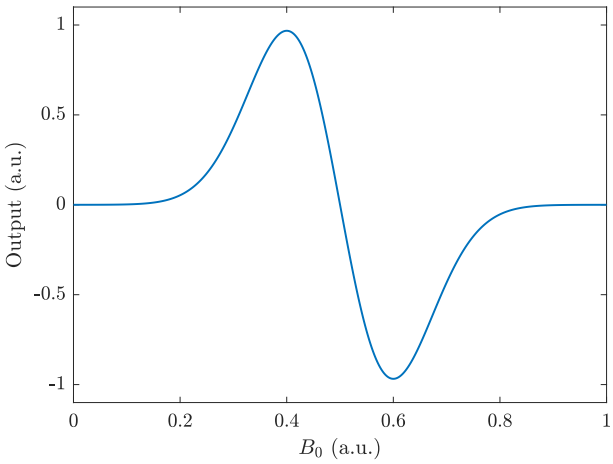

Figure 5.5: Derivative line shape produced by employing a lock-in amplifier to demodulate an EPR signal.

The derivative line shape is a result of modulation of the B_0 field and subsequent demodulation by the LIA. As the field is oscillating between two values during a modulation cycle, the output will oscillate accordingly, with one extent of the modulation producing a higher value than the other when the sweep encounters a resonant feature.

5.2.2 Optically detected magnetic resonance

The energy level structure of the NV$^-$ (see figure 5.6) allows for the spin polarisation of the centre by irradiation with green light at e.g. 532 nm. Absorption at this wavelength excites the centre from the ^3A triplet ground state to the ^3E triplet excited state in a spin-conserving transition. Relaxation from the excited states is spin state dependent. From the $m_s = 0$ state there is a high probability of relaxation via the emission of a 637 nm or longer wavelength photon, with this transition referred to as "bright". From the $m_s = \pm 1$ state, there is a high probability of intersystem crossing (ISC - see fig. 5.6) and the emission of of an infrared photon or a non-radiative transition between the $^1A_1$ and $^1E_1$ states, and the subsequent relaxation back to the $m_s = 0$ ground state, termed the "dark" transition. This

results in efficient spin polarisation into the $m_s = 0$ state.

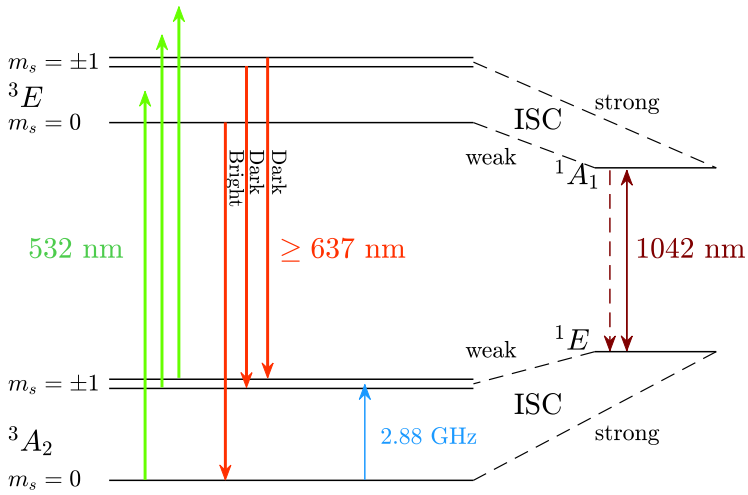

Figure 5.6: The energy level scheme of the negatively charged nitrogen vacancy centre. Spin conserving optical excitation of the ^{3}A$_2$ triplet ground state[10] to the excited ^{3}E state leads to relaxation via a red photon (λ_{re}) or spin polarisation to the $m_s = 0$ ground state via inter-system crossing (ISC) and non-radiative relaxation (or the emission of an infrared photon (λ_{ir})) between the singlet states. Resonant microwave excitation can then excite from the $m_s = 0$ ground state to the degenerate $m_s = \pm 1$ ground state. This degeneracy may be lifted by the application of a magnetic field by Zeeman splitting (see section 5.1.2). 'Weak' and 'strong' refer to the relative probability of centres making the transition from either the $m_s = 0$ or $m_s = \pm 1$ excited state through the shelving states. With the spin selective transition from the ^3E level to the $^1A_1$ level, approximately 99% of transitions will be via the 'strong' route, coming from the $m_s = \pm 1$ state and the remaining 1% from the $m_s = 0$ state.

After polarisation (or 'initialisation' into the $m_s = 0$ ground state), the centre may then be raised from the $m_s = 0$ ground state to the $m_s = \pm 1$ ground state by the absorption of a microwave photon (magnetic dipole transition) of a specific resonant frequency according to equation 5.3. This reduces the red fluorescence enabling ODMR detection of the transition. The application of a magnetic field then leads to Zeeman splitting of the ± 1 states. If the microwave field is swept

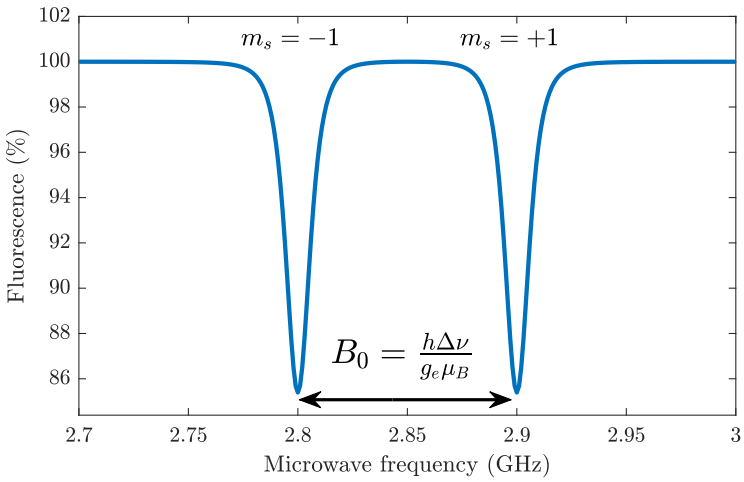

Figure 5.7: A sketch of the NV$^-$ ODMR spectrum. Each trough in fluorescence represents a formerly degenerate state in the presence of a magnetic field, calculable from equation 5.3. Note that this drawing does not take account of a lock-in amplifier, and so the features are purely absorptive and have no derivative line shape.

under these conditions, a reduction of the red fluorescence will be detected at specific frequencies.

Fluorescence collection efficiency in ODMR

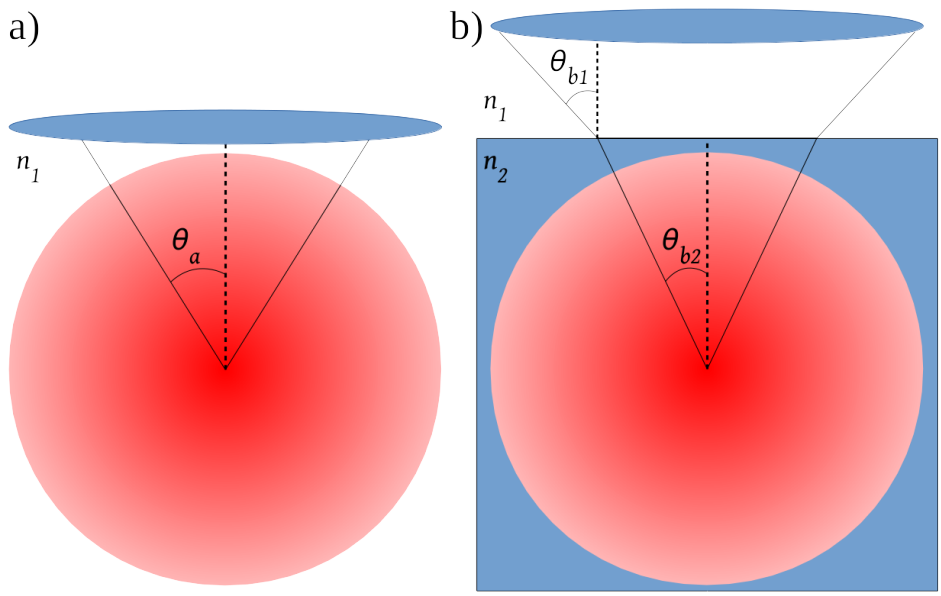

Figure 5.8: Two dimensional model of the collection efficiency of a lens collecting light from an isotropic source in a) a single medium of refractive index n_1 and b) two materials of refractive indices n_1 and n_2.

The amount of light collected from an emitter at the focus of a lens can be defined by a cone whose section inscribes the angle 2θ, where θ is the angle between the exterior face of the cone and the line normal to the base of the cone (see figure 5.8). This angle is in turn defined by the lens' numerical aperture (NA) as:

$$NA = n \sin\theta \tag{5.13}$$

where n is the refractive index of the medium through which the collected light travels before reaching the lens. Where two refractive indices are present, as shown in figure 5.8b:

$$NA = n_1 \sin\theta_{b1} = n_2 \sin\theta_{b2} \tag{5.14}$$

This collection efficiency becomes significant when employing ODMR practically and is discussed further in chapter 6.

5.3 Pulsed ODMR

5.3.1 The Bloch interpretation

Any two level quantum system can be illustrated by a 'Bloch sphere', a pictographic representation of that system (see figure 5.9). The poles of the sphere represent the two levels ('basis states'), with the equator of the sphere representing an equal superposition of the two states. Partial superpositions are represented by all other surface positions, and mixed states are represented by points within the sphere beneath the surface.

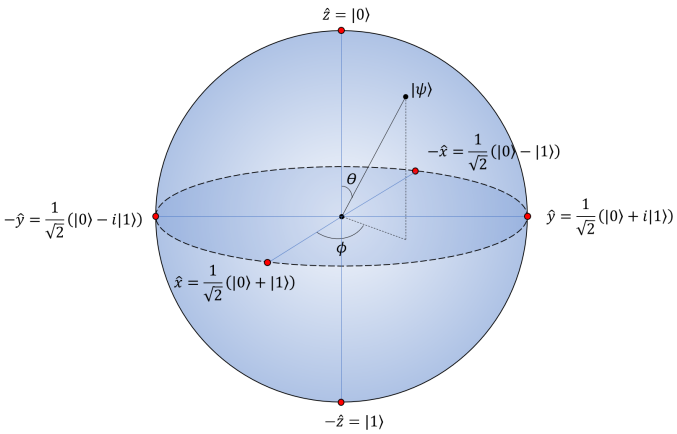

Figure 5.9: Bloch sphere for a non-specific two level system. Vectors at either pole are basis states, with other points on the sphere's surface corresponding to superpositions of the two basis states. Mixed states can be represented by vectors which terminate below the sphere's surface.

A vector joining any of these points with the sphere's centre then represents the state of the two-level system in its entirety. For the NV^- centre spin, the state vector $|\psi\rangle$ is also rapidly rotating in the laboratory reference frame, and so the

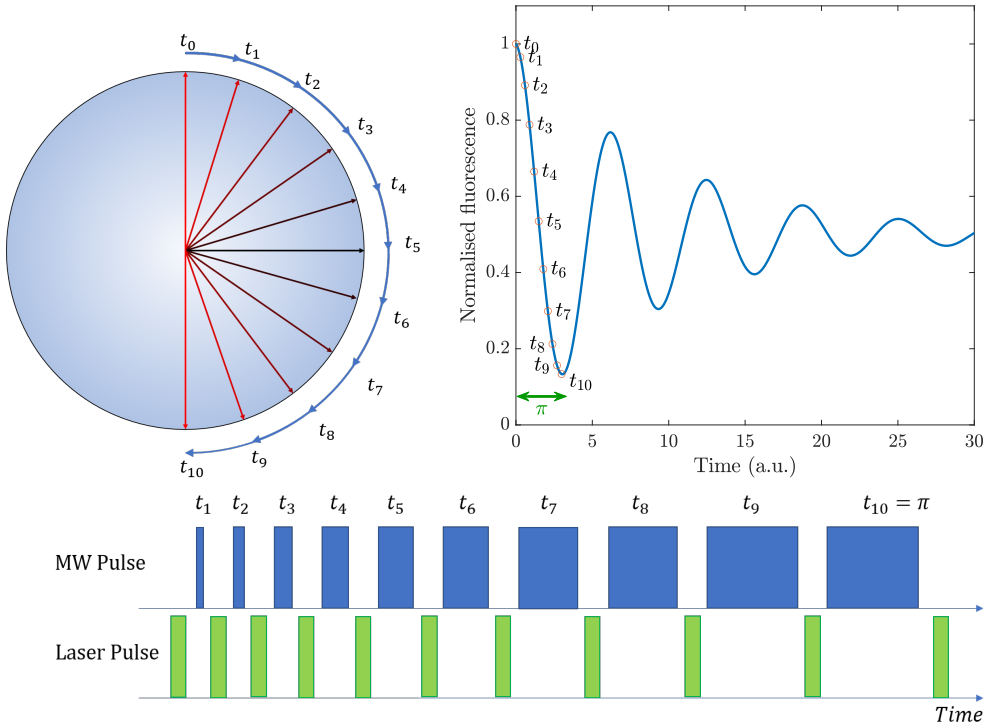

Figure 5.10: A two dimensional Bloch sphere representation of a Rabi oscillation sequence (left) with the resulting fluorescence as a function of pulse area (right). Each state or superposition has a characteristic fluorescence which is plotted against the length of the microwave pulse used to initialise that state or superposition. Below are the microwave and laser pulse sequences used for spin initialisation and read out.

Bloch sphere interpretation breaks down. However, if a rotating reference frame is used, the vector remains stationary. For the remainder of this thesis, the rotating reference frame will be assumed unless otherwise stated.

5.3.2 Rabi oscillations

Using the microwave transition illustrated in figures 5.6 and 5.7, the state of the NV$^-$ may be driven from $m_s = 0$ to $m_s = \pm 1$, and its change in fluorescence observed in order to read out the state (see figure 5.10). The length of pulse necessary to drive the spin between these states, identified by the time between the initial fluorescence

maximum and the subsequent minimum, is half the Rabi period and is the length of the π-pulse, which will be used for other pulse sequences as it measures the length of the pulse necessary to place the spin in a particular state or superposition.

5.3.3 Decoherence

Once a system is placed into a superposition of two states $|1\rangle$ and $|2\rangle$, this superposition cannot remain coherent indefinitely and is time dependent:

$$|Q,t\rangle = e^{-i\omega_1 t}\left(\alpha\,|1\rangle + \beta e^{i\varphi} e^{-i\omega_0 t}\,|2\rangle\right) \tag{5.15}$$

where $\omega_1 t$ is an non-measurable global phase, φ is the initial relative phase and the acquired relative phase is $\omega_0 t$, where $\omega_0 t$ can change with time. If $\omega_0 t$ is known, then quantum information can be preserved, otherwise various random interactions result in a fluctuation of the energy difference between the spin up and spin down states, $E_0 = \hbar\omega_0$ over time. At a later time, t', equation 5.15 then becomes:

$$\left|Q',t\right\rangle = \alpha\,|1\rangle + \beta e^{i\varphi} e^{-i\omega_0 t} e^{-i\delta}\,|2\rangle \tag{5.16}$$

where the accumulated phase:

$$\delta = \frac{1}{\hbar}\int_0^{t'} \delta E_0\,(dt) \tag{5.17}$$

is unknown. These fluctuations lead to the gradual decoherence of the superposition and the state becoming mixed rather than purely coherent. In the Bloch interpretation this is represented by a shortening of the $|\psi\rangle$ state vector. Such mixed states require the use of density matrices which are not covered here.

Spin-lattice decoherence

Through phononic interactions, the magnetisation vector of an NV^- centre parallel to the background magnetic field may reach thermal equilibrium with the lattice of the diamond. This phenomenon is known as spin-lattice relaxation, and the length of time for this to occur after the initialisation of a spin state is known as the T_1 time.

Free induction decay

Free induction decay (FID) is the pulsed EPR signal generated by electron spin magnetisation precessing about the magnetic field after a pulse that is not a π pulse. A $\pi/2$ pulse is chosen to maximise the FID. The timescale for this decay is T_2^* which is generally dominated by the inhomogeneous dephasing but also includes the homogeneous dephasing and the spin lattice decay. To observe FID using ODMR a $\pi/2$ pulse is used. For the case of repeated measurements of a single spin, this inhomogeneous decoherence occurs to changing environmental factors such as the local strain field or electric and magnetic fields in between measurements. In the case of multiple spins, these factors may vary between the locations of the individual spins, again leading to an inhomogeneous environment and resulting decoherence.

Spin-spin decoherence

To consider an isolated spin is, in most cases, unrealistic. In truth, most spins are surrounded by other spins, whether nuclear or electronic, with which they will interact. The relaxation of the transverse component of the magnetisation vector towards its equilibrium, which can be caused by these neighbouring spins, is called spin-spin decoherence and is referred to as the T_2 coherence time. As the length of the T_2 is dependent on the number of spins in the environment, it is sometimes the

case that:

$$T_2 \propto \frac{1}{n_s} \tag{5.18}$$

where n_s is the local number density of spins.[11]

Importantly, these neighbouring spins may be either a part of the lattice in the form of substitutional nitrogen ($N_S{}^0$), carbon-13 (^{13}C) or other dopants, or they may take the form of surface level spins. In nanodiamond, where surfaces are a significant proportion of the material by number of atoms, these surface defects become significant, with smaller nanodiamonds seeing changes to the material's band gap,[12] and size may affect wavelength dependent fluorescence and total fluorescence.[13, 14] The reason behind these effects is that as nanodiamond diameter decreases, the proportion of the particle's mass occupied by the surface increases, and therefore the proportion of the particle's mass composed of surface spins increases. Moreover, decreasing particle diameter leads to decreased separation between NV defects and these surface spins. It is not unreasonable then to suspect that, due to the decoherence processes described in section 5.3.3 decreased T_2 times are expected to be observed in smaller nanodiamonds.

5.3.4 Spin echo

In order to probe the spin-spin coherence time (T_2), a 'spin echo' pulse sequence can be applied (see figure 5.11). By applying a $180° = \pi$ pulse about the x-axis after inhomogeneous dephasinge has built up, the states are allowed to refocus, reversing the effect of the previously accumulated dephasing. This allows the effects of $T_2{}^*$ dephasing to be largely eliminated, although by applying dynamic decoupling methods noise can be better refocused.

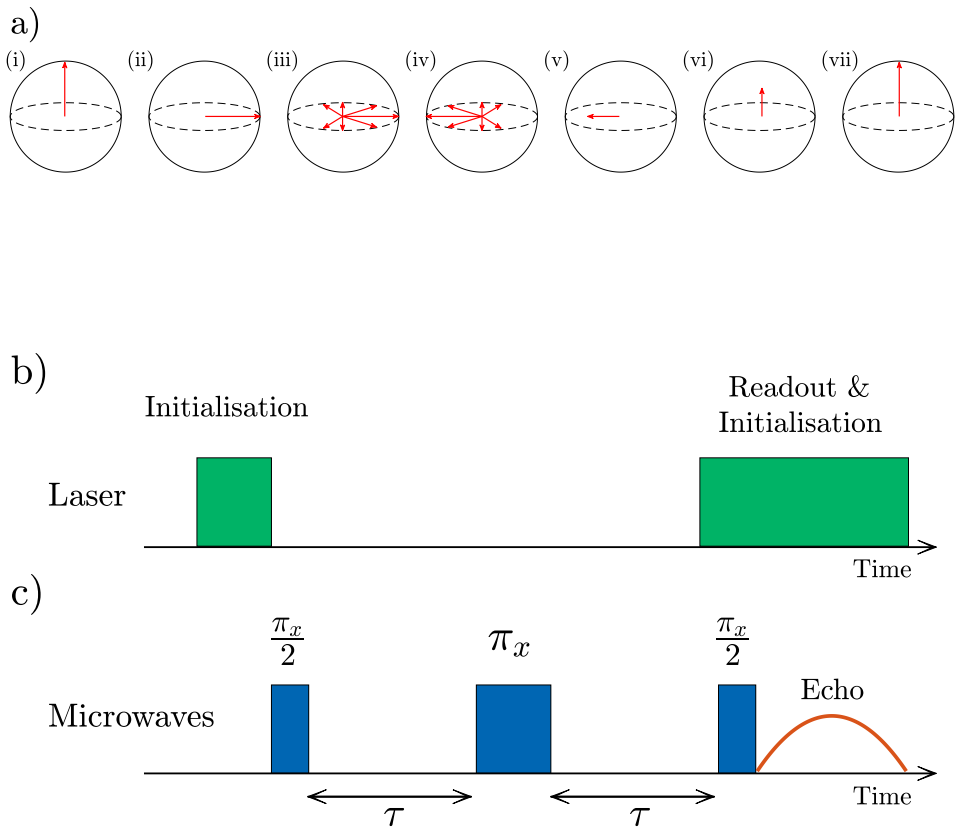

Figure 5.11: The spin echo pulse scheme: the effect of the laser (b) and microwave (c) pulse sequences on the magnetisation vector of the NV$^-$(a). An initial laser pulse prepares the spin by placing it into the $|0\rangle$ state (i). The NV is then placed in a quantum superposition (ii) with a $\frac{\pi_x}{2}$ microwave pulse. Decoherence is accumulated (iii) before a π_x rotates the vector through 180° around the x-axis. The same degree of decoherence is now accumulated again (iv), 180° rotated from the original accumulation, cancelling out the earlier decoherence. The spin echo then occurs (v) and a $\frac{\pi_x}{2}$ readout pulse is then applied to rotate the magnetisation vector (vi) so that it can be detected by measuring the fluorescence from a green laser excitation pulse. This pulse reinitialises the centre (vii) so that the sequence can be repeated.

5.3.5 Dynamic decoupling

Various pulse schemes exist which seek to further mitigate the effects of decoherence[15] in order to extend the spin coherence time of a system. By applying coherent radio frequency pulses across other axes (compared to the spin echo method above)[16, 17] the Carr-Purcell-Meiboom-Gill (CPMG) method of dynamic decoupling further reduces the effects of decoherence, allowing the measurement of longer times. These methods are not employed in this research, but they could be useful in potential future research.

5.4 Optically detected magnetic resonance (ODMR) of fluorescent nanodiamonds

This section discusses previous research into optically detected magnetic resonance of nanodiamonds and introduces the fabrication and processing of samples of nanodiamond used for the research detailed later in this thesis.

Research into NV^- spin coherence times (see section 5.3.3), both in bulk- and nano-diamond has made significant progress by taking into account the factors discussed in chapter 4, such as particle size and surface termination. Material purity and crystallographic quality, both controllable as a result of fabrication processes, have led to high quality diamond with long coherence times. However, in nanodiamond various factors, most notably nitrogen dopant concentration, particle size and surface quality, have limited the maximum coherence times achieved.

Alongside changes to material properties, advanced microwave and laser pulse sequences such as dynamic decoupling have allowed researchers to mitigate various effects which would otherwise reduce measured coherence times.

5.4.1 Spin-spin decoherence

In 2013, Knowles et al. showed that electron T_2 coherence times in nanodiamond, i.e. the length of coherence limited by spin-spin interactions, could be extended to $>$ 60 µs at room temperature.[18] Though this research made use of dynamic decoupling techniques, it found that nearby nitrogen impurities, as opposed to surface states, limited the NV$^-$s coherence time to significantly lower than those in higher purity diamond.

The following year, researchers at the Massachusetts Institute of Technology (MIT) demonstrated NV T_2 coherence times in excess of 200 µs, also by employing dynamical decoupling[19] using diamond nanopillars.

Also by employing the nano-pillar approach, T_2 times in excess of 700 µs were reported, once again making use of dynamic decoupling.[20] This time the diamond precursor was isotopically purified to remove ^{13}C atoms from the lattice, thus eliminating their contribution to spin-spin decoherence. This study found that the low levels of impurities and the isotopic purity of these nanodiamonds led to their NV$^-$ defects having significantly longer spin coherence times than those of less pure, less isotopically pure nanodiamonds of similar dimensions, fabricated in a similar manner. This is due to the spin of ^{13}C atoms as well of those of substitutional impurities acting to impart decoherence on the spin of the NV$^-$. However, the nanopillar method only creates nanodiamonds in one two-dimensional plane at a time, whilst milling produces them in three dimensions simultaneously which isn't much faster in practice when large numbers of nanodiamonds are required. A single 500 μm $\times$ 500 μm diamond membrane can only produce approximately 6.3 $\times 10^5$ nanodiamonds. This is too few to be practically compatible with many applications.[21]

5.5 Samples used for research

The nanodiamonds used for this research are milled from a single type of diamond precursor. Twenty standard grade single crystal CVD specimens from Element Six with an initial N_s^0 concentration of $\approx$ 121 ppb were irradiated in order to create vacancies (known as GR1 centres). Irradiation parameters are contained in table 5.1.

Parameter	Value
Beam energy	4.5 MeV
Beam current	20 mA
Exposure time	1 min
V production rate	0.3 ppm/hr*

Table 5.1: Electron irradiation parameters for ball milled nanodiamonds. *The expected vacancy production rate was estimated from work conducted by Andrew Edmonds with Warwick University in 2008, as detailed in his thesis.[22] However, the facility used (Synergy Health, Swindon, UK) is not well characterised and so precise irradiation damage rates are prone to a large error.

After irradiation, the samples were annealed following the method detailed by Chu et al,[23] allowing vacancies to migrate and eventually combine with N_s^0 to form NV centres:[24, 25]

- Inserted into furnace at 400 °C and maintained for 3 hours
- 4 hours at 800 °C
- 2 hours at 1200 °C
- Allowed to passively cool down to room temperature (taking a few hours to stabilise).

The precursor samples were then ball milled with silicon nitride at Cardiff University by Soumen Mandal, Laia Ginés and Oliver Williams' group, with the

expectation of producing a range of nanodiamond sizes, with those nanodiamonds of roughly 500 nm diameter containing approximately one NV. Beginning with an N_s^0 concentration $\rho_{N_s^0} \approx 100$ ppb the expected substitutional nitrogen concentration for such a nanodiamond can be calculated. Per cubic micron, $\rho_{N_s^0}$ is:

$$\rho_{N_s^0} = 2 \times 10^{16}\,\mathrm{cm}^{-3} = 2 \times 10^{4}\,\mu\mathrm{m}^{-3} \tag{5.19}$$

and the volume V of an ND of radius $r = 0.25\,\mu$m is:

$$\frac{4}{3}\pi r^3 = \frac{4}{3}\pi 0.25^3 \approx 0.06\mu m^3 \tag{5.20}$$

Using these figures, the number of N_s^0 per nanodiamond, n can be given as:

$$n = V\rho_{N_s^0} \approx 1.25 \times 10^3 \tag{5.21}$$

With an NV production rate around $1/1000$ the number of N_s^0, this leads to around one NV per 500 nm diameter nanodiamond. In reality some larger nanodiamonds will contain a single NV and some smaller nanodiamonds will contain more than one NV. Rather than expecting a certain sized nanodiamond to contain a specific number of NVs then, NV concentration was determined per-ND by confocal fluorescence microscopy (see chapter 7). Due to the reactive nature and the comparative inertness of molecular nitrogen, it is assumed that these NDs possess a largely oxygen terminated surface. However, as discussed in chapter 4, the true nature of the surface termination is likely to contain a mixture of various carbon-, hydrogen- and oxygen-containing molecules.

Chapter 5 References

[1] C. Rudowicz and S.K. Misra. Spin-Hamiltonian Formalisms in Electron Magnetic Resonance (EMR) and Related Spectroscopies. *Applied Spectroscopy Reviews*, 36(1):11–63, 2001.

[2] Arthur Schweiger and Gunnar Jeschke. *Principles of Pulse Electron Paramagnetic Resonance*. Oxford University Press, 2001.

[3] B. Odom, D. Hanneke, B. D'Urso, and G. Gabrielse. New measurement of the electron magnetic moment using a one-electron quantum cyclotron. *Phys. Rev. Lett.*, 97:030801, Jul 2006.

[4] G.R. Eaton, S. S. Eaton, D. P. Barr, and R. T. Weber. *Quantitative EPR*. Springer-Verlag Wien, 2010.

[5] Ruslan P. Ozerov and Anatoli A. Vorobyev. Elements of Quantum Mechanics. In Ruslan P. Ozerov and Anatoli A. Vorobyev, editors, *Physics for Chemists*, pages 423 – 496. Elsevier, Amsterdam, 2007.

[6] Christopher C. Rowlands and Damien M. Murphy. EPR Spectroscopy Theory. In John C. Lindon, editor, *Encyclopedia of Spectroscopy and Spectrometry*, pages 445 – 456. Elsevier, 1999.

[7] Maxie M. Roessler and Enrico Salvadori. Principles and applications of epr spectroscopy in the chemical sciences. *Chem. Soc. Rev.*, 47:2534–2553, 2018.

[8] Richard A Dunlap. Hyperfine interactionspart iii: the magnetic dipole interaction

and the nuclear zeeman effect. In *The Mössbauer Effect*, 2053-2571, pages 7–1 to 7–4. 2019.

[9] M. W. Doherty, N. B. Manson, P. Delaney, F. Jelezko, J. Wrachtrup, and L. C. L. Hollenberg. The nitrogen vacancy colour centre in diamond. *Physics Reports*, 528:1–45, 2013.

[10] P. Delaney, J. C. Greer, and J. A. Larsson. Spin-Polarization Mechanisms of the Nitrogen-Vacancy Center in Diamond. *Nano Letters*, 10(2):610–614, Feb 2010.

[11] N. Mizuochi, P. Neumann, F. Rempp, J. Beck, V. Jacques, P. Siyushev, K. Nakamura, D. J. Twitchen, H. Watanabe, S. Yamasaki, F. Jelezko, and J. Wrachtrup. Coherence of single spins coupled to a nuclear spin bath of varying density. *Phys. Rev. B*, 80:041201, Jul 2009.

[12] Surface and size effects on the charge state of NV center in nanodiamonds. *Computational and Theoretical Chemistry.*

[13] Emma R Wilson, Lindsay M Parker, Antony Orth, Nicholas Nunn, Marco Torelli, Olga Shenderova, Brant C Gibson, and Philipp Reineck. The effect of particle size on nanodiamond fluorescence and colloidal properties in biological media. *Nanotechnology*, 30(38):385704, 2019.

[14] P.-H. Chung, E. Perevedentseva, and C.-L. Cheng. The particle size-dependent pbotoluminescence of nanodiamonds. *Surface Science*, 601(18):3866–3870, 2007.

[15] L. Viola and S. Lloyd. Dynamical suppression of decoherence in two-state quantum systems. *Phys. Rev. A*, 58:2733–2744, Oct 1998.

[16] H. Y. Carr and E. M. Purcell. Effects of diffusion on free precession in nuclear magnetic resonance experiments. *Phys. Rev.*, 94:630–638, May 1954.

[17] S. Meiboom and D. Gill. Modified SpinEcho Method for Measuring Nuclear Relaxation Times. *Review of Scientific Instruments*, 29:688, 1958.

[18] Helena S. Knowles, Dhiren M. Kara, and Mete Atatüre. Observing bulk diamond spin coherence in high-purity nanodiamonds. *Nature Materials*, 13(21), Nov 2013.

[19] Matthew E. Trusheim, Luozhou Li, Abdelghani Laraoui, Edward H. Chen, Hassaram Bakhru, Tim Schroeder, Ophir Gaathon, Carlos A. Meriles, and Dirk Englund. Scalable Fabrication of High Purity Diamond Nanocrystals with Long-Spin-Coherence Nitrogen Vacancy Centers. *Nano Letters*, 14(1):32–36, Jan 2014.

[20] P. Andrich, B. J. Alemán, J. C. Lee, K. Ohno, C. F. de las Casas, F. Joseph Heremans, E. L. Hu, and D. D. Awschalom. Engineered Micro- and Nanoscale Diamonds as Mobile Probes for High-Resolution Sensing in Fluid. *Nano Letters*, 14:4959–4964, 2014.

[21] A. C. Frangeskou, A. T. M. A. Rahman, L. Gines, S. Mandal, O. A. Williams, P. F. Barker, and G. W. Morley. Pure nanodiamonds for levitated optomechanics in vacuum. *New Journal of Physics*, 20(1):043016, 2018.

[22] A. Edmonds. *Magnetic resonance studies of point defects in single crystal diamond*. PhD thesis, University of Warwick, 7 2008.

[23] Y. Chu, N. P. de Leon, B. J. Shields, B. Hausmann, R. Evans, E. Togan, M. J. Burek, M. Markham, A. Stacey, A. S. Zibrov, A. Yacoby, D. J. Twitchen, M. Loncar, H. Park, P. Maletinsky, and M. D. Lukin. Coherent Optical Transitions in Implanted Nitrogen Vacancy Centers. *Nano Letters*, 14(4):1982–1986, Apr 2014.

[24] G Davies and A.T. Collins. Vacancy Complexes in Diamond. *Diamond and Related Materials*, 2(2-4):80–86, Mar 31 1993.

[25] D. J. Twitchen, M. E. Newton, J. M. Baker, T. R. Anthony, and W. F. Banholzer. Electron-paramagnetic-resonance measurements on the divacancy defect center $r4/w6$ in diamond. *Phys. Rev. B*, 59:12900–12910, May 1999.

Chapter 6

Magnetometry

6.1 Ensemble NV magnetometry

In chapter 5, the discussion of ODMR centred around magnetic resonance experiments using single nitrogen vacancy centres in nanodiamonds. However, the same principles can be applied to ensembles of NV$^-$s in bulk diamond. In general, by employing continuous wave (CW) ODMR, the shot-noise limited[1] sensitivity η_{CW} of an ensemble NV magnetometer can be given as follows:[2]

$$\eta_{CW} = \frac{4}{3\sqrt{3}} \frac{h}{g_e \mu_B} \frac{\Delta\nu}{C_{CW}\sqrt{R}} \tag{6.1}$$

where the resonance line width $\Delta\nu$ and ODMR contrast C_{CW} are both dependent on the number of NV$^-$s in the excitation/detection volume. R, the photon detection rate depends on the optical system and is proportional to the number of NV centres. The other terms are defined in chapter 5.

Magnetometers employing established technology, such as flux gate[3] and SQUID[4] magnetometers, are already capable of reaching sensitivities above and beyond those achieved by NV magnetometry. However, the NV magnetometer is attractive for a number of reasons. Firstly, it operates at room temperature, removing the need for bulky and/or expensive cryogens. Secondly, costs can be kept low as the wide absorption band of the NV$^-$ allows for the use of generic 532 nm solid state lasers for optical excitation. Thirdly, due to the quality of diamond material engineering, samples with symmetry axes along all four crystallographic axes are obtained, leading to full vector field sensing with a single diamond sample.[5, 6]

6.1.1 Basic setup

An NV magnetometer usually consists of four principal components: an excitation laser (usually at around 532 nm), a diamond sample containing NVs, a microwave antenna and a fluorescence detector such as a photodiode. In its simplest configu-

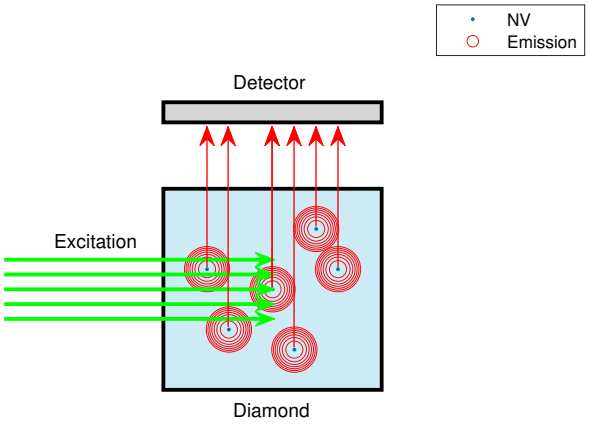

Figure 6.1: A simplistic view of an NV magnetometer. Excitation light (green arrows) is directed towards a diamond containing NV centres, which fluoresce omni-directionally (red rings). Some of this fluorescence (red arrows) arrives at the detector. A microwave antenna (not shown) delivers microwave radiation at approximately 2.88 GHz to enable ODMR. The omni-directional nature of the NV fluorescence emission demonstrates the need for optical elements to improve the collection efficiency of this arrangement.

ration, shown in figure 6.1, collection efficiency is low due to the omni-directional emission of fluorescence by the NV centres. This efficiency can be improved by the use of various optical elements such as collector lenses or optical fibre coupling configurations which lead to greater quantities of fluoresced photons reaching the detector.

6.1.2 Design considerations

The design and construction of an NV^- magnetometer depends heavily upon the nature of the field being measured. Regardless of practical considerations such as

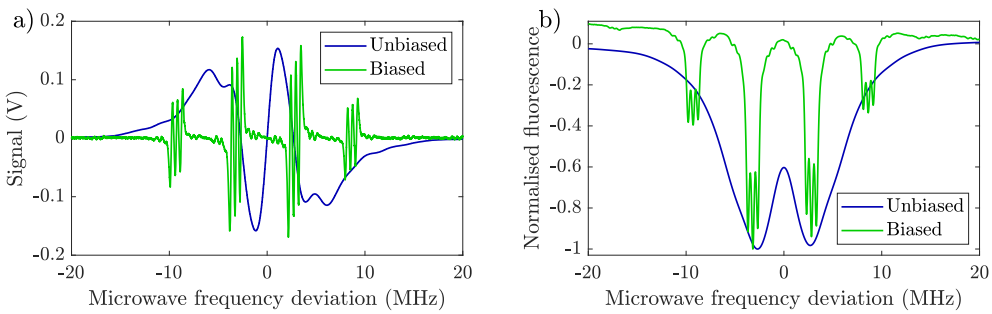

Figure 6.2: Derivative (a) and purely absorptive (b) ODMR spectra of NV$^-$ ensemble under zero bias field and under an arbitrary bias field aligned along the [1 1 1] axis. The application of the bias field lifts the degeneracy of the $m_s = \pm 1$ state, and the resonances are further split by hyperfine interactions.

environmental conditions, accessibility and target-specific concerns, the dynamic nature of the measured field will impact on the suitability of the device. Detection and measurement of static ('DC' - direct current) fields require a different approach to rapidly varying ('AC' - alternating current)[7] or narrow band signals. Whilst ensemble DC sensing is limited by the NV's inhomogeneous dephasing time (T_2^*), AC sensing is limited by the T_2 spin-spin decoherence time, which is typically longer[8] than T_2^* and which can be extended by applying dynamic decoupling techniques.[9] Magnetic fields can be measured by applying a bias field to an ensemble of NV$^-$s which lifts the degeneracy of the $m_s = \pm 1$ ground state (see figure 6.2, data acquired by Angelo Frangeskou and processed by the author) and results in sharper resonant features. By applying equation 5.4, changes to the resonant frequency of a particular transition allow changes to the magnetic field B_0 to be measured. Absolute measurement of magnetic field strength is also possible using NV$^-$ magnetometry, although due to the temperature dependence[10, 11] of the resonant frequency, ambient conditions must be well understood, or the NV ODMR can be used to measure temperature by recording two resonances simultaneously.

6.2 Magnetocardiography

Figure 6.3 shows the simplified design of a magnetometer initially built by Ben Green and Ben Breeze and then refined optically and electronically by the author and Angelo Frangeskou for the purposes of our research into NV based magnetocardiography.

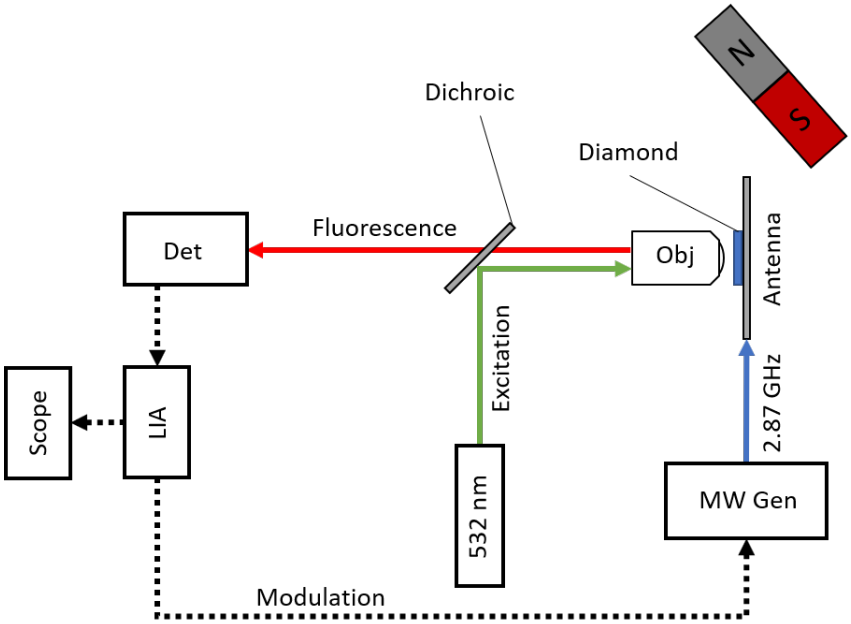

Figure 6.3: Layout of the NV magnetometer built for this research. Optical excitation is delivered and fluorescence collected via a microscope objective. Modulated 2.88 GHz excitation for driving between the $m_s = 0$ and $m_s = \pm 1$ ground state is applied via an antenna to the diamond sample. Fluorescence detection utilises a photodiode whose output is passed to an LIA and subsequently to an oscilloscope. A bias field is provided by a permanent magnet.

Magnetiocardiography, or MCG, is the study of the impulses of the heart by measuring the magnetic field generated by the heartbeat.[12, 13, 14] A more conventional and common technique, electrocardiography (ECG), is in widespread use but suffers from a number of technical barriers which reduce its usefulness in the early detection of symptoms of various cardiological illnesses.[12, 15] MCG by contrast can be performed without physical contact[15] with the patient. ECG is limited by the

interaction of the signal and the intervening tissue of the patient's chest, which is not a factor in MCG because human tissue in the chest is not sufficiently magnetic to distort magnetic signals, whilst it is electrically conductive enough to distort electrical signals.

Due to magnetic noise (from, for example, other nearby machinery and instruments), MCG has only been able to compete with ECG by employing magnetically shielded rooms (MSRs), a technique which was demonstrated in 1970.[16] Even within MSRs, MCG has typically required the use of superconducting quantum interference devices (SQUIDs), which require bulky and expensive cryogenic cooling.

Outside MSRs by employing gradiometry techniques to reduce environmental noise,[17] NVs aim to offer a room temperature, low cost and compact alternative to conventional MCG implementations.

6.3 Experimental considerations

6.3.1 Field homogeneity

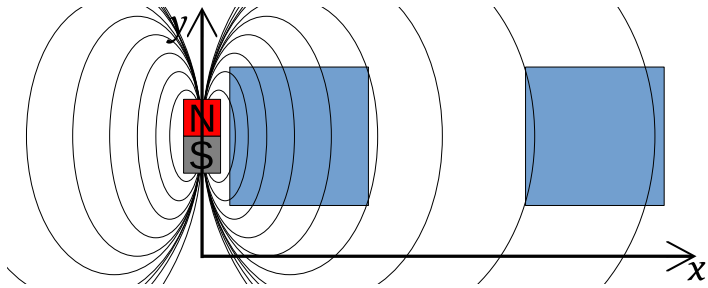

Figure 6.4: The effect of distance between the sensing area (blue squares) and the origin of a field, in this case a permanent magnet. The separation between field lines in the x direction indicates the steepness of the magnetic field gradient.

Homogeneity of both the bias and test/measured fields are essential, although that of the latter may not be controllable under real world conditions. Field homogene-

ity across the sensing volume ensures that all NVs within that volume experience a similar magnetic field. By contrast, an inhomogeneous field results in the resonances of different NVs being frequency shifted by different amounts, leading to broadening of the resonant ODMR lines. In order to reduce broadening, a strong bias magnet is placed at a comparatively large distance from the sensing volume to ensure a homogeneous field and therefore narrow resonances. Narrower resonant lines have steeper gradients than broader lines, and so smaller changes in magnetic field strength can be detected. Application of this bias field can impose constraints on the practical dimensions and physical shape of the magnetometer.

6.3.2 Fluorescence collection efficiency

For a collecting lens of $NA = 0.68$ such as that originally used in these experiments, obtaining light from a diamond ($n_2 = 2.42$)):

$$0.68 = 2.42 \sin \theta_2 \tag{6.2}$$

$$\theta_2 = 16.32^\circ \tag{6.3}$$

$$a = R \sin(16.32) \tag{6.4}$$

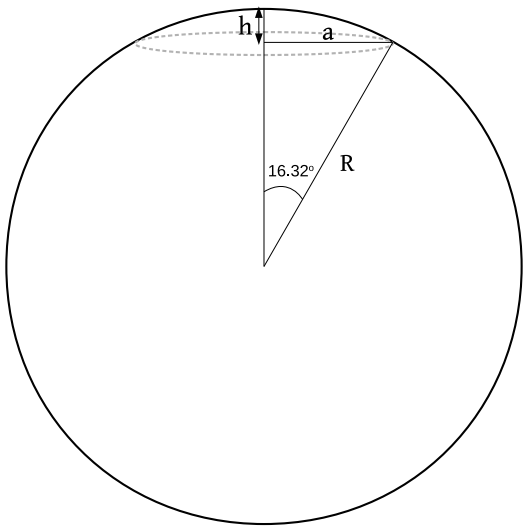

Figure 6.5: The surface area of the cap bounded by the circle of radius a at a distance h from the sphere's surface towards its centre, when compared to the sphere as a whole, will give the collection efficiency of the lens.

The collection efficiency of the lens, using equation 6.2 and figure 6.5 can be taken as:

$$\eta_{collect} = \frac{A_{cap}}{A_{sphere}} = \frac{\pi(a^2 + h^2)}{4\pi R^2} \tag{6.5}$$

which gives:

$$\eta_{collect} = \frac{\pi(\sin(16.32°)^2 + (1 - \cos 16.32°)^2)}{4\pi} = 0.02 \tag{6.6}$$

With a maximum possible collection efficiency of 2% and internal reflection further decreasing collection efficiency of an NV magnetometer using the design shown in 6.3, it is clear that there are improvements to be made which could substantially improve the sensitivity of an NV magnetometer using such a lens. Experiments using this magnetometer achieved a maximum sensitivity of $30\,\mathrm{nT}/\sqrt{\mathrm{Hz}}$. By reaching even 50% collection efficiency, this could potentially be brought down to around $2\,\mathrm{nT}/\sqrt{\mathrm{Hz}}$.

6.4 Potential improvements

6.4.1 Infrared absorption

Limitations exist when considering NV$^-$ fluorescence detection for magnetometry,[1] particularly poor fluorescence collection efficiency, contrast and unwanted background detection. In order to combat these issues, it has been proposed and demonstrated[18, 19] that instead of collecting fluorescence, the detection of infrared absorption in the ^{1}A singlet ground state of the NV$^-$ (see figure 6.6) could be employed to achieve improved signal-to-noise and approach the shot-noise limited sensitivity of the NV.

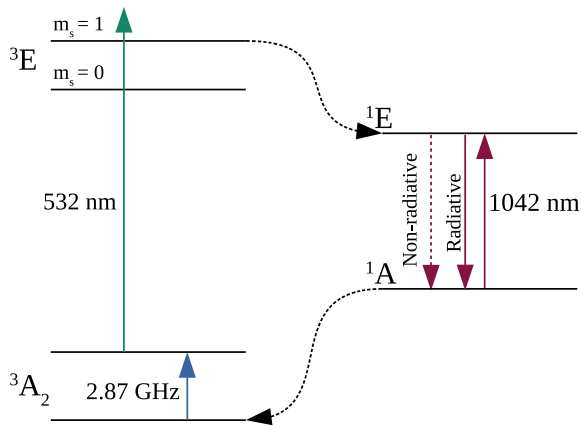

Figure 6.6: Resonant excitaion from the ^{3}A$_2$ $m_s = 0$ to the $m_s = 1$ state is driven by resonant microwave excitation, and is further excited to the corresponding ^{3}E state as with conventional fluorescence detection. Rather than detect fluorescence from photon emission back to the ground state though, absorption by excitation from the ^{1}A to the ^{1}E can be used for ODMR.

Bougas[18] proposes the use of light trapping diamond waveguides (LTDWs) similar to those explored by Clevenson et al[20] in which excitation light is reflected off the internal faces of the LTDW leading to longer excitation path lengths, whilst Dumeige[19] envisions a complex hybrid laser system. Meanwhile in 2010 it was demonstrated that sensitivities achieved using the infrared absorption method could

exceed those obtained via fluorescence collection,[21] although subsequent research increased[2] sensitivity using fluorescence detection to around $15\,\mathrm{pT}\cdot\mathrm{Hz}^{\frac{1}{2}}$ and perhaps even below $1\,\mathrm{pT}\cdot\mathrm{Hz}^{\frac{1}{2}}$.[22] In 2017, Chatzidrosos et al[23] demonstrated $28\,\mathrm{pT}\cdot\mathrm{Hz}^{\frac{1}{2}}$ sensitivity by employing NV IR absorption magnetometry using a cavity enhanced sensor.

Each of these absorption-based methodologies, both proposed and demonstrated, provide differing approaches to mitigating the limitations of NV fluorescence magnetometry, though all rely upon IR absorption as a means of detecting the magnetic resonance phenomena related to the defect. The use of LTDWs seeks to increase absorption of a 1042 nm probe beam by increasing the optical path length to be comparable to the absorption path length, whilst other methods mentioned rely on cavities and/or complex optics to achieve the same goal. Various NV magnetometry sensing regimes were reviewed by Barry et. al. in 2020.[24]

Using Bougas' LTDW proposal as a guide, we can see that it's possible to get similar results using a focused, fibre coupled design. In that research, a 2 W Laser Quantum gem532 532 nm solid state laser was used for excitation. A tunable 1042 nm, 100 mW probe beam was combined with the green pump beam and inserted into the two LTDWs with path lengths of 1.5 cm and 2.8 cm. These configurations resulted in absorption of 0.18% and 0.3% respectively, leading to inherently low sensitivity. This methodology suffers from two phenomena which are likely to reduce absorption of both pump and probe beams with greater optical path length. Firstly, the diameter of the combined beams ensures that intensity at a given point is comparatively low compared to a focused beam. Secondly, as path length increases, intensity will decrease as a result of optical extinction of both beams. Below (see fig. 6.8), an approach is proposed using focused, fibre coupled excitation and absorption detection which could be built to partially avoid these limitations. Further to this, the diamond material used was quoted with NV concentration of 0.2 ppm

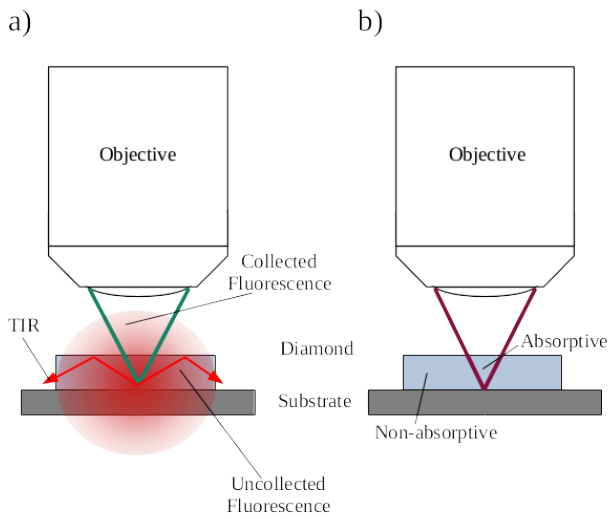

Figure 6.7: a) In conventional fluorescence detection, large amounts of signal are lost due to radiation away from the optical path. Similarly, a significant proportion of the signal is directed to the edge of the diamond by total internal reflection (TIR). b) In this hypothetical scheme, only material within the optical path is able to absorb and so no signal is lost, leading to collection efficiency nearing unity.

and 1.3 ppm. Increasing the NV concentration should further increase absorption of both pump and probe beams, potentially multiplying the signal by a factor of four. In Bougas' approach, linewidths and signal intensities were comparable with those achieved by by fluorescence detection. Lastly, by reflecting the excitation and collecting the absorption data in reflection, a second pass through the material is achieved, increasing absorption and simplifying collection (see figure 6.8). Improvements such as those mentioned could potentially allow nitrogen vacancy infrared absorption magnetometry to exceed the sensitivities achieved by fluorescence detection by reducing noise caused by unwanted background detection, increasing signal collection (see figure 6.7) and increasing excitation.

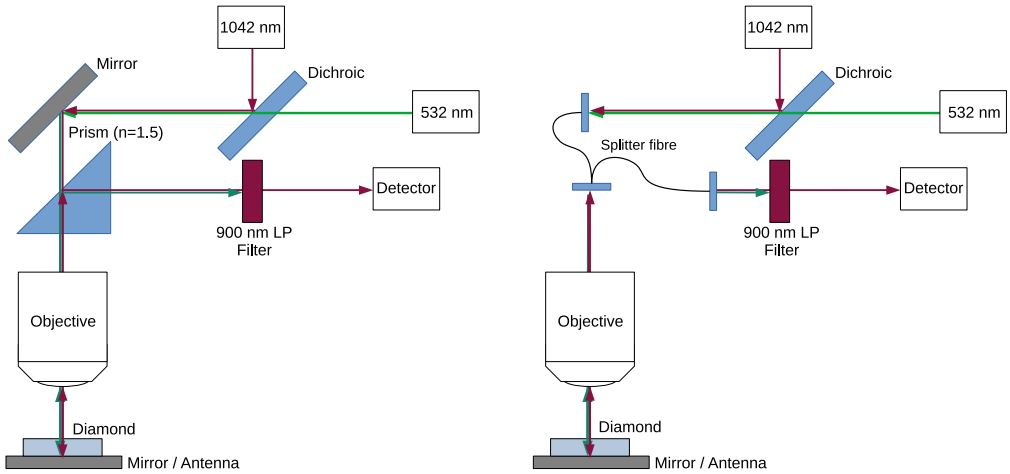

Figure 6.8: Layout of proposed design with free space optics (left) and a fibre coupled design (right). 1042 nm probe light is reflected by a silvered surface back through the objective, after which it is deflected from the incident path by a prism to a detector.

6.4.2 Gradiometry

One way of reducing noise and thereby improving the sensitivity of an NV magnetometer is to perform gradiometry by employing two identical sensors in parallel. Gradiometry measures the difference in magnetic field between two magnetometers,[25] rather than the absolute magnetic field at either detector, allowing for much more sensitive measurements. This would be a simple way in which to improve the diamond magnetometer described above, as was demonstrated in 2015[26] where an absorptive, fibre coupled NV magnetic gradiometer achieved a sensitivity of $60\,\mathrm{pT}/\sqrt{\mathrm{Hz}}$. Gradiometers have a number of applications such as the measurement of buried radioactive waste[27] and the study of geophysical[28] phenomena.

6.4.3 MCG imaging

Large numbers of MCG magnetometers like those discussed here could potentially be placed in a large array over a subject's chest in order to produce magnetocariographical maps of the patient. This configuration would utilise a large number of diamond magnetometers in a square array, with the resolution of the imaging system

being determined by the size of the sensing volume and the density of sensors within a given area. The disadvantage with such a system would be the large number of LIAs required; one dual channel LIA for every two magnetometers. At the cost of many commercially available LIAs, this cost would soon become prohibitive for many end users. At a cost of, for example, £10,000 for a single two channel LIA, this would reach more than £700,000 for a 12×12 pixel device, taking account of purchasing the LIAs alone. Whilst this cost is within reasonable range of larger hospitals, smaller outfits, particularly in developing countries, may not be able to justify such a cost. However, using the RePLIA described in chapter 2, this cost falls to approximately £14,400. The cost of optical equipment is not included in these calculations.

Chapter 6 References

[1] L Rondin, J-P Tetienne, T Hingant, J-F Roch, P Maletinsky, and V Jacques. Magnetometry with nitrogen-vacancy defects in diamond. *Reports on Progress in Physics*, 77(5):056503, 2014.

[2] J. F. Barry, Ma. J. Turner, J. M. Schloss, D. R. Glenn, Y. Song, M. D. Lukin, H. Park, and R. L. Walsworth. Optical magnetic detection of single-neuron action potentials using quantum defects in diamond. *PNAS*, 113:14133–14138, 2016.

[3] R.H. Koch, J.G. Deak, and G. Grinstein. Fundamental limits to magnetic-field sensitivity of flux-gate magnetic-field sensors. *Applied Physics Letters*, 75(24):3862–3864, Dec 13 1999.

[4] H. Weinstock. A review of SQUID magnetometry applied to nondestructive evaluation. *IEEE Transactions on Magnetics*, 27(2):3231–3236, 1991.

[5] D. Le Sage, K. Arai, D. R. Glenn, S. J. DeVience, L. M. Pham, L. Rahn-Lee, M. D. Lukin, A. Yacoby, A. Komeili, and R. L. Walsworth. Optical magnetic imaging of living cells. *Nature*, 496:486489, 2013.

[6] J. M. Schloss, J. F. Barry, M. J. Turner, and R. L. Walsworth. Simultaneous Broadband Vector Magnetometry Using Solid-State Spins. *Phys. Rev. Applied*, 10(3):034044, Sep 2018.

[7] J. M. Boss, K. Chang, J. Armijo, K. Cujia, T. Rosskopf, J. R. Maze, and C. L. Degen. One- and Two-Dimensional Nuclear Magnetic Resonance Spectroscopy with a Diamond Quantum Sensor. *Phys. Rev. Lett.*, 116(19):197601, May 2016.

[8] G. de Lange, Z. H. Wang, D. Ristè, V. V. Dobrovitski, and R. Hanson. Universal dynamical decoupling of a single solid-state spin from a spin bath. *Science*, 330(6000):60–63, 2010.

[9] D. Farfurnik, Y. Horowicz, and N. Bar-Gill. Identifying and decoupling many-body interactions in spin ensembles in diamond. *Phys. Rev. A*, 98(3):033409, Sep 2018.

[10] Y. Y. Hui, O. Y. Chen, T. Azuma, B.-M. Chang, F.-J. Hsieh, and H.-C. Chang. All-Optical Thermometry with Nitrogen-Vacancy Centers in Nanodiamond-Embedded Polymer Films. *Journal of Physical Chemistry C*, 123(24):15366–15374, 2019.

[11] M. Fukami, C.G. Yale, P. Andrich, X. Liu, F.J. Heremans, P.F. Nealey, and D.D. Awschalom. All-Optical Cryogenic Thermometry Based on Nitrogen-Vacancy Centers in Nanodiamonds. *Phys. Rev. Applied*, 12(1):014042, Jul 2019.

[12] J. S. W. Kwong, B. Leithäuser, J.-W. Park, and C.-M. Yu. Diagnostic value of magnetocardiography in coronary artery disease and cardiac arrhythmias: A review of clinical data. *International Journal of Cardiology*, 167:1835–1842, Jan 2013.

[13] S. Ghasemi-Roudsari1, A. Al-Shimary, B. Varcoe, R. Byrom, L. Kearney, and M. Kearney. A portable prototype magnetometer to differentiate ischemic and non-ischemic heart disease in patients with chest pain. *PLOS One*, 13(1):1–10, Jan 2018.

[14] T. Lachlan, H. He, K. Sharma, J. Khan, K. Rajappan, A. Morley-Davies, A. Patwala, H. Randeva, and F. Osman. Magneto cardiography parameters to predict future Sudden Cardiac Death (MAGNETO-SCD) or ventricular events from implantable cardioverter defibrillators: study protocol, design and rationale. *BMJ Open*, 10, Sep 2020.

[15] R. Fenici, D. Brisinda, and A. Meloni. Clinical application of magnetocardiography. *Expert review of molecular diagnostics*, 5:291–313, 06 2005.

[16] D. Cohen, E. A. Edelsack, and J. E. Zimmerman. Magnetocardiograms taken inside a shielded room with a superconducting point-contact magnetometer. *Appl. Phys. Lett*, 16:278, 1970.

[17] M. Bick, G. Panaitov, M. Schick, Y. Zhang, and H. J. Krause. Adaptive frequency dependent gradiometry applied to SQUID magnetocardiography. *IEEE Transactions on Applied Superconductivity*, 13(2, 1):364–367, Jun 2003.

[18] L. Bougas, A. Wilzewski, Y. Dumeige, D. Antypas, T. Wu, A. Wickenbrock, E. Bourgeois, M. Nesladek, H. Clevenson, D. Braje, D. Englund, and D. Budker. On the Possibility of Miniature Diamond-Based Magnetometers Using Waveguide Geometries. *Micromachines*, 9:276, 2018.

[19] Y. Dumeige, J.-F. Roch, F. Bretenaker, T. Debuisschert, V. Acosta, C. Becher, G. Chatzidrosos, A. Wickenbrock, L. Bougas, A. Wilewski, and D. Budker. Infrared laser threshold magnetometry with a nv doped diamond intracavity etalon. *Optics Express*, 27(2):1706, 2019.

[20] H. Clevenson, M. E. Trusheim, C. Teale, T. Schröder, D. Braje, and D. Englund. Broadband magnetometry and temperature sensing with a light-trapping diamond waveguide. *Nature Physics*, 11:393–397, 2015.

[21] V. M. Acosta, E. Bauch a), A. Jarmola, L. J. Zipp, M. P. Ledbetter, and D. Budker. Broadband magnetometry by infrared-absorption detection of nitrogen-vacancy ensembles in diamond. *Applied Physics Letters*, 97(17):174104, 2010.

[22] Ilja Fescenko, Andrey Jarmola, Igor Savukov, Pauli Kehayias, Janis Smits, Joshua Damron, Nathaniel Ristoff, Nazanin Mosavian, and Victor M. Acosta. Diamond magnetometer enhanced by ferrite flux concentrators. *arXiv:1911.05070v2*, 2019.

[23] G. Chatzidrosos, A. Wickenbrock, L. Bougas, N. Leefer, T. Wu, K. Jensen, Y. Dumeige, and D. Budker. Miniature Cavity-Enhanced Diamond Magnetometer. *Phys. Rev. Applied*, 8(4):044019, Oct 2017.

[24] John F. Barry, Jennifer M. Schloss, Erik Bauch, Matthew J. Turner, Connor A. Hart, Linh M. Pham, and Ronald L. Walsworth. Sensitivity optimization for NV-diamond magnetometry. *Reviews of Modern Physics*, 92(1), Mar 31 2020.

[25] S. M. Blakley, I. V. Fedotov, S. Ya. Kilin, and A. M. Zheltikov. Room-temperature magnetic gradiometry with fiber-coupled nitrogen-vacancy centers in diamond. *Optics Letters*, 40(16):3727–3730, Aug 15 2015.

[26] S. M. Blakley, I. V. Fedotov, S. Ya. Kilin, and A. M. Zheltikov. Room-temperature magnetic gradiometry with fiber-coupled nitrogen-vacancy centers in diamond. *Optics Letters*, 40(16):3727–3730, Aug 15 2015.

[27] Dale Franklin Rucker. The application of magnetic gradiometry and electromagnetic induction at a former radioactive waste disposal site. *Waste Management & Research*, 28(4):364–372, 2010.

[28] J.B. Nelson, D.L. Marcotte, and C.D. Hardwick. Magnetic-field Gradients and their uses in the study of the Earth's Magnetic Field. *Journal of Geomagnetism and Geoelectricity*, 44(5):367–370, 1992.

Chapter 7

Confocal microscopy

7.1 Room Temperature Confocal Fluorescence Microscopy

7.1.1 Operating principles

A confocal microscope has an advantage over conventional optical microscopes in that by using a pinhole it is able to reject out of focus light from regions outside the 'confocal volume',[1] i.e. the volume from which light may pass through the pinhole at the back focus of the objective lens, as opposed to light from outside this region which is predominantly rejected (see figure 7.1).

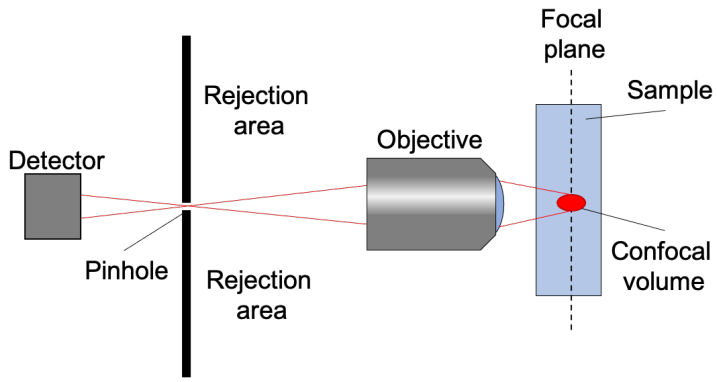

Figure 7.1: The pinhole in a confocal microscope accepts light from the confocal volume near the focal plane and allows it to pass through to the detector (red lines). Light originating outside the confocal volume does not come to focus on the pinhole and so is spread out, with only a small proportion entering the pinhole and the majority being rejected. Note that though the focal plane exists at a defined distance from the objective (the working distance), the confocal volume is an extended region, with the size of this volume being determined by the size of the pinhole, the excitation volume and the characteristics of the objective and any other optical components in the optical path.

The resultant sectioning leads to high levels of optical rejection away from the confocal volume and high resolution[2] in the z-axis (i.e. the axis that is normal to the focal plane in figure 7.1).

In a confocal fluorescence microscope (CFM), fluorescence is stimulated by an excitation beam and the stimulated fluorescence is then collected from the confocal

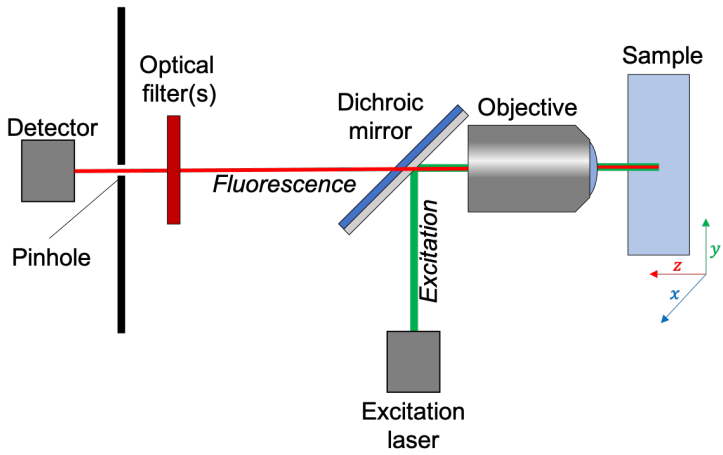

Figure 7.2: In confocal fluorescence microscopy, fluorescence in the sample is stimulated by an excitation beam which is directed into the objective and thus to the sample by a dichroic mirror which also allows fluorescence to be transmitted. Optical filtering reduces back scattered excitation light unintentionally reflected by the dichroic. The sample may be scanned through three dimensions in order to produce a map of the sample.

volume whilst back scattered excitation light is rejected by optical filtering (see fig. 7.2). If the sample is rastered in the xy plane, a map of fluorescence in an extended sample may be produced, and scanning along the z-axis allows fluorescence at varying depths to be detected. Also, in such apparatus the filtering medium may be removed or replaced to allow the collection of back scattered excitation light in place of the fluorescence. This is useful where the region surrounding the fluorescent material needs to be mapped out prior to the collection of fluorescence.

The setup of the confocal apparatus can be seen in figure 7.3. Excitation is provided by a Laser Quantum gem532, a horizontally polarised, transverse mode 532 nm diode laser with up to 100 mW output. This excitation light then passes through an Isomet 1250C acousto-optic modulator (AOM) which allows control of the laser output and also enables rapid switching of the excitation for pulsed ODMR experiments. An iris allows the first order emitted from the AOM to be passed whilst other orders are blocked. A beam expander is used to ensure that the excitation

light fills the back aperture of an objective, producing the appropriate numerical aperture for coupling into a single mode (SM) fibre. This fibre reduces the open beam portion of the path length of the excitation light, reducing the effect of flexing and vibrations of the optical table. Upon egress from the fibre, the excitation enters a second objective which re-collimates the beam, after which a $\frac{\lambda}{4}$ waveplate allows for polarisation of the excitation. The excitation beam then reflects off a dichroic mirror and into the sample objective and finally to the sample where it stimulates fluorescence.

The fluorescence initially takes the reverse path of the excitation light through the sample objective and then passes through the dichroic, although some excitation light also passes due to imperfect rejection by the dichroic. The remaining light is then filtered, first by a 630 nm long-pass (LP) filter and then by a 532 nm notch filter, which attenuate both the excitation light and any undesirable background light to manageable levels. The filtered fluorescence is then focused onto a pinhole and then re-collimated before encountering a 50:50 beam splitter which creates two beams of equal intensity and directs them to multimode (MM) fibre coupled single photon counting modules (SPCMs). Manual translation stages allow for the alignment of the MM fibres with the incoming fluorescence. This system was built and modified by Ben Green, Phil Diggle, Angelo Frangeskou, Colin Stephen and Ben Breeze. The single mode fibre alteration (as opposed to the previous free space design not shown here) was designed and implemented by Ben Green, Yashna Lekhai, Olga Young and myself. All measurements and data processing used in this chapter were performed by myself.

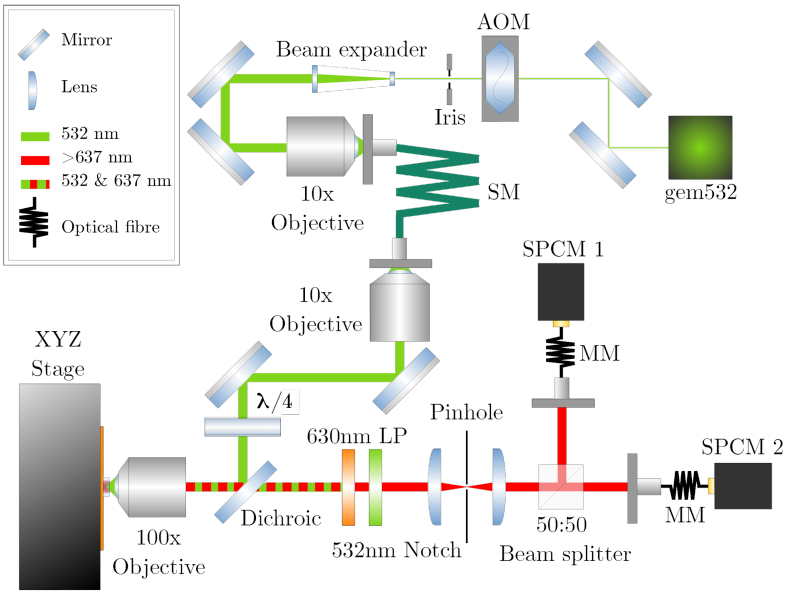

Figure 7.3: Layout of the confocal fluorescence microscope. Single photon counting modules (SPCMs) are employed to detect excitation from single NVs. The addition of a single mode fibre to the excitation arm reduces the effects of misalignment and movement within the optical table.

Hanbury Brown-Twiss

The use of two SPCMs and a 50:50 beam splitter enables the Hanbury Brown-Twiss experiment.[3] This takes two optical paths of equal length originating from a single source (an NV^-) and measures the arrival times of photons. Seeing as all photons travelling in similar media will travel an equal distance in an equal time, it follows that should multiple photons arrive at the detectors simultaneously, the source either is not a single photon emitter or is multiple single photon emitters. Photon detection times were measured by a Swabian Instruments Time Tagger Ultra and processed using Qudi experiment control software. Qudi, written at the University of Ulm and modified by Ben Green, Phil Diggle, Colin Steven and myself, allow for the complete operation of the confocal microscope system, including excitation control, sample positioning, object tracking and data acquisition. Automation scripting for the NV

statistics measurements (see section 7.4.1) were written by myself. The correlation of intensities from the two detectors shows a characteristic anti-bunching dip at time $\tau = 0$ (see figure 7.4).

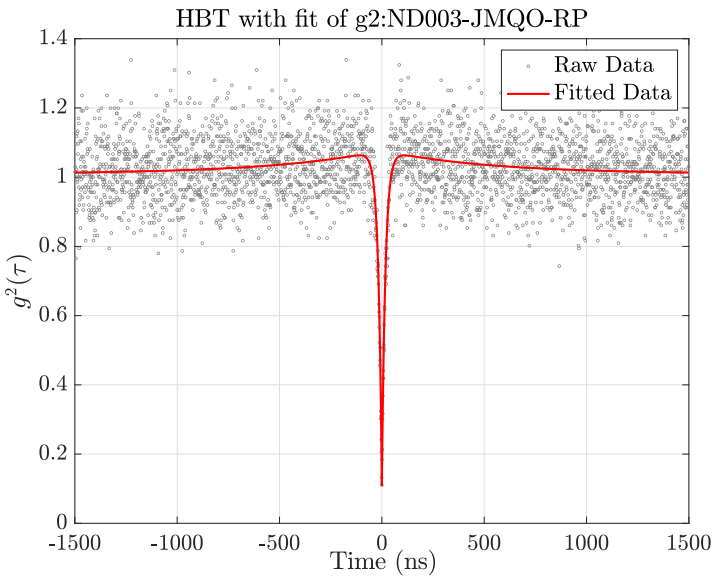

Figure 7.4: Result of an HBT experiment. The characteristic anti-bunching dip must fall below $g^{(2)}(0) = 0.5$ to be considered a single emitter. Data is fit to $(1-(1+a)\cdot e^{\frac{-|x|}{\tau_1}}) + a \cdot e^{\frac{-|x|}{\tau_2}}$ which describes a three-level system where τ_1 is the estimated fluorescence lifetime, τ_2 is the estimated shelving rate of the NV and x is the arrival time of a particular photon.

The fluorescence lifetime τ_1 is characterised by the time taken for excitation r_{12} and relaxation r_{21} between the ground and excited states:

$$\frac{1}{\tau_1} = r_{12} + r_{21} \tag{7.1}$$

The shelving rate τ_2 can be defined as:

$$\frac{1}{\tau_2} = r_{31} + \frac{r_{23} r_{12}}{\tau_1} \tag{7.2}$$

where r_{23} is the time taken for relaxation from the excited state to the shelving states

and r_{31} is the time taken for relaxation from the shelving states to the ground state. The number of emitters present can be determined by assessing the minimum value of the anti-bunching dip using the following formula:

$$g^{(2)}(0) = \frac{n(n-1)}{n^2} \tag{7.3}$$

where n is the number of single emitters contributing to the signal. Using this formula then a $g^{(2)}(0)$ of ≤ 0.5 is taken to indicate the presence of a single NV$^-$ within the confocal volume.

7.2 Silicon maps

n-type phosphorus doped silicon wafers were etched by Yashna Lekhai with an addressed grid pattern designed by Colin Stephen and myself in order to allow for the identification and location of specific nanodiamonds. Phosphorus doping was chosen so that the negative charge on the wafer might reduce the likelihood of charge state switching by the NV$^-$. These maps allow samples to be moved between various experiments without losing track of particular nanodiamonds.

Si wafer segments (5 mm $\times$ 5 mm) were prepared with 2.5 $\times$ 2.5 mm etched grids. Each 5 mm $\times$ 5 mm wafer has its own unique 2 letter code. Each of these maps is then subdivided into 625 blocks which are again addressed by a 2 letter code. Each of these blocks is further subdivided into 16 unaddressed squares. The square containing the 2 letter address is known as 0,0 (referring to rows and columns respectively). Reading from top to bottom for rows and right to left for columns, the further 15 squares are labelled accordingly. For example, CH-BD-2,3 is the square second from the bottom on the left hand column of block BD on wafer CH (see figure 7.5).

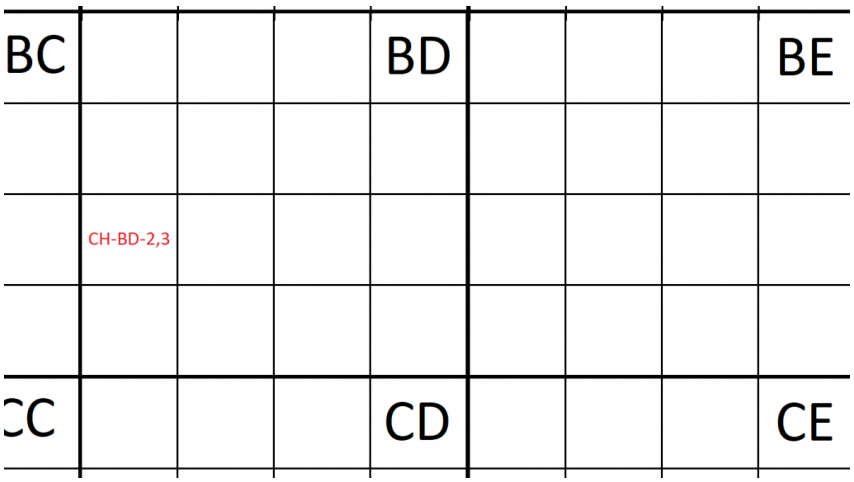

Figure 7.5: Illustration of the mapping system in use on the silicon wafer samples.

7.2.1 Nanodiamond deposition

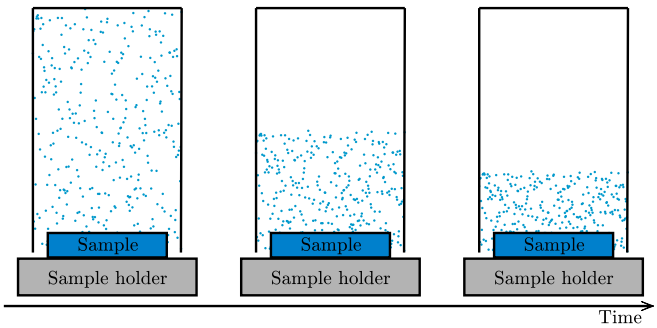

Figure 7.6: Nanodiamonds suspended in methanol are sprayed into an upturned glass vial and are allowed to precipitate onto the silicon sample surface.

Nanodiamonds were held in a suspension of HPLC methanol (CH_3OH) at a density of approximately 1 mg/ml and sprayed for three seconds by a nebuliser (Omron MicroAIR U22) into an upturned vial, ensuring that a high density of nanodiamonds were injected. The nanodiamonds were then allowed to precipitate onto the Si wafers (see figure 7.6). This was to reduce the 'coffee-ring' effect often seen in drop casting and to prevent aggregation which was found to be prevalent when using direct

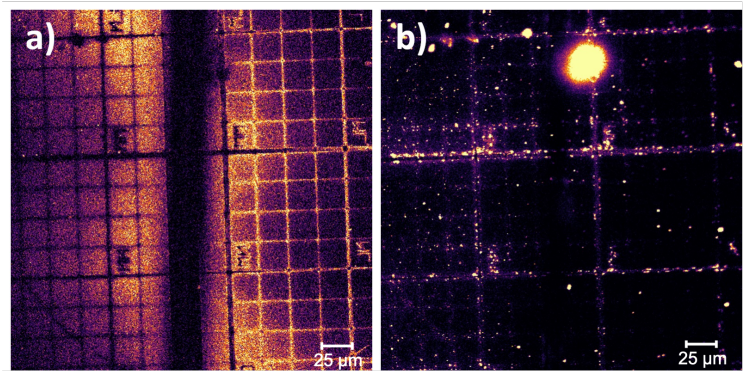

Figure 7.7: a) a reflection image of a silicon map and a fluorescence image of the same region (b). The solid black vertical bar is a microwave delivery antenna positioned above the focal plane. Larger squares span 100 µm whilst the smaller cells are 25 µm across.

spray application. This application was repeated six times in order to be confident of sufficient coverage of the Si wafer by the nanodiamonds.

7.2.2 Confocal mapping

By temporarily reducing green rejection on the CFM it is possible to image non-fluorescent materials by collecting light reflected by the sample as opposed to emitted fluorescence. This then produces a spatially accurate image of the sample surface. Larger nanodiamonds are also visible, although as the diffraction limited CFM has a maximum resolution larger than many of the nanodiamonds in use, it is not a reliable method of finding or characterising the physical dimensions of NDs (see subsection 7.2.3). It is however adequate to spatially identify physical locations on the maps, which are labelled using a unique addressing system (see figures 7.7a and 7.5).

Once the physical position of the sample has been identified, green rejection is implemented and fluorescence imaging can take place (see figure 7.7b). This image can be combined with the reflection image to provide an addressed fluorescence map of the sample.

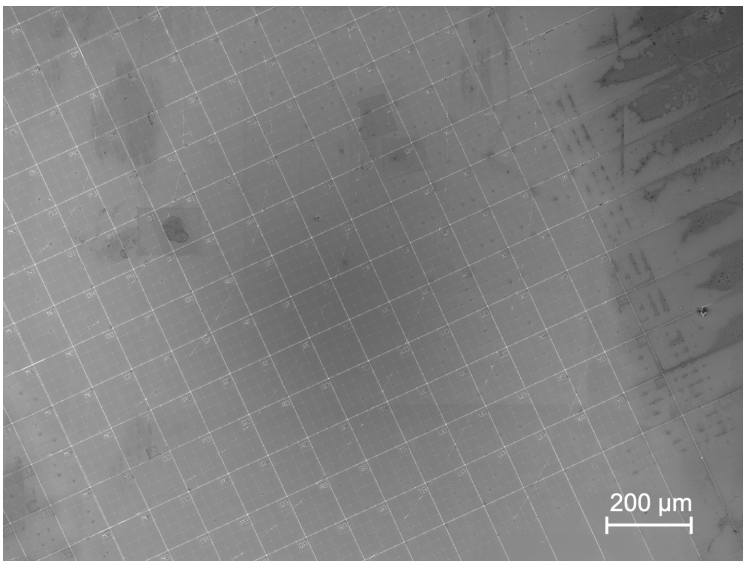

Figure 7.8: Scanning electron microscope image of a silicon map before ND deposition. Irregular dark patches are unidentified contamination which was not able to be removed, whilst rectangular dark areas are locations which have been previously imaged under SEM, with the expectation being that electron irradiation from the microscope has modified the silicon dioxide surface.

7.2.3 SEM

Scanning electron microscopy enables highly accurate measurements of the physical dimensions of nanodiamonds. By matching up SEM images with the combined reflection/fluorescence images described in section 7.2.2, CFM data can be attributed to particular nanodiamonds of now known dimensions. All SEM data in this thesis were acquired by myself using a Zeiss Supra scanning electron microscope located at the University of Warwick.

As well as allowing the dimensions of NDs to be measured, placing samples into the SEM makes it possible to distinguish whether or not a particular source of fluorescence represents a single ND or multiple NDs in close proximity.

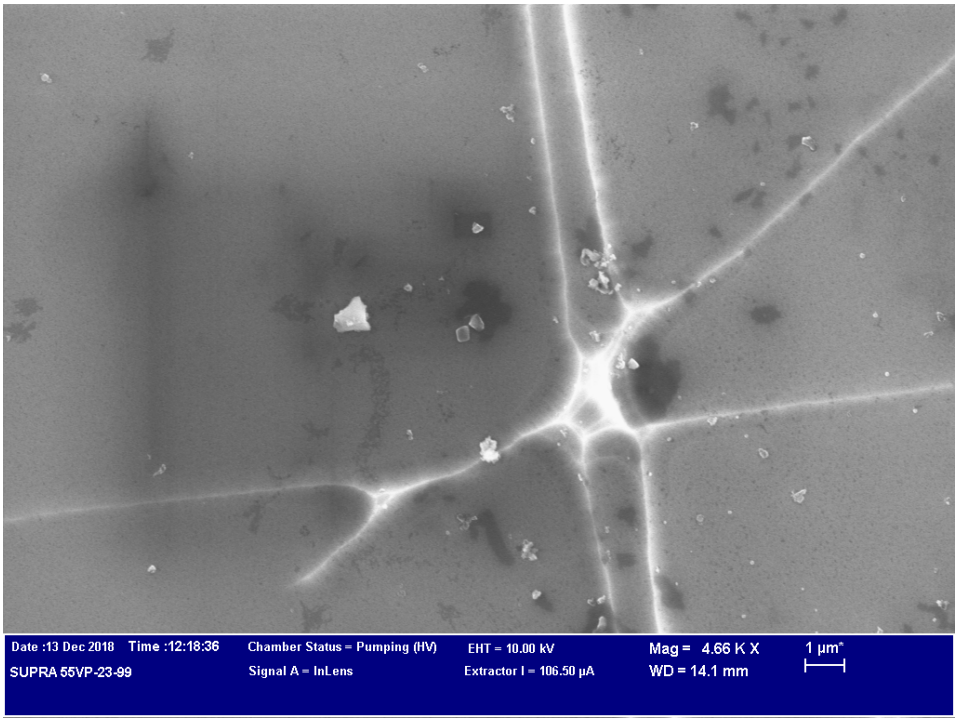

Figure 7.9: SEM image of nanodiamonds deposited on the surface of a silicon wafer. The large tracks visible here are part of the grid shown in figure 7.8.

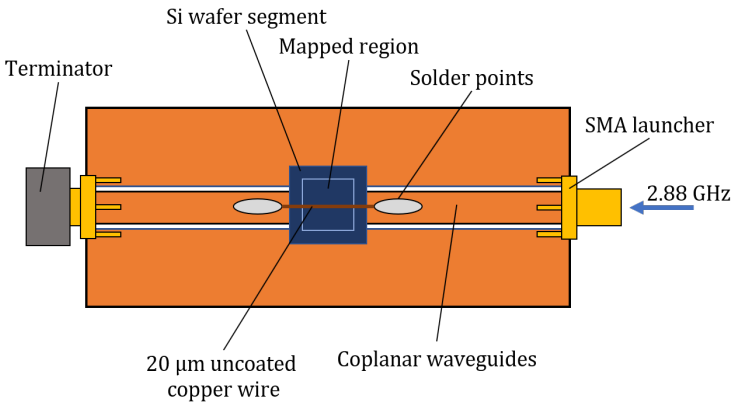

Figure 7.10: Confocal sample holder with inbuilt coplanar waveguide and antenna for microwave delivery. The mapped region is the area described in section 7.2.2.

7.3 Continuous Wave ODMR

In chapter 5, the physical principles of ODMR were discussed. In confocal microscopy, these principles can be applied to either bulk diamond or nanoscale particles using the sample mount seen in figure 7.10. In this configuration, a waveguide delivers microwave radiation at 2.88 GHz to a linear antenna in the form of a 20 µm diameter copper wire which sits atop the sample. This antenna provides an area approximately 50×300 µm, the dimensions of which are constrained by the 300 µm travel of the stage and the useful radiative range of the antenna. This latter dimension is dependent on several factors such as the diameter of the antenna, the power delivered and the vertical distance between the antenna and the sample which is not easily controlled. The sample holder can be scanned over the microscope objective to provide a confocal image, and can be positioned with nm precision to take measurements of specific sites.

In continuous wave ODMR (CW-ODMR) on the confocal microscope, with an applied bias magnetic field the positions of the resonances can be used to align the bias field so that the field lines run parallel to the axis of the NV. This is achieved

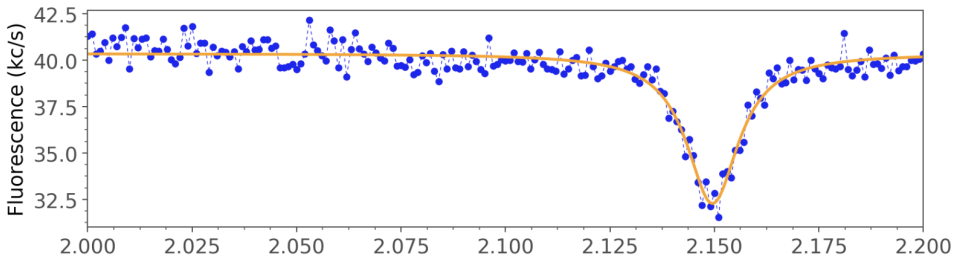

Figure 7.11: Continuous wave ODMR spectrum of ND1 (see fig. 7.13). This spectrum was taken in order to align the bias magnetic field with the symmetry axis of the NV by iteratively altering the magnet position whilst attempting to achieve the lowest possible frequency of the observed resonance (identified by the dip in fluorescence).

by maximising the frequency separation of the resonances (i.e. the $m_s = +1$ and $m_s = -1$ states) in a frequency swept ODMR spectrum (see fig. 7.11). In such a configuration, the strength of the field should have no effect on the fluorescence output of the NV as the magnetic field is now aligned along the defect's symmetry axis. This can be checked by altering the distance between the magnet producing the bias field and the sample, and monitoring the fluorescence in real time. The accurate alignment between the NV symmetry axis and the magnetic field are essential for accurate assessment of spin decoherence times with pulsed ODMR. This alignment is performed by the reorientation of the bias field magnet which is achieved using a linear motor and two rotational motors, all manually operated, connected to an aluminium arm which holds the bias magnet. This allows for three axis positioning of the magnet through approximately one eighth of a spherical area surrounding the sample.

7.3.1 Nanodiamonds

Nanodiamonds pose challenges for confocal ODMR that are not a concern when probing single crystal material. In the latter example, NVs will have only one of four orientations relative to the sample, so once these four orientations are ascertained,

magnetic field alignment for a given NV is trivial. For nanodiamonds however, the orientation of the NV is arbitrary, so complete alignment of the field is required for each nanodiamond.

Difficulties may also arise due to the random morphology of nanodiamonds manufactured by the milling process discussed in chapter 4. Although nanodiamonds smaller than the diffraction limit of the emitted light should act as point sources,[4, 5] NDs larger than this can have an unpredictable optical effect on the emission of NV fluorescence from an unknown ND geometry which could lead to circumstances where the collection efficiency of the equipment becomes insufficient for reliable measurements. An example of this might include a large, irregularly shaped nanodiamond where internal reflections might lead to asymmetric emission of light from the diamond. This is particularly the case during pulsed measurements where the experimental conditions further limit emission. In such a case, low excitation as a result of the duty cycle of the laser can cause the nanodiamond to be insufficiently bright for tracking by the Qudi software, and so the signal may be lost before adequate data have been collected. In practical terms this can lead to situations where many hours of collection are required to achieve sufficient signal to noise but NV fluorescence is too low to enable tracking of the ND with the piezoelectric stage.

Further to this, ODMR appears to become undetectable at a shorter distance from the antenna when operating on NDs on silicon compared to NVs in bulk diamond. This may be explained by the shape of the silicon maps after cutting often leading to the suspension of the antenna at a distance of a few microns from the surface, decreasing microwave intensity for a given NV. This can be limited by cutting silicon wafers from the underside, so that no ridges are produced around the cutting area (see fig. 7.12) and thereby reducing the distance between the antenna and the sample, and by ensuring that the length of the antenna is kept to a minimum, thus limiting microwave emission only to the desired experimental area, as opposed to

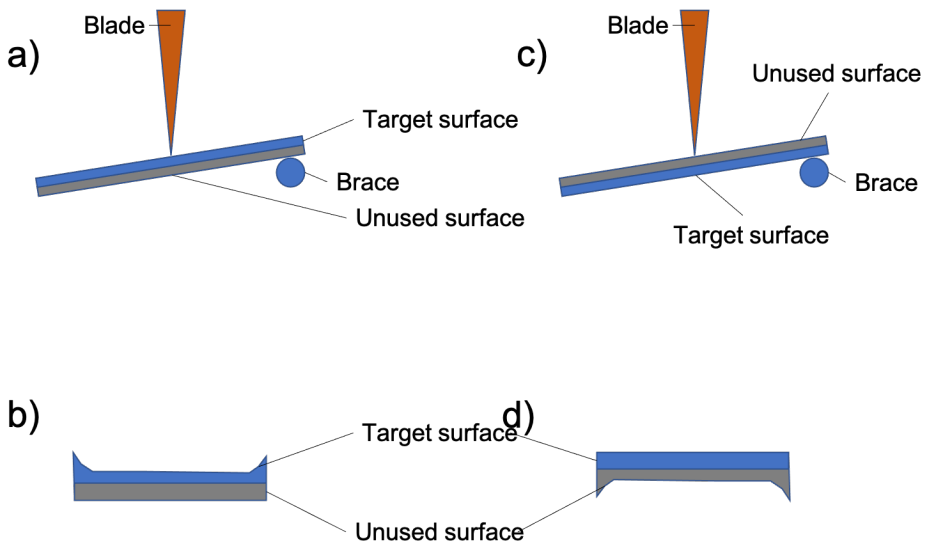

Figure 7.12: Cutting a wafer involved placing a brace (a small cylinder of metal) beneath the wafer and pushing down with a blade, causing the wafer to snap along a scored line. a) When the blade is placed against the target surface (i.e. the side to be imaged), the cutting action causes ridges to form on that surface (b). This can be alleviated by placing the wafer target side down on the brace (c) which results in the ridges being formed on the unused surface (d), meaning that an antenna can sit flush with the target surface.

a longer antenna which might lose energy by radiating across areas not used for measurement.

These issues lead to the fact that large numbers of NVs in a given sample are inappropriate or inaccessible for measurement.

7.4 Microscopy results

Figure 7.13 shows confocal fluorescence data overlaid on a confocal reflection image and an SEM image. The relevant nanodiamond, labelled ND1, is shown in all three images and using the SEM its dimensions can be measured.

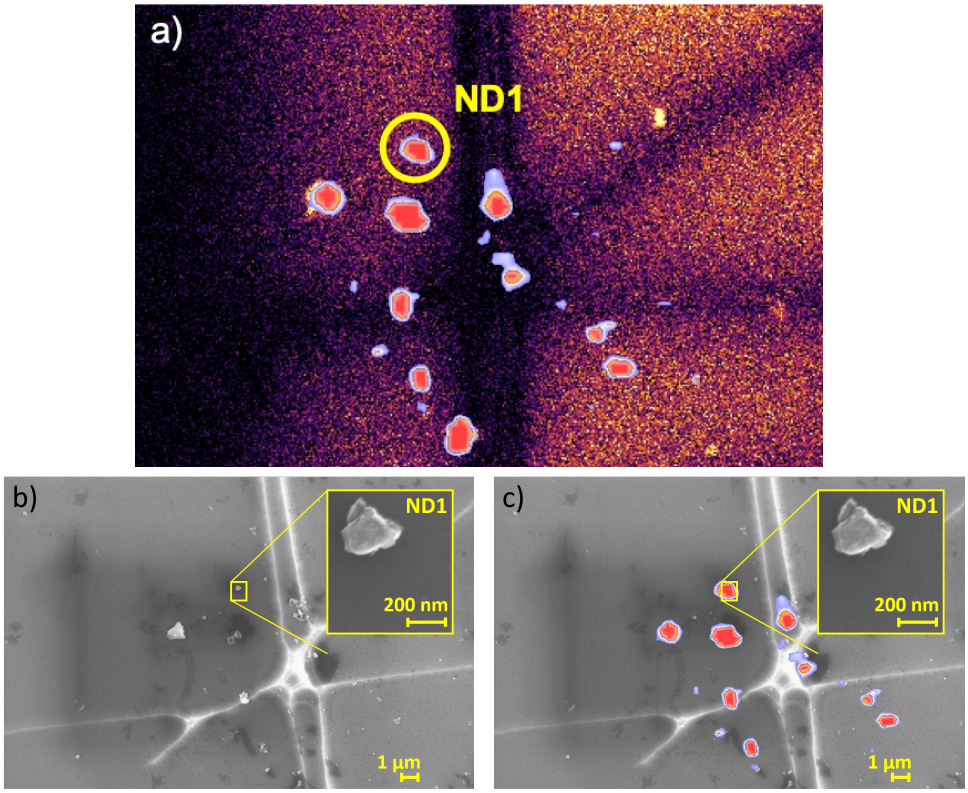

Figure 7.13: a) Confocal microscope fluorescence heatmap of sample ND1 overlaid on reflection image. The ND is too small to resolve conclusively on the confocal microscope which is diffraction limited, so SEM imaging (b) is necessary to provide an accurate measurement of ND size. The ND inset is approximately 323 nm at its widest point. c) Fluorescence data overlaid on an SEM image, allowing ODMR data to be matched to specific diamonds. Note that sites distinguishable as multiple nanodiamonds in SEM may appear as single objects in CFM.

7.4.1 Auto-correlation statistics

Taking $g^{(2)}(0)$ auto-correlation measurements from a large number of fluorescent sites can provide an estimate of the yield of NDs containing single centres from a given sample. This process was automated using a Python/Jupyter script written by myself. Though individual sites were selected manually, auto-correlation measurements were taken automatically by this script, which returned to the user-defined sites and monitored them for one minute (to ensure a roughly constant count rate) before taking an HBT measurement. Figure 7.14 shows the results of auto-correlation measurements from 69 nanodiamonds on a single silicon wafer with no bias field applied so as to minimise the impact of NV orientation. Sites were only chosen whose fluorescence appeared to come from a single, circular source, where no evidence of aggregation was present. As such, some larger single NDs may have been excluded as in CFM imagery they may be indistinguishable from aggregated sites of multiple NDs. Ideally, SEM images would have been obtained beforehand to identify lone NDs and separate them from multiple NDs (see figure 7.13).

These data indicate that roughly 39% of NDs measured contained single NV^- centres. Of those, 7 were seen to have photon count rates of below 20,000 counts/sec, which was determined to be insufficiently fluorescent for T_2 measurements. From the remaining 20, the vast majority were at excessive distances on the silicon for microwave absorption at high enough levels for ODMR detection. These figures show that only one a small number NDs from a single Si wafer will be suitable for pulsed ODMR measurements.

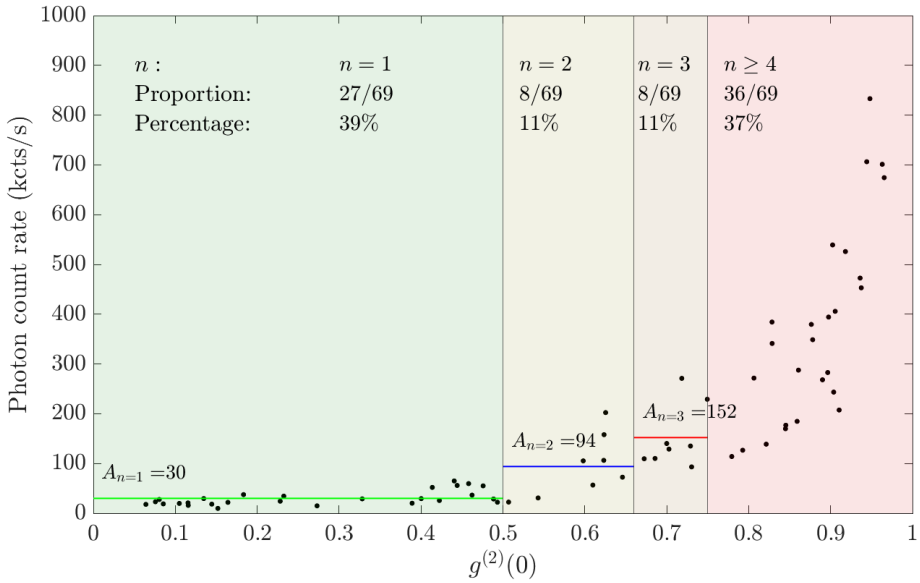

Figure 7.14: Autocorrelation values plotted against photon count rates for 69 nanodiamonds on a single silicon wafer sample. Vertical lines delineate $g^{(2)}(0)$ values corresponding to integer numbers of NVs. Horizontal lines represent average photon counts ($A_{n=x}$ where x is the number of NVs) for NDs in that category.

These data also indicate that the average fluorescence count ($A_{n=x}$ where x is the number of NVs per nanodiamond) is not directly proportional to the number of NVs as could be expected. Extrapolating from $A_{n=1} = 30$, it would be reasonable to suspect that $A_{n=2} = 2A_{n=1}$, however, in fact $A_{n=2} = 3.1 \cdot A_{n=1}$. Similarly, $A_{n=3} = 5.1 \cdot A_{n=1}$. This may be as a result of outliers skewing the average due to host NDs being smaller than the fluorescence wavelength, leading to improved collection efficiency compared to NDs larger than the fluorescence wavelength. In larger NDs, internal reflections and portions of the material lying outside the confocal volume could reduce the number of photons collected.

7.5 Pulsed ODMR results

7.5.1 Rabi

Figure 7.15 shows the Rabi oscillations of four single NVs with a fit of the function

$$f(t) = A \cdot \sin\left(2\pi f_{Rabi} t + \phi\right) \cdot e^{\frac{-t}{\tau}} + C \tag{7.4}$$

where A is the amplitude of the oscillation, f_{Rabi} is the characteristic Rabi frequency and τ is the Rabi coherence time of the centre. Applied magnetic fields ranged between 15 mT and 30 mT.

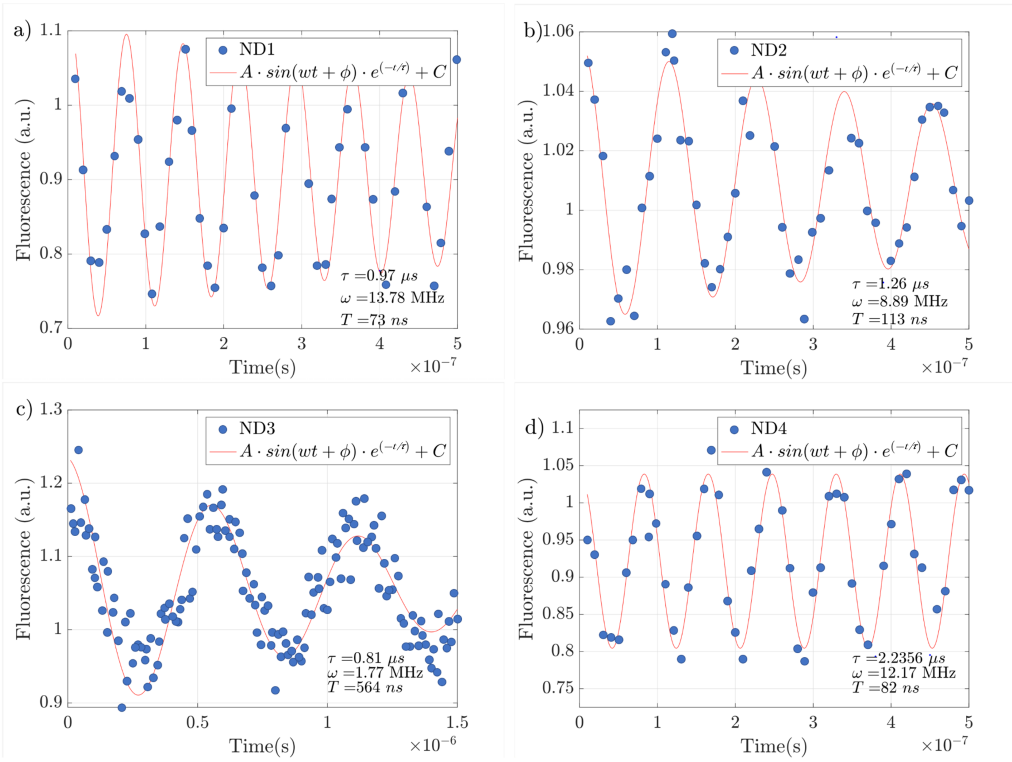

Figure 7.15: Rabi oscillations for four NVs in nanodiamond. T is the Rabi period.

With Rabi frequencies of 13.78 MHz and 8.89 MHz respectively, NDs 1 and 2 are likely coupled to nearby ^{13}C atoms,[6] making them possibly appropriate for use as a 2-qubit system. NDs 3 and 4 may be too distant from any ^{13}C atoms to

display coupling. The signature of any such coupling could be improved though by increasing the applied magnetic field.[7]

7.5.2 Spin echo

Figure 7.16 shows the results of spin echo measurements for the same four nanodiamonds measured in figure 7.15 (see chapter 5 and section 7.3 of this chapter for details of how these data were acquired).

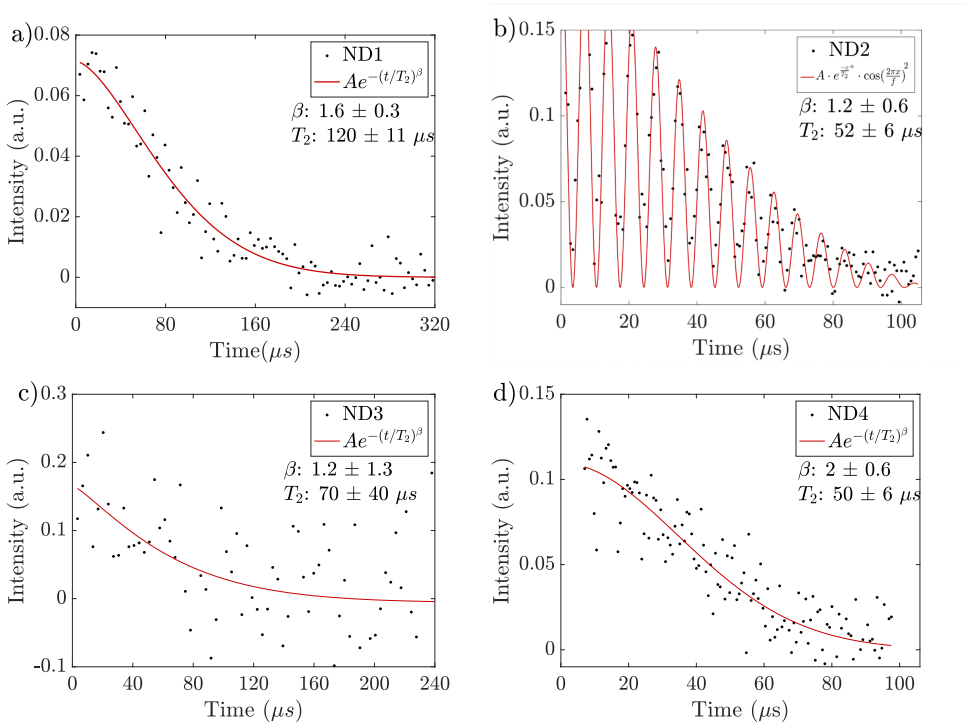

Figure 7.16: a-d) Spin echo measurements from four nanodiamonds. Note that for ND2 (b), fluorescence measurements were taken more frequently, allowing the carbon-13 revival period to manifest in the data, leading to characteristic fringes. For other NVs more sparse data were obtained, leaving only the envelope.

These show that generally, single NVs in these nanodiamonds have spin-spin decoherence times of around $T_2 = 50\,\mu\text{s}$. However, the NV present in ND1 showed longer coherence, which may be due to increased nanodiamond diameter ensuring that surface spins are kept at a greater distance from the NV centre itself. To gain

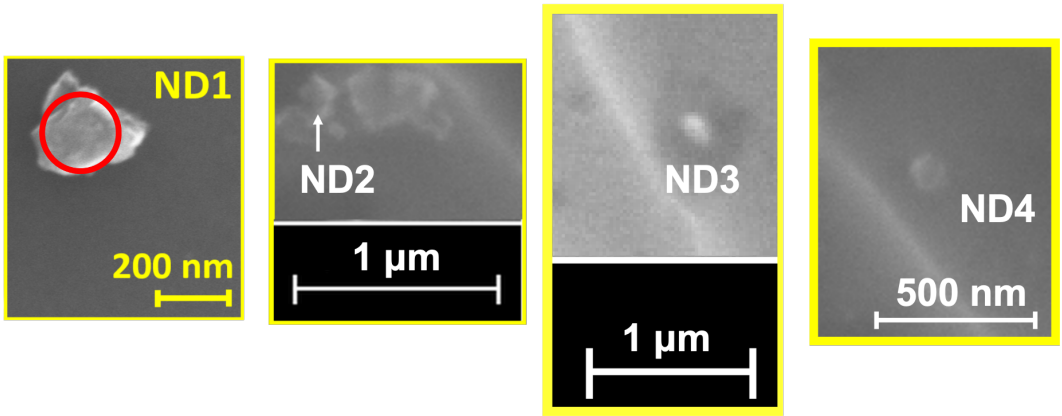

Figure 7.17: The four nanodiamonds used for these experiments. A circle has been drawn on ND1 whose centre represents the estimated greatest distance an NV may be from the surface. However, it should be noted that as the SEM does not provide a three dimensional image, height data regarding the ND cannot be obtained. The low quality of NDs 2, 3 and 4 is a result of differing experimental conditions preventing the acquisition of high resolution data, namely sample drift due to charging on the sample during SEM imaging and operator inexperience at the time these measurements were taken.

an understanding as to whether or not this may be the case, Pulsed ODMR data was combined with data from SEM to determine whether or not there is a relationship between nanodiamond size and spin-spin decoherence time. It should be noted that the values for β seen in all four of these examples, which describe the stretching of the exponential, agree with expected values for the corresponding T_2 coherence times[8] for systems not limited by ^{13}C.[9]

Sample	Address	R_{max} (nm)	Rabi period (ns)	T_2 (μs)
ND1	KNMO13#1	106 ± 2	73 ± 1	120 ± 11
ND2	ENMS10#3	71 ± 4	113 ± 1	52 ± 6
ND3	LMKO00#1	68 ± 6	564 ± 1	70 ± 40
ND4	ENNU32#1	54 ± 6	82 ± 1	50 ± 6

Table 7.1: PODMR data and dimensions obtained via SEM for the four nanodiamonds. R_{max} is the maximum possible distance between the measured NV^- and the surface of the nanodiamond.

Figure 7.17 shows two nanodiamonds, ND1 and ND2, with a ring overlaid over ND1 showing the maximum distance between an NV and the surface. Table 7.1 compares these distances with the T_2 times for all four of the nanodiamonds measured in 7.16. With the small sample size and the fact that only maximum (not actual) distance between the NV and the surface being available, it is not possible to determine whether or not this distance is the limiting factor on the length of the T_2. However, the largest nanodiamond (ND1) does host the NV with the longest T_2 time.

Previously, T_2s in nanodiamond have been limited to <10 µs in high yield material and ≤360 µs in low yield material for natural isotope abundance with spin-echo measurement[10, 11] as detailed in chapter 4. These results show that using our high yield milling method along with high purity material, it is possible to obtain T_2 times comparable with low yield, high complexity production methods and even exceeding that obtained with dynamical decoupling in high yield material. However, the unsuitability of many of the nanodiamonds may reduce the usefulness of our yield, although a more in depth understanding of the reasoning behind this unsuitable behaviour could lead to its mitigation. It should also be pointed out that due to the inaccessibility of many of the NDs with the repositionable magnet discussed in this chapter, many of the nanodiamonds treated as unusable may indeed have been

more suitable for measurement had it been possible to align the bias magnetic field to the NV symmetry axes in those NVs.

A comparison of these results with those seen bulk material is also warranted. NVs in single crystal bulk material measured on the apparatus used here consistently display count rates exceeding 1.2×10^5 counts/sec, whereas even when aligned to the bias magnetic field, ND1 produced at best 5.8×10^4 counts/sec. This is attributed to the irregular shape of nanodiamonds affecting the transmission of light out of the crystal. These low count rates can have an effect on the accuracy of measurements as during pulsed ODMR pulse sequences, periods with low excitation result in an inability of the Qudi tracking software to retain the location of the ND.
The T_2 times reported here are also lower than those achievable in bulk single crystal material. In the latter case, coherence times exceeding 1 s have been reported.[12] Though these coherence times were achieved using dynamic decoupling techniques, they still exceed coherence times reported in ND1 when dynamic decoupling was applied.[13] The difference in coherence times achieved between bulk material and nanodiamond is suspected to be due to the presence of surface spins on the nanodiamond in close proximity to the NV centre.

7.6 Future research

Immediately after the research detailed here, the next step would be to apply dynamical decoupling techniques which could extend the T_2 time of this material to over 1 ms without altering the material in any fashion, approaching some T_2 times in bulk single crystal material (although ultimately, T_2s in NDs are likely to be limited by surface interactions and so are unlikely to match those times in bulk SCD). Subsequent research should focus on further further purifying precursor material, not only in terms of nitrogen concentration but also carbon isotopic purification, reducing the component of decoherence produce by the presence of ^{13}C in the diamond

lattice. With longer T_2s, a number of research opportunities present themselves for consideration. NV$^-$s could be employed to investigate the spin bath provided by surface spins on nanodiamonds themselves. This in turn might lead to better material which would improve the usefulness of NVs in ND for probing external environments, such as spins in silicon which might be of interest to the semiconductor industry. Further to this, long T_2 times in these nanodiamonds may potentially be employed for the investigation of fundamental physics (see chapter 8).

Chapter 7 References

[1] R.H. Webb. Confocal optical microscopy. *Reports on Progress in Physics*, 59(3):427–471, Mar 1996.

[2] J.A. Conchello and J.W. Lichtman. Optical sectioning microscopy. *Nature Methods*, 2(12):920–931, Dec 2005.

[3] R. Hanbury Brown and R.Q. Twiss. LXXIV. A new type of interferometer for use in radio astronomy. *The London, Edinburgh, and Dublin Philosophical Magazine and Journal of Science*, 45(366):663–682, 1954.

[4] A. Beveratos, R. Brouri, T. Gacoin, J.-P. Poizat, and P. Grangier. Nonclassical radiation from diamond nanocrystals. *Physical Review A*, 64:061802, 2001.

[5] H. Fu and P. R. Berman. Microscopic theory of spontaneous decay in a dielectric. *Physical Review A*, 72:022104, 2005.

[6] A. Dréau, J.-R. Maze, M. Lesik, J.-F. Roch, and V. Jacques. High-resolution spectroscopy of single NV defects coupled with nearby ^{13}C nuclear spins in diamond. *Phys. Rev. B*, 85:134107, 2012.

[7] J. R. Maze, A. Dréau, V. Waselowski, H. Duarte, J.-F. Roch, and V. Jacques. Free induction decay of single spins in diamond. *New Journal of Physics*, 14:103041, 2012.

[8] C.J. Stephen, B.L. Green, Y.N.D. Lekhai, L. Weng, P. Hill, S. Johnson, A.C. Frangeskou, P.L. Diggle, Y.-C. Chen, M.J. Strain, E. Gu, M.E. Newton, J.M.

Smith, P.S. Salter, and G.W. Morley. Deep Three-Dimensional Solid-State Qubit Arrays with Long-Lived Spin Coherence. *Phys. Rev. Applied B*, 12:064005, 2019.

[9] Z.-H. Wang, G. de Lange, D. Ristè, R. Hanson, and V.V. Dobrovitski. Comparison of dynamical decoupling protocols for a nitrogen-vacancy center in diamond. *Phys. Rev. B*, 85:155204, 2012.

[10] P. Andrich, B. J. Alemán, J. C. Lee, K. Ohno, C. F. de las Casas, F. Joseph Heremans, E. L. Hu, and D. D. Awschalom. Engineered Micro- and Nanoscale Diamonds as Mobile Probes for High-Resolution Sensing in Fluid. *Nano Letters*, 14:4959–4964, 2014.

[11] Helena S. Knowles, Dhiren M. Kara, and Mete Atatüre. Observing bulk diamond spin coherence in high-purity nanodiamonds. *Nature Materials*, 13(21), Nov 2013.

[12] M. H. Abobeih, J. Cramer, M. A. Bakker, N. Kalb, M. Markham, D. J. Twitchen, and T. H. Taminiau. One-second coherence for a single electron spin coupled to a multi-qubit nuclear-spin environment. *Nature Communications*, 9, Jun 2018.

[13] B. D. Wood, G. A. Stimpson, J. E. March, Y. N. D. Lekhai, C. J. Stephen, B. L. Green, A. C. Frangeskou, L. Gins, S. Mandal, O. A. Williams, S. Bose, and G. W. Morley. Matter and spin superposition in vacuum experiment (massive). *arXiv:2105.02105*.

Chapter 8

Optical trapping

8.1 Theory & motivation

Evidence of optical trapping experiments were first published in 1970 by Arthur Ashkin at Bell Laboratories, who held micron sized particles in stable optical wells produced by a 1 W continuous wave laser.[1] This built on work by others[2, 3] which hinted at radiation pressure as a useful force, but the potential applications of these physical phenomena were not guessed at until much later.

8.1.1 Macroscopicity

That quantum mechanics and general relativity remain at loggerheads despite the success and usefulness of both fields might be surprising to one who witnessed the blistering pace of physics research through the nineteenth and twentieth centuries. Not only does a unification of the two theories appear not to be on the horizon, but the location of the boundary between them remains as yet a mystery. Placing particles of ever increasing numbers of atoms into a spatial superposition though, a purely quantum mechanical state of affairs, may shed light on the whereabouts of this elusive boundary. Although theory tells us that any object, no matter how massive and no matter from how many atoms it is constructed, should be able to be placed in a spatial superposition,[4] our experience tells us that this is not so. In fact, it was not until relatively recently that we discovered that any object *at all* could be placed into such a state,[5] although Young's famous double slit experiment had begun to suggest that the evidence of our senses might not be sufficient to explain the world around us in 1801.[6]

More recently however, larger objects such as complex molecules[7] have been placed into a spatial quantum superposition, and several measures of a superposition's 'macroscopicity' have been proposed.[8] Such measures define the macroscopicity of a mechanical system, such as an oscillator, as its experimental demonstration's ability to rule out modifications to quantum mechanics, using only the observable

consequences of the experiment. One proposal[9] sees a nanodiamond bead containing an NV$^-$ suspended in an optical trap (see figure 8.1).

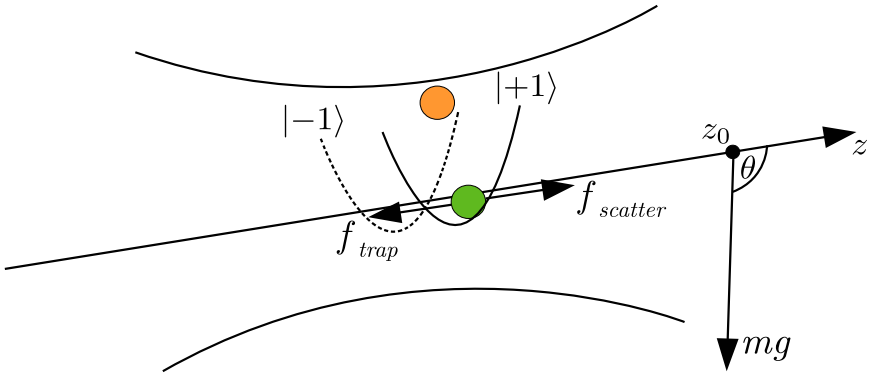

Figure 8.1: An optical trap suspends a particle where the trapping force f_{trap} equilibriates with a scattering force $f_{scatter}$. A nanodiamond particle is suspended in an optical trap with the direction of weakest confinement and the NV$^-$ spin quantisation aligned along the optical axis. A magnet at z_0 means that the $|-1\rangle$ and $|+1\rangle$ states will be attracted to the centre of the harmonic well to a different degree. The gravitational force mg is oriented at a non-perpendicular angle θ to the optical axis, leading to differing gravitational potentials for the $|-1\rangle$ and $|+1\rangle$ states. As the two states (orange and green circles) oscillate along the z-axis, they accrue a gravitational phase difference.

The spin of the the NV is coupled to the oscillatory motion of the bead, meaning that should the NV be placed in a spin superposition, the spatial location of the bead must also be in a superposition. This can be achieved by placing a magnetic sphere at some point along the optical axis which leads to the case where the $m_s = +1$ and $m_s = -1$ spin states experience differing magnetic forces. Provided the optical axis is at a non-perpendicular angle θ to that of the gravitational force, the two states will exist in non-identical harmonic potential wells and therefore will accrue a phase difference as they oscillate. The magnitude of this phase difference can be measured by spin readout when:

$$t_0 = \frac{2\pi}{\omega_z} \tag{8.1}$$

providing a measurement of the macroscopicity of the superposition, where ω_z is the frequency of the particle's oscillation through the z-axis. This is a single period of oscillation of the optically trapped system, with the two components of the superposition spatially coinciding, leading to interference.

8.1.2 The physics of optical trapping

An optical trap works by applying multiple opposing forces upon a particle, causing the particle to become suspended at the equilibrium point of these forces. In this research, these forces both originate from a focused laser beam. An attractive ('trapping') force, f_{trap} arises from the concentration of light at the focal point, resulting in a strong, localised electric field gradient.[10] A scattering force $f_{scatter}$ occurs due to the radiation pressure exerted on the particle[11] (see figure 8.2). The equilibrium point between these two forces then forms a potential well about which the particle oscillates.[12] In the z-axis, i.e. that axis parallel to the optical axis, the particle therefore sits just 'downstream' of the trapping beam's focal point. Along the y-axis, that axes perpendicular to both the optical axis and the gravitational force, the trapping force is dominant, keeping the bead central. Finally in the x-axis, parallel to the gravitational force, there is an equilibrium point which exists between the trapping force and the gravitational force, causing the bead to 'sag' relative to the focal point of the trapping beam. It is important to note that essential to this proposal is feedback cooling of the suspended nanodiamond's centre-of-mass (COM) temperature to mK levels, in order to reduce the thermal state phonon number below the limit at which the harmonic approximation breaks down.

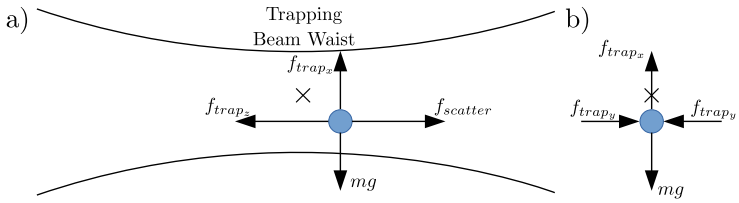

Figure 8.2: The forces effective on a dielectric particle in an optical trap when viewed along the y-axis (a) and along the z-axis (b). The electric field maximum sits at the beam waist, marked $\times$. This causes an attractive force f_{trap} which is countered in the z-direction by a scattering force $f_{scatter}$ and by the gravitational force mg in the vertical x-direction. In the y-axis, the trapping force is equal in the positive and negative direction, cancelling itself out.

The 'stiffness' of the optical trap, required to keep the nanodiamond fixed in the experiment, can be defined as:[13]

$$k_{trap} = 4\pi^3 \cdot \frac{P_0 \alpha}{c\epsilon_0} \cdot \frac{(N.A.)^4}{\lambda^4} \tag{8.2}$$

whilst the the frequency of the trapped particle's oscillation in the z-axis is:

$$w_z = \sqrt{\frac{4P_0\lambda^2}{m\pi^3 w_0^6}} \tag{8.3}$$

and in turn, w_0, the diameter of the beam waist, is related to the numerical aperture (N.A.) of the trapping lens by:

$$\frac{f\lambda}{w_0} \approx \frac{2\lambda}{(N.A.)} \tag{8.4}$$

$$w_0 = \frac{f(N.A.)}{2} \tag{8.5}$$

so therefore:

$$w_z = \sqrt{\frac{8^6 \cdot 4P_0\lambda^2}{m\pi^3 (f(N.A.))^6}} \tag{8.6}$$

where P_0 is the power of the trapping beam, α is the polarisability of the

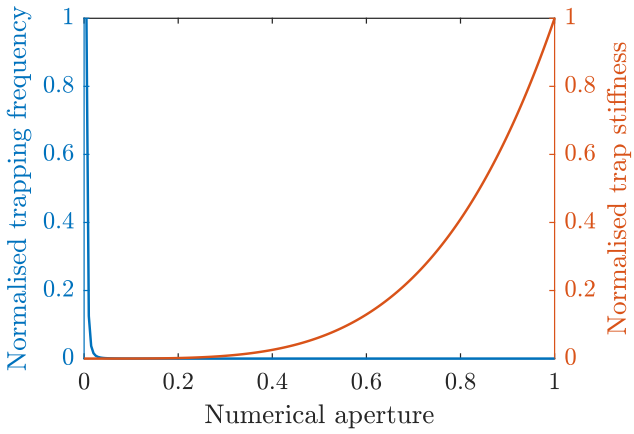

Figure 8.3: Numerical aperture of the trapping lens has a direct effect on the trap stiffness and the trapping frequency.

nanodiamond bead, λ is the trapping wavelength and f is the focal length of the trapping lens.

From this it can be seen that an increase in trap stiffness by increasing the numerical aperture of the trapping lens comes at the cost of reduced trapping frequency, the latter variable being important for parametric feedback cooling of the bead's centre of mass temperature. Higher trap frequencies allow the x, y and z components of the particle's oscillation to be more spread out in the frequency domain and therefore to be extracted more easily.

8.1.3 Experimental considerations

The proposal discussed in subsection 8.1.1 faces a number of challenges that must be overcome before it can be realised. Firstly, the experiment must be contained within an ultra-high vacuum environment in order to limit interactions between the nanodiamond bead and gaseous species.

Achieving ultra high vacuum (pressure below 10^{-9} mbar) is not difficult in itself. However, heating of the nanodiamond by the trapping laser reduces spin coherence times and can graphetise the diamond.[14] However, by increasing the purity of the diamond precursor from which the nanodiamonds are fabricated, lower absorption

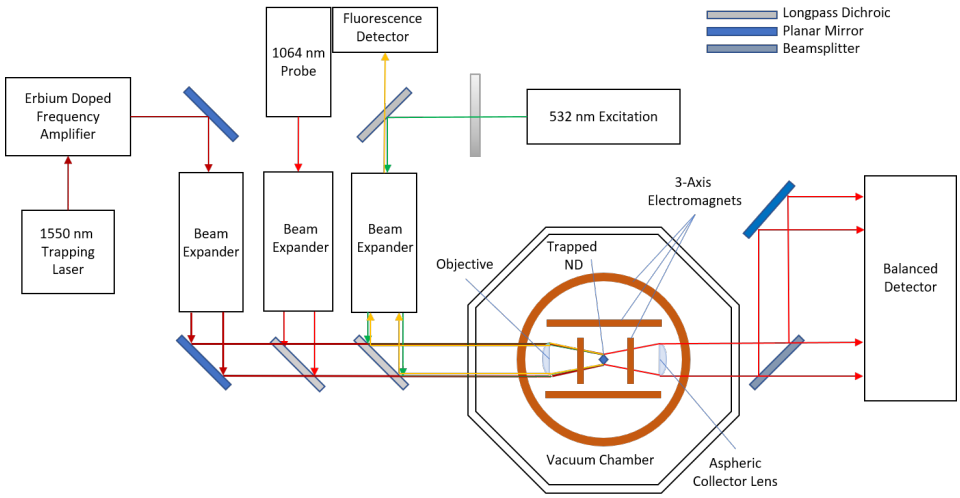

Figure 8.4: Setup of the optical trap. A 1550 nm trapping beam is amplified by an EDFA before being expanded and then focused to trap a particle. A 1064 nm probe beam is similarly expanded and then travels co-linearly with the trapping beam through the trapped sample to a balanced detector. A 532 nm beam is also expanded before being focused on the trapped particle where it stimulates fluorescence from the NV centre. The fluorescence then returns along the excitation path where it is selected by a dichroic mirror before arriving at a detector.

of the trapping energy limits this graphetisation,[13] preventing decreases to T_2 coherence times and enables longer spin coherence compared to other diamond material (see chapter 7).

8.1.4 Trapping apparatus

The apparatus for optical trapping can be seen in figure 8.4. This consists of a vacuum chamber, three lasers, an erbium doped fibre amplifier (EDFA) and a balanced detector as well as supplementary optics. The 1550 nm trapping beam is amplified to a power of up to 3 W, with the beam intensity controlled by computer communication with the EDFA. The beam is then expanded to back-fill the trapping objective, whereupon it is focused by an aspheric lens in order to trap a particle. The nanodiamonds are inserted into the vacuum chamber by creating a mild vac-

uum in the chamber and then opening a tap, into which a mist of NDs are sprayed. Under ideal circumstances, one of these many NDs travels near to the optical focus and is trapped by the electric field gradient.

A second beam at 1064 nm travels co-linearly with the trapping beam, reaching focus at or near to the same point as the trapping beam. It then passes to an aspheric collector lens and to a balanced detector.

A third beam of 532 nm light is also focused on the trapped nanodiamond in order to stimulate fluorescence for ODMR.

Balanced detection

Interferometric balanced detection operates by measuring differing intensities of light at two photodiodes. This difference in intensity is produced by the destructive interference caused by a differing path length in light which has been scattered by interaction with the trapped particle, as opposed to light which has not been scattered, resulting in a lower signal at one of the photodiodes.

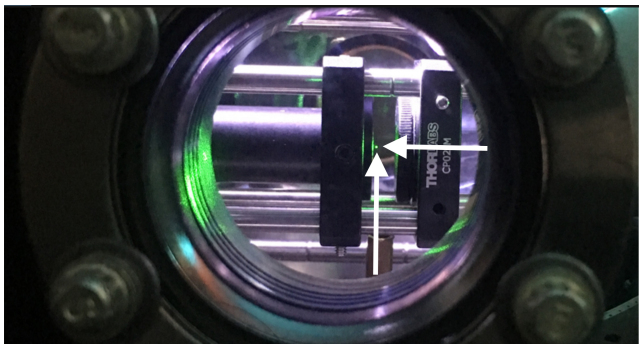

Figure 8.5: A nanodiamond (indicated by white arrows) suspended in the optical trap. Note that the green light visible does not trap the particle but is used for ODMR. The 1550 nm trapping beam and the 1064 nm probe beam are invisible.

8.1.5 Trap frequency

As detailed in section 8.1.2, the use of a high numerical aperture objective is required to ensure an optical trap which is stiff enough to maintain confinement of

the nanodiamond. However, it must also be of a low enough NA that a high trap frequency is maintained. For these experiments, an aspheric lens of $N.A. = 0.77$ was chosen. The trap apparatus was built initially by Angelo Frangeskou and Anis Rahman, and the aspheric lens was selected and installed by myself.

To test the result of using the aspheric lens, the apparatus was constructed in the manner detailed in figure 8.4 with the aspheric lens used as the objective. It should be noted that this is distinct from the aspheric collector lens which is not involved in the trapping process but instead collects light and directs it to the balanced detector. Once the apparatus was constructed, the vacuum chamber was sealed and the pressure decreased slightly (by a few tens of millibar) by the use of a rotary pump. A small tap in the side of the vacuum chamber was then opened and a sample of nanodiamonds suspended in HPLC methanol was injected using a nebuliser, after which the tap was closed. By observing the output of the balanced detector, the capture of a nanodiamond verified by observing the appearance of a broad peak in the FFT of the balanced detector output. Once this capture was verified, the pressure in the chamber was allowed to fall to around 300 mbar, whereupon the rotary pump was turned off and a turbopump activated. This brought the pressure down to 1.2 mbar at which point several peaks (see fig. 8.6) were observed, with the rightmost peak attributed to the oscillation in the z-axis (the axis parallel to the optical path).

This resulted in z-axis trapping frequencies in excess of 220 kHz as opposed to approximately 150 kHz when using an $N.A. = 0.8$ microscope objective as in previous efforts. The operation of the trapping apparatus and the data acquisition were performed by myself.

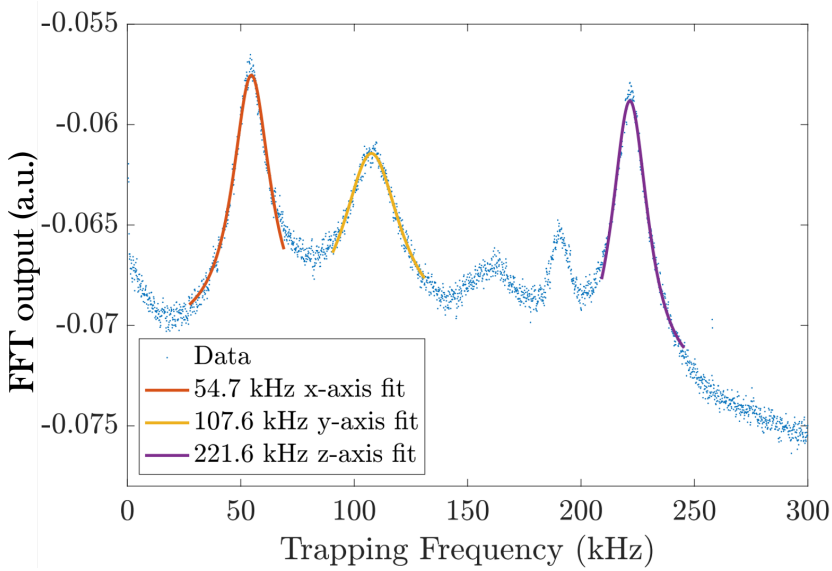

Figure 8.6: An FFT of balanced detector output, showing trapping frequencies measured with a 0.77 NA aspheric lens using a 1550 nm trapping laser. The x- and y-axes are well separated and the z-axis has a comparatively high trapping frequency of 221.6 kHz. Smaller peaks are thought to correspond to interference and imbalance, such as rotations or torsional motion of the particle.[15]

Furthermore, higher trapping frequencies result in more well defined peaks in the detection data (see figure 8.6). These peaks correspond to oscillations in the x-, $y-$ and z-axes.[15] Parametric feedback cooling of the trapped diamond could potentially be used to cool the particle close to its ground state, which requires careful measurement of the particle's motion in each of the three axes. This data is then used to modify the trap stiffness at twice the frequency of oscillation in a given axis.[16] Careful separation of these peaks is therefore crucial to prevent oscillations from other axes causing interference.

8.2 Homogeneous magnetic fields

For ODMR of NVs in levitated diamond to be performed, it is necessary to deliver a fully orientable, homogeneous magnetic field *in situ*. Whilst in the confocal microscope (see chapter 6) this may take the form of a permanent magnet on a two

axis armature, the vacuum system in use for optical trapping prevents such a configuration in this case. Instead, a three axis magnetic field assembly was designed and machined from aluminium (see figure 8.7). This consists of three sets of nested Helmholtz coils, each providing magnetic field control of their respective axes.

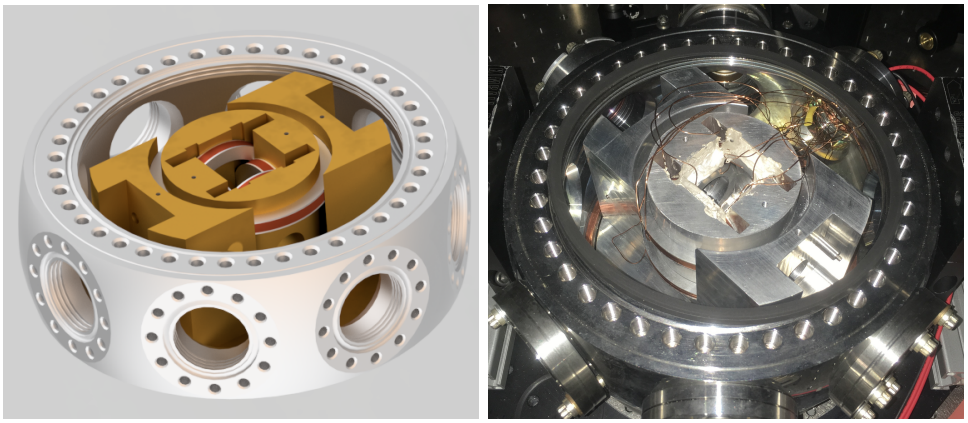

Figure 8.7: Left: Three dimensional model of the 3-axis, Helmholtz-type homogeneous magnetic field assembly. The six coils forming the three Helmholtz magnets are supported by an aluminium structure (coloured gold in this model) which also acts as a heat sink for the device. Right: photo of the chamber. Note the addition of silver paste around the coils for improved thermal management.

The presence of six electromagnetic coils in a vacuum chamber leads to significant levels of heating to achieve the desired magnetic field at the centre of the trap (15 mT was chosen as a reasonable field). Although the magnetic field assembly and the vacuum chamber itself are comprised of thermally conductive metal, thermal imaging of the chamber indicated that temperatures were rising to levels which could damage various parts of the experimental apparatus. To reduce this heating, silver paste was added between the coil assembly and the base of the chamber, as well as between the coil assembly and the coils themselves. The effect of the heating with and without the silver paste can be seen in figure 8.8. The maximum field obtained using this configuration was 18 mT, though some heating was still taking place after measurements ceased (see fig. 8.8). Before such a field could be described as useful, the homogeneity of the field would need to be examined.

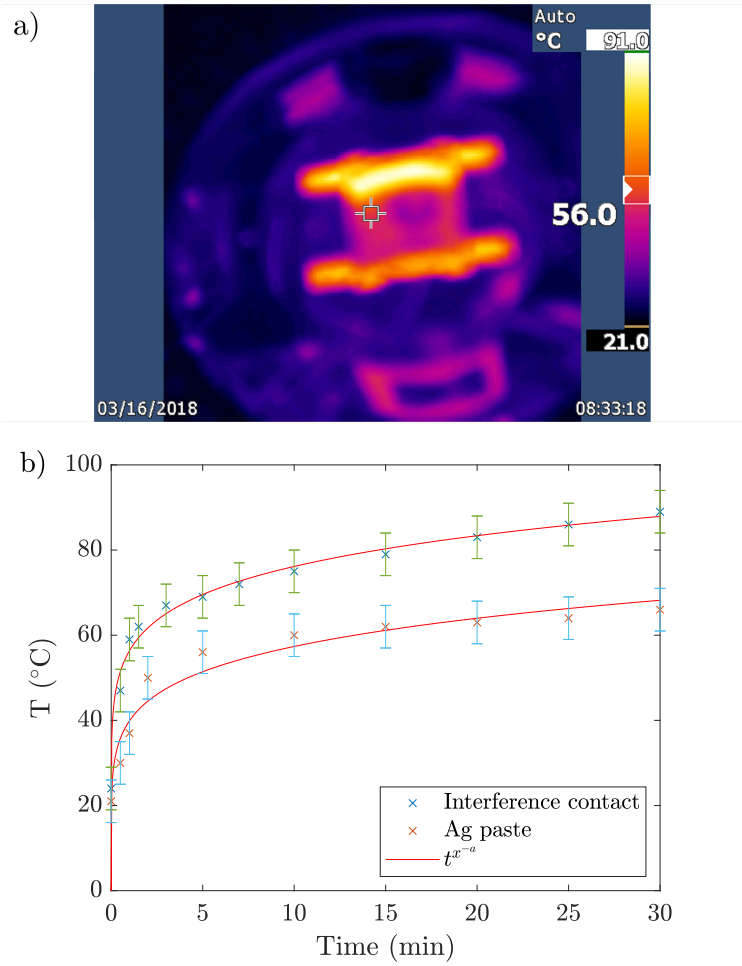

Figure 8.8: a) Heating of the z-axis coil captured by thermal imaging camera. b) Heating of the coil assembly over time. The addition of a silver paste at the interface between the assembly and the vacuum chamber reduces the heating rate and maximum temperature of the system. Temperatures were monitored by using a thermal imaging camera whilst the vacuum chamber was unsealed and the lid removed.

8.3 Future research

With the application of a thermally stable, homogeneous magnetic field, ODMR can now be performed. However, in order to undertake the experiments discussed in section 8.1, the pressure in the vacuum chamber must be reduced such that collisions between the trapped particle and ballistic air molecules are sufficiently rare. This will be essential if the particle is to be kept in a spatial superposition as such interactions can lead to a collapse of that superposition.[17, 18, 19]
Also critical to this research will be the development of nanodiamonds suitable for the experiments. As discussed in chapter 4, the size of the particle is crucial in obtaining long enough NV spin coherence times for measurements to be taken. Inroads have been made to this goal, detailed in chapter 7, where high purity diamond with widely spaced NVs led to NDs of several hundred nanometres in diameter containing a single NV only. Similarly, research performed by other members of the group[13] show that the substitutional nitrogen concentration in the material used is sufficient to reduce heating of the nanodiamonds and the subsequent graphetisation.

The data from these experiments, along with the improvements suggested, open up the potential for further experiments into the macroscopicity of particles in a quantum superposition to be realised, among others. This work shows not only what is possible, but what is necessary to see such visions become a reality.

Chapter 8 References

[1] A Ashkin. Acceleration and Trapping of Particles by Radiation Pressure. *Physical Review Letters*, 24(4):156, 1970.

[2] Nichols, E. F. and Hull, G. F. A preliminary communication on the pressure of heat and light radiation. *Phys. Rev. (Series I)*, 13:307–320, 1901.

[3] P. N. Lebedev. Experimental Examination of Light Pressure. *Annalen der Physik*, 6(433), 1901.

[4] M. Arndt and K. Hornberger. Testing the limits of quantum mechanical superpositions. *Nature Phys.*, 10:271277, 2014.

[5] C. J. Davisson and L. H. Germer. Reflection of Electrons by a Crystal of Nickel. *P.N.A.S.*, 14(4):317–322, 1928.

[6] E. Tretkoff, J. Ouelette, and A. Chodos. May 1801: Thomas Young and the Nature of Light. *APS News*, 17(5), 2008.

[7] S. Gerlich, S. Eibenberger, M. Tomandl, S. Nimmrichter, K. Hornberger, P.J. Fagan, J. Tüxen, M. Mayor, and M. Arndt. Quantum interference of large organic molecules. *Nature Communications*, 2:263, 2011.

[8] S. Nimmrichter and K. Hornberger. Macroscopicity of Mechanical Quantum Superposition States. *Phys. Rev. Lett.*, 110:160403, 2013.

[9] M. Scala, M. S. Kim, G. W. Morley, P. F. Barker, and S. Bose. Matter-wave

interferometry of a levitated thermal nano-oscillator induced and probed by a spin. *Phys. Rev. Lett.*, 111:180403, 2013.

[10] Lukas Novotny, Randy X. Bian, and X. Sunney Xie. Theory of nanometric optical tweezers. *Phys. Rev. Lett.*, 79:645–648, 1997.

[11] Nan Li, Xun-min Zhu, Wen-qiang Li, Zhen-hai Fu, Meng-zhu Hu, and Hui-zhu Hu. Review of optical tweezers in vacuum. *Frontiers of Information Technology & Electronic Engineering*, 20(5):655–673, 2019.

[12] R. W. Bowman and M. J. Padgett. Optical trapping and binding. *Reports on Progress in Physics*, 76(2):026401, 2013.

[13] A. C. Frangeskou, A. T. M. A. Rahman, L. Gines, S. Mandal, O. A. Williams, P. F. Barker, and G. W. Morley. Pure nanodiamonds for levitated optomechanics in vacuum. *New Journal of Physics*, 20(043016), 2018.

[14] A. T. M. A. Rahman, A. C. Frangeskou, M. S. Kim, S. Bose, G. W. Morley, and P. F. Barker. Burning and graphitization of optically levitated nanodiamonds in vacuum. *Scientific Reports*, 6:21633, 2016.

[15] A. T. M. A. Rahman, A. C. Frangeskou, P. F. Barker, and G. W. Morley. An analytical model for the detection of levitated nanoparticles in optomechanics. *Review of Scientific Instruments*, 89(2):023109, 2018.

[16] L. Ferialdi, A. Setter, M. Toros, C. Timberlake, and H. Ulbricht. Optimal control for feedback cooling in cavityless levitated optomechanics. *New Journal of Physics*, 21(7):073019, 2019.

[17] Anton Zeilinger. Decoherence and the quantum-to-classical transition. *Nature*, 451(7174):18, 2008.

[18] Oriol Romero-Isart. Quantum superposition of massive objects and collapse models. *Phys. Rev. A*, 84:052121, 2011.

[19] E. Joos, H.D. Zeh, C. Kiefer, D. Giulini, J. Kupsch, and I.-0. Stamatescu. *Decoherence and the Appearance of a Classical World in Quantum Theory.* Springer, 2nd edition, 2003.

Chapter 9

Conclusion

Research was presented regarding the suitability of high purity nanodiamonds containing nitrogen vacancy centres for matter wave interferometry experiments, alongside the characterisation of an open source lock-in amplifier for multi-detector magnetocardiography based on NV centres in diamond. Limitations were discussed regarding the collection efficiency of optical apparatus in the latter case, and long spin-spin coherence times were demonstrated to benefit the former.

9.1 Summary of findings

An open source, high frequency LIA was shown to produce sensitivities of up to $90\,\mathrm{nV}\sqrt{\mathrm{Hz}}$ at 500 kHz demodulation, an order of magnitude larger than those of a commercial available alternative which provides sensitivities of $5\,\mathrm{nV}\sqrt{\mathrm{Hz}}$. However, due to a cost two orders of magnitude lower and a similar maximum demodulation frequency, such a sensitivity was seen to be acceptable under certain circumstances, particularly where large numbers of LIAs are required. The LIA was characterised in a manner that no open source, high frequency competitor has been previously, and the relevant research was published in light of such an observation.[1] This characterisation included data describing two methods of data acquisition and the linearity of the device's output. The effect of time constant, demodulation frequency and increased collection time were explored, demonstrating that the device behaved as could be reasonably expected and, in some cases, exceeded expectation.

Further to this, the intrinsic electronic, thermal and mechanical properties of diamond were discussed, and the results of confocal fluorescence microscopy experiments on high purity nanodiamonds on a silicon substrate map were presented. These nanodiamonds were shown to host nitrogen vacancy centres which had spin-spin decoherence (T_2) times in excess of the high yield ND in previous research.[2] These coherence times were suggested to owe their duration to large dimensions and low substitutional nitrogen concentration of the host nanodiamonds.

These nanodiamonds were also investigated using scanning electron microscopy, which allowed the size of the nanodiamonds to be compared to their T_2 times, which suggested increased interactions between surface defects and the colour centres within smaller NDs.

Finally, progress was made towards employing these high purity nanodiamonds for matter-wave interferometry experiments which seek to study the boundary between classical and quantum mechanics. Trapping frequencies exceeding 220 kHz were achieved which are necessary for the centre-of-mass cooling of levitated particles which will be required to reach these goals. Similarly, coupling between the NV electronic spin and the oscillatory motion of a trapped particle were brought one step closer by the introduction of a three axis Helmholtz coil which will enable initialisation and readout of the NV spin state. This ODMR will be essential to probe the quantum superposition into which the levitated nanodiamond is placed.

9.2 Concluding remarks

This thesis has shown that high frequency LIAs are accessible even with modest budgets, and that large numbers of them can be affordably combined to enable multi-detector MCG. It has also shown, however, that a number of improvements should be made in order to extend the sensitivity of diamond magnetometers to bring them into the realms required by this demanding task.

It has also demonstrated that ball milled nanodiamonds may be suitable for advanced experiments into the classical-quantum boundary and that more complex fabrication methods may not be necessary as comparable T_2 coherence times can be achieved in ball milled material. However, further improvements remain to be made before this goal can be achieved.

On a personal note, I would like to interject with the development of my own understanding of the nitrogen vacancy in diamond. Prior to undertaking these experiments and the writing of this thesis, it had seemed to me that the presence of the NV in diamond was purely incidental; that such a defect could have existed in any material such as silicon or cubic boron nitride and that there was nothing save pure happenstance which led to the NV arising in this particular carbon allotrope. However, through exploring the superlative properties of diamond it has become clear, to me at least, that far from random chance, it is these very properties, electrical, optical, thermal and mechanical, which lead to the usefulness of this unique defect and its appropriateness to so many exciting and compelling applications. Diamond's particular structure does not simply play host to the nitrogen vacancy and all its associated properties, instead it gives rise to them, creating a physical system which shows so much promise in so many diverse fields of inquiry.

Chapter 9 References

[1] G. A. Stimpson, M. S. Skilbeck, R. L. Patel, B. L. Green, and G. W. Morley. An open-source high-frequency lock-in amplifier. *Review of Scientific Instruments*, 90(9):094701, 2019.

[2] Helena S. Knowles, Dhiren M. Kara, and Mete Atatüre. Observing bulk diamond spin coherence in high-purity nanodiamonds. *Nature Materials*, 13(21), Nov 2013.